

DISSERTATION

INTERACTIONS OF ARCTIC CLOUDS, RADIATION, AND SEA ICE
IN PRESENT-DAY AND FUTURE CLIMATES

Submitted by

Melissa Ann Burt

Department of Atmospheric Science

In partial fulfillment of the requirements

For the Degree of Doctor of Philosophy

Colorado State University

Fort Collins, Colorado

Spring 2016

Doctoral Committee:

Advisor: David A. Randall

Sonia M. Kreidenweis
Christian D. Kummerow
Michele M. Betsill

Copyright by Melissa Ann Burt 2016

All Rights Reserved

ABSTRACT

INTERACTIONS OF ARCTIC CLOUDS, RADIATION, AND SEA ICE IN PRESENT-DAY AND FUTURE CLIMATES

The Arctic climate system involves complex interactions among the atmosphere, land surface, and the sea-ice-covered Arctic Ocean. Observed changes in the Arctic have emerged and projected climate trends are of significant concern. Surface warming over the last few decades is nearly double that of the entire Earth. Reduced sea-ice extent and volume, changes to ecosystems, and melting permafrost are some examples of noticeable changes in the region.

This work is aimed at improving our understanding of how Arctic clouds interact with, and influence, the surface budget, how clouds influence the distribution of sea ice, and the role of downwelling longwave radiation (DLR) in climate change.

In the first half of this study, we explore the roles of sea-ice thickness and downwelling longwave radiation in Arctic amplification. As the Arctic sea ice thins and ultimately disappears in a warming climate, its insulating power decreases. This causes the surface air temperature to approach the temperature of the relatively warm ocean water below the ice. The resulting increases in air temperature, water vapor and cloudiness lead to an increase in the surface downwelling longwave radiation, which enables a further thinning of the ice. This positive ice-insulation feedback operates mainly in the autumn and winter. A climate-change simulation with

the Community Earth System Model shows that, averaged over the year, the increase in Arctic DLR is three times stronger than the increase in Arctic absorbed solar radiation at the surface.

The warming of the surface air over the Arctic Ocean during fall and winter creates a strong thermal contrast with the colder surrounding continents. Sea-level pressure falls over the Arctic Ocean and the high-latitude circulation reorganizes into a shallow "winter monsoon." The resulting increase in surface wind speed promotes stronger surface evaporation and higher humidity over portions of the Arctic Ocean, thus reinforcing the ice-insulation feedback.

In the second half of this study, we explore the effects of super-parameterization on the Arctic climate by evaluating a number of key atmospheric characteristics that strongly influence the regional and global climate. One aspect in particular that we examine is the occurrence of Arctic weather states. Observations show that during winter the Arctic exhibits two preferred and persistent states — a radiatively clear and an opaquely cloudy state. These distinct regimes are influenced by the phase of the clouds and affect the surface radiative fluxes. We explore the radiative and microphysical effects of these Arctic clouds and the influence on these regimes in two present-day climate simulations. We compare simulations performed with the Community Earth System Model, and its super-parameterized counterpart (SP-CESM). We find that the SP-CESM is able to better reproduce both of the preferred winter states, compared to CESM, and has an overall more realistic representation of the Arctic climate.

ACKNOWLEDGEMENTS

This dissertation would not have been possible without the help and guidance of my advisor, Dr. David A. Randall. It has been an honor to work with and learn from him. I am grateful for his leadership and commitment to excellence throughout this process. Additionally, I would like to thank Drs. Sonia M. Kreidenweis, Christian D. Kummerow, and Michele M. Betsill for their advisement and participation as members of my doctoral committee.

Special thanks is owed to the former and current members of the Randall Research group for their advice and support throughout the years, especially, Mark Branson, Charlotte DeMott and Rachel McCrary. I also would like to thank my CMMAP Education and Diversity colleagues for their encouragement and willingness to listen over the years.

My heartfelt appreciation goes to my family and friends for their overwhelming support throughout this journey. To my parents, your willingness to believe in me and your constant support throughout my life has made me the person that I am today. To my husband Stacy, thank you for bringing joy and happiness into my life during a time when all I could think about was work. But most of all, thank you for dealing with my craziness during this emotional stage of my career.

Finally, I would like to thank the National Science Foundation for supporting this research. This research project was supported by the National Science Foundation Science and Technology Center for Multi-Scale Modeling of Atmospheric Processes, managed by Colorado State University under Cooperative Agreement No. ATM-0425247.

DEDICATION

TO JOHN AND WANDA BURT,

for raising me to believe that anything was possible

AND TO BABY ADAMS,

anything is possible... follow your dreams

TABLE OF CONTENTS

ABSTRACT	ii
ACKNOWLEDGEMENTS	iv
DEDICATION	v
TABLE OF CONTENTS	vi
CHAPTER 1: SEA ICE AND CLOUDS IN THE ARCTIC CLIMATE SYSTEM	1
1.1 FIGURES	9
CHAPTER 2: THE EFFECTS OF DOWNWELLING LONGWAVE RADIATION ON ARCTIC AMPLIFICATION	16
2.1 GLOBAL CLIMATE CHANGE	16
2.2 DARK WARMING	19
2.2.1 INTRODUCTION	19
2.2.2 METHODS	23
2.2.3 THE ICE-INSULATION FEEDBACK	24
2.2.4 THE BIRTH OF A NEW MONSOON	31
2.2.5 COMPARISON WITH CMIP5 MODELS	35
2.2.6 DISCUSSION	40
2.3 SUMMARY	41
2.4 FIGURES	43
CHAPTER 3: THE CLIMATE OF THE SUPER-PARAMETERIZED CESM	77
3.1 SIMULATION OF THE PRESENT-DAY ARCTIC ATMOSPHERE	80
3.2 ARCTIC CLOUDS AND RADIATION	83
3.3 ARCTIC WEATHER STATES	88
3.4 EFFECTS OF SUPER-PARAMETERIZATION ON ARCTIC WARMING	93
3.4.1 GLOBAL CLIMATE CHANGE	93
3.4.2 DARK WARMING IN SP-CESM	95

3.4.3 ARCTIC WEATHER STATES AT 4xCO ₂	99
3.5 SUMMARY	100
3.6 FIGURES	102
CHAPTER 4: SUMMARY AND FUTURE WORK	141
4.1 SUMMARY	141
4.2 FUTURE WORK	145
REFERENCES	149

CHAPTER 1: SEA ICE AND CLOUDS IN THE ARCTIC CLIMATE SYSTEM

The Arctic climate system involves complex interactions between the atmosphere, land surface, and the sea-ice-covered Arctic Ocean (Figure 1.1). This highly varying landscape, with an extreme seasonal cycle in solar radiation, has an important role in the global climate system, notably as a heat sink in the Northern Hemisphere. Observed changes in the Arctic have emerged and projected climate trends are of significant concern (Solomon et al., 2007). Surface warming over the last few decades is nearly double that of the entire Earth (Figure 1.2). Reduced sea-ice extent (Figure 1.3) and volume, changes to ecosystems, and melting permafrost are some examples of important and apparent changes in the region.

The Arctic climate is strongly influenced by the overall hemispheric circulation. During winter, the equatorial regions receive more solar radiation than the poles, which leads to uneven heating (Figure 1.4). This results in a meridional temperature gradient that generates an atmospheric and oceanic net poleward transport of energy, which counteracts the heating imbalance. A change in the meridional temperature gradient can alter the energy transport. As an example, high-latitude storms are more intense during winter than in summer, mainly due to the stronger meridional temperature gradient. On the other hand, changes in heat and moisture transport can alter the incoming shortwave and outgoing longwave radiation through their effects on water vapor and clouds. A change in temperature impacts the amount of emitted and absorbed longwave radiation directly. Advection of moisture has the potential to alter the amount of clouds, which affect both shortwave and longwave radiation. On seasonal time scales, there is a

close balance between the loss (gain) of radiative energy at the top-of-the-atmosphere and the gain (loss) of energy by meridional transport.

The large-scale energy budget of the Arctic was reviewed by Serreze et al. (2007). Figure 1.5 is a schematic of the Arctic energy budget during January and July, adapted from Frohner et al. (2007). They computed the energy budget over the polar cap (poleward of 70°N) using the ERA-40 reanalysis from the European Center for Medium-Range Weather Forecasts dataset. At the surface, the radiative terms dominate the surface energy budget in both winter and summer. At the top of the atmosphere, the loss of longwave (LW) radiation is 231 Wm⁻² in summer and 178 Wm⁻² in winter, while the summer net shortwave (SW) radiation flux is 241 W m⁻² downward. Of course, there is no solar radiation during winter. Energy transport from lower latitudes into the Arctic (given by $\nabla \cdot \mathbf{F}$) is about the same for summer and winter, 80–90 Wm⁻². These radiative and advective transports give a net energy storage in the Arctic Ocean mixed layer ($\frac{\partial O_E}{\partial t}$) of 105 W m⁻² in summer, associated with sea ice melt and sensible heat gain. In winter, the surface has a net loss of 52 W m⁻² due to ice growth and sensible heat loss. In winter, the radiative loss at the top of the atmosphere is about equal to the sum of the contributions from radiative loss at the surface and horizontal advection.

The seasonal cycle of sea level pressure over the Arctic and sub-arctic exhibits a maximum in late spring, a minimum in winter, and a weak secondary maximum in late autumn. Prominent features of autumn and winter are the mean Icelandic and Aleutian Lows in the northern North Pacific and northern North Atlantic, respectively, and the Siberian High over northern Eurasia. The summer pattern is flatter. The mean July field shows weak low pressure

over the central Arctic Ocean. Mean lows reflect the presence of cyclones in the region. The climatological seasonal cycle of sea level pressure are largely determined by the passage of migratory cyclones and anticyclones, which are associated with storminess patterns. These circulations carry heat, momentum, and moisture into the Arctic and have a significant influence on high-latitude climate (e.g. Serreze and Barry, 2014; ACIA ,2005).

Sea ice is an important factor in the energy deficit at high latitudes due to its high surface albedo; it significantly enhances the temperature gradient between mid-latitudes and the Arctic. Variations in sea-ice extent therefore have a significant impact on the heat budget of the atmosphere and oceans, and the meridional energy transport. For this reason, it is important to understand recent changes and variability of the sea-ice cover. The perennial sea-ice cover is one of the most unique and important features of the Arctic climate system. During winter, sea ice covers about 15.6 million km², extending over the entire Arctic Ocean and parts of the adjacent seas. In summer, the area covered by sea ice is significantly reduced; the sea-ice minimum is reached in September, when the sea-ice extent decreases to about 6.0 million km² (lower in recent years). Sea-ice growth and melt depend largely on the heat exchange between the atmosphere, sea ice and the underlying ocean. Clouds, water vapor, and atmospheric constituents determine the downward shortwave and longwave radiation that reach the surface. Part of this energy is absorbed by the surface: practically all longwave radiation is absorbed immediately, while the amount of shortwave radiation absorbed depends on the surface albedo and the fraction of shortwave radiation that penetrates the ice. Turbulent fluxes of sensible and latent heat contribute to the surface energy exchange. The exchange of sensible heat leads directly to temperature changes; latent heat exchange is a temperature change due to the phase change of

water, such as evaporation. Sea ice represents an important interface between the atmosphere and the underlying ocean, as it controls the energy exchange between the two; for example, in winter sea ice isolates the relatively warm ocean water with its temperature of $\sim -2^{\circ}\text{C}$ from the cold Arctic atmosphere, which is occasionally as cold as -40°C . Changes and variations of the sea-ice thickness or extent can have a variety of impacts on the local Arctic and global climate (ACIA, 2005; Francis et al., 2009; Maslowski et al., 2012).

Clouds play a dominant role in regulating the energy budget of the planet. They are also integral to the atmospheric hydrological cycle. The surface energy balance requires net radiative heating to be balanced by turbulent fluxes of sensible and latent heat and thus determines the evolution of surface temperature and the cycling of water, which are key in climate change (Solomon et al., 2007). It is important to remember that the global-mean precipitation and evaporation rates, which are measures of the strength of the hydrological cycle, do not scale with Clausius-Clapeyron relationship (e.g., Held and Soden 2006; Betts 1998; Trenberth 1998). As the climate warms, water vapor in the atmosphere increases as a consequence of the increased saturation vapor pressure of water. McGuire et al., (2006) found that enhanced moisture and heat transport into the Arctic can lead to further amplification of warming from changes in atmospheric water vapor and/or cloudiness.

Arctic clouds have competing effects on the surface radiation budget. They warm the surface by increasing the downwelling longwave radiation. They also cool the surface by reflecting shortwave radiation, but the strength of this effect is strongly dependent on the surface albedo. These two effects are usually referred to as the longwave and shortwave components of

the surface cloud radiative forcing. In the Arctic, shortwave cloud forcing is important only during the summer, while longwave cloud forcing is strong during the entire year (Gorodetskaya and Tremblay, 2008). Clouds also play a major role in Arctic surface energy exchange, controlling the growth and melt of sea ice. At the same time the processes involved in the formation, maintenance and dissipation of cloud cover over the Arctic Ocean are thought to be strongly influenced by the sea ice itself.

Clouds remain a major source of uncertainty in climate models, both globally and in the Arctic (Boucher et al., 2013; ACIA, 2005). For example, Figure 1.5, from Eisenman et al., (2007) shows the inter-model spread in Arctic cloudiness from 20th Century simulations from IPCC AR4. Eisenman et al., (2007) reported that this spread in cloudiness is associated with a 40 Wm^{-2} inter-model range in downwelling longwave radiation incident at the surface, significantly impacting the surface radiation budget.

Numerous studies have examined the properties of Arctic clouds in the present climate and evaluated the ability of models to represent them (e.g., Inoue et al., 2006; Walsh et al., 2002, 2005; Walsh and Chapman, 1998; Curry et al., 1996). Vavrus et al., (2011b) pointed out that less attention has been focused on how anthropogenic climate change may affect clouds in the Arctic, the impact the clouds have on climate and the mechanisms involved. Wetherald and Manabe (1986) found that greenhouse warming leads to more Arctic cloudiness in the annual mean and seasonally, resulting in a positive longwave feedback. Curry et al., (1996) obtained similar results confirming that cloud increases lead to a positive feedback, assuming that the present relationship between cloud amount and temperature holds in the future. Miller and Russell (2002) extensively studied the energy budget of the present and future Arctic climate in a $2\times\text{CO}_2$

experiment and demonstrated that the general circulation model (GCM) produced substantial cloud increases. Holland and Bitz (2003) analyzed Arctic clouds using a suite of climate models and reported that polar amplification was significantly correlated with the wintertime cloud increase, when clouds are a warming mechanism. The effects of cloud changes on future Arctic climate were also addressed in a GCM study performed by Vavrus (2004), who found that cloud increases in high latitudes accounted for almost half of the simulated Arctic temperature increase under greenhouse forcing. Vavrus et al., (2011a) analyzed simulations of Arctic cloud amount in GCMs and concluded that the relationship between Arctic cloud changes and possible mechanisms, indicates that the simulation of local evaporation, which is strongly linked to temperature and sea-ice cover, is the most important process for determining the projected polar cloud response to greenhouse forcing.

Kay et al., (2008) found that in a warmer world sea ice will be thinner, and variations in the summertime atmospheric circulation and associated changes in clouds and shortwave radiation can play an increasingly large role in modulating sea-ice extent. Liu et al., (2012) conducted an observational assessment of the degree to which cloud cover responds to changes in Arctic sea ice. Their results show that a 1% decrease in sea-ice concentration leads to a 0.36–0.47% increase in cloud cover, suggesting that a further decline in sea-ice cover will result in an even cloudier Arctic. We can expect this have an even greater impact in future Arctic climate. Holland et al., (2012) examined the direct radiative effects of melt ponds in CCSM4 during a CO₂ induced warming scenario. They found that “pond forcing” increased in the CO₂ warming scenario as more surface melting enhanced melt pond coverage throughout the basin.

In addition to the extreme weather and climate conditions, a number of socio-economic issues influence the vulnerability of the Arctic and the communities in this region. From a socio-economic perspective sea ice serves as an important base for subsistence hunting for many Arctic native communities; for example, coastal communities build trails across shortfast sea ice, ice that is grounded to the underlying surface, to reach migrating whales (Druckenmiller et al., 2013). It also plays a substantial role for Arctic maritime activities, such as oil drilling and shipping. Therefore, it is essential to identify and track changes of the ice cover in order to allow for safe access and an adaptation of native communities (Eicken, 2013). The physical as well as the socio-economic implications require a more thorough understanding of critical processes governing the Arctic sea ice and climate.

Modeling recent Arctic climate change and projecting future Arctic change are challenges because of the complex nature of Arctic processes, including those associated with Arctic amplification and the sensitivity of radiative fluxes to changes in clouds and sea ice. In order to simulate the Arctic climate, models must accurately represent surface type and albedo, cloud amount, and cloud phase. This is also a challenge due to the lack of observations of the Arctic because of the extreme climate conditions.

Historically, GCMs have had difficulty representing the complicated nature of cloud processes. However, it is possible to better represent clouds and their subsequent processes through the implementation of a cloud resolving model (CRM). By embedding a CRM into each grid cell of a GCM, an approach termed “super-parameterization,” it is possible to perform explicit simulation of cloud and boundary layer processes (Randall et al., 2003). A key motivating factor for performing simulations with the super-parameterized model is that it

simulates water vapor and radiatively active cloudiness through mechanisms that are much closer to reality compared to the conventional, more highly parameterized models.

This dissertation is aimed at improving our understanding of how Arctic clouds interact with, and influence, the surface budget, how clouds influence the distribution of sea ice, and the role of downwelling longwave radiation in climate change. Figure 1.6 serves as a reference map as several of these regions will be used to describe locations in the Arctic. The main questions addressed in this dissertation are:

- What are the key interactions between the atmosphere and sea ice?
- What is the role of wintertime downwelling longwave radiation in future climate simulations of the Arctic under elevated concentrations of carbon dioxide?
- How do super-parameterization and better representations of microphysical properties influence simulations of the Arctic climate?

The remainder of this dissertation is structured as follows. In Chapter 2, we investigate the idea of Arctic amplification and the role of wintertime downwelling longwave radiation. Chapter 3 explores the effects of super-parameterization on the Arctic climate. Finally, in Chapter 4 we summarize the key findings and discuss future work.

1.1 FIGURES

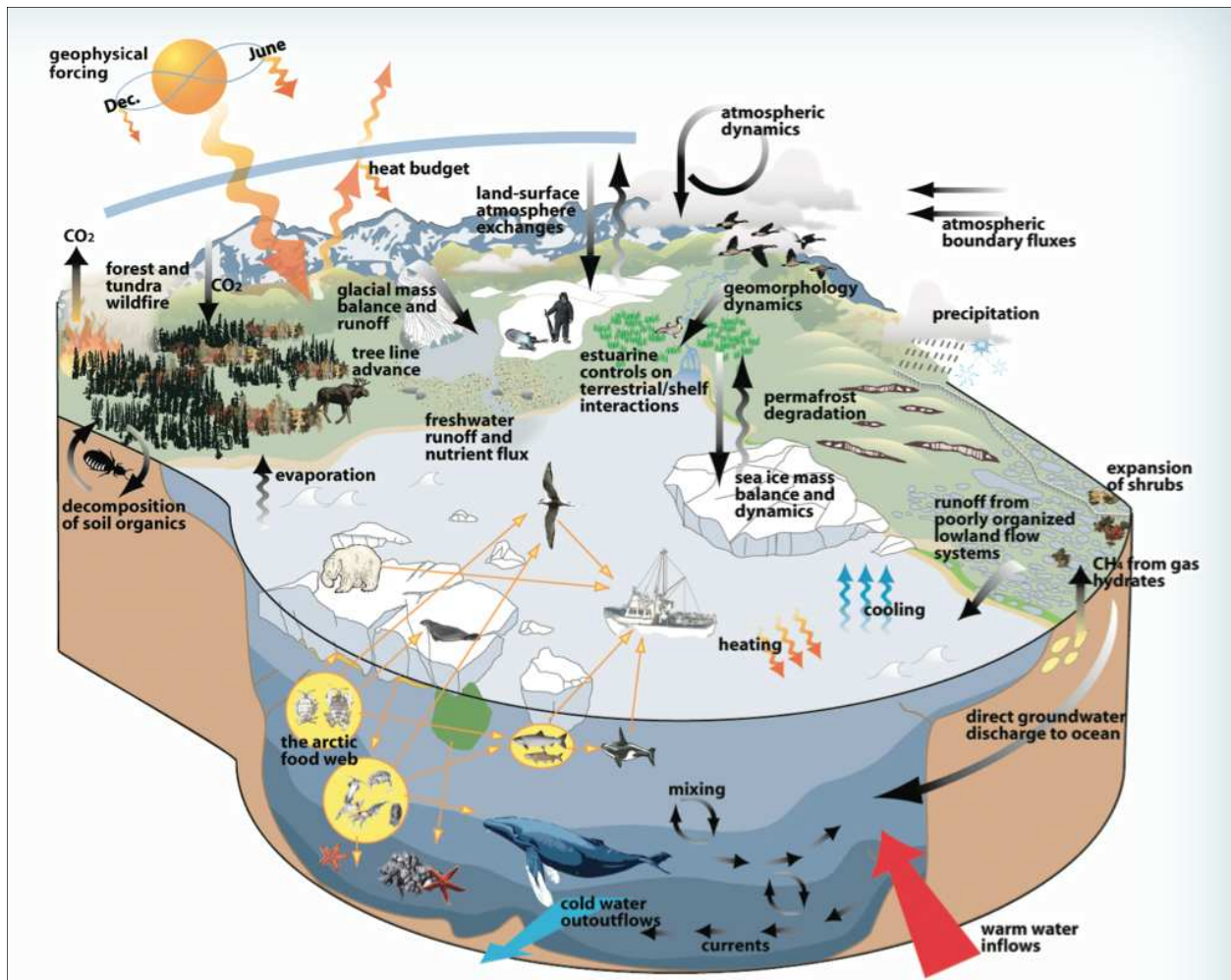


Figure 1.1. The Arctic climate system and its highly complex interactions. Adapted from Roberts et al., (2010).

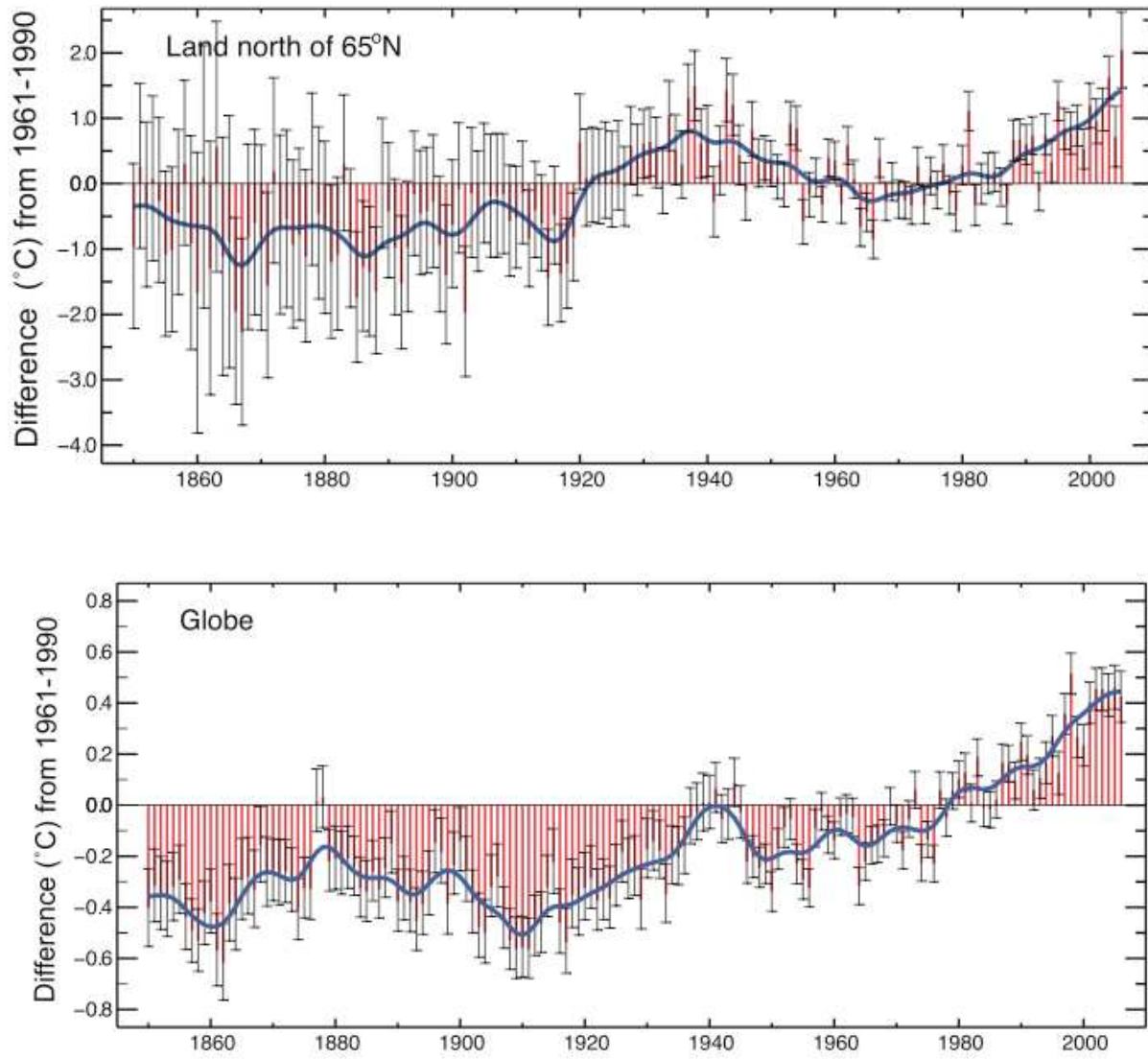


Figure 1.2. Global and Arctic annual land-surface air temperature anomalies relative to the 1961-1990 mean. Adapted from Solomon et al., (2007).

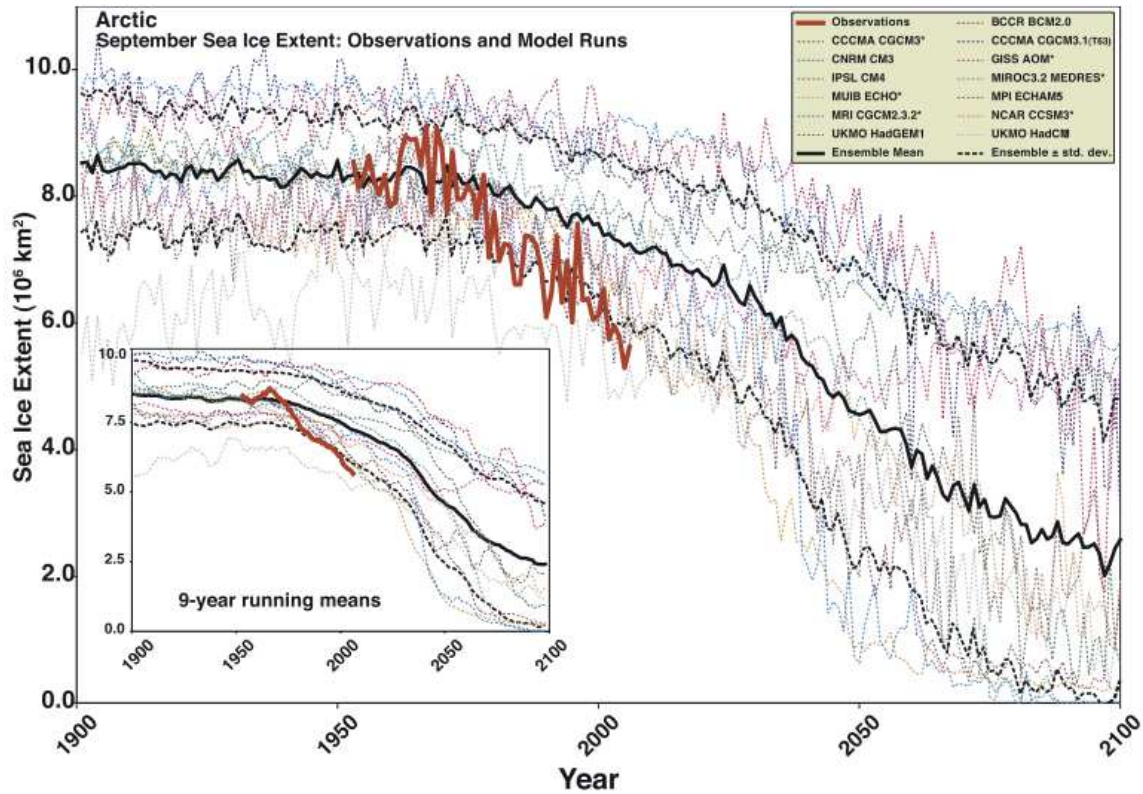


Figure 1.3. Arctic September sea ice extent ($\times 10^6 \text{ km}^2$) from observations (thick red line) and 13 IPCC AR4 climate models, together with the multi-model ensemble mean (solid black line) and standard deviation (dotted black line). Models with more than one ensemble member are indicated with an asterisk. Inset shows 9-year running means. Adapted from Stroeve et al., (2007).

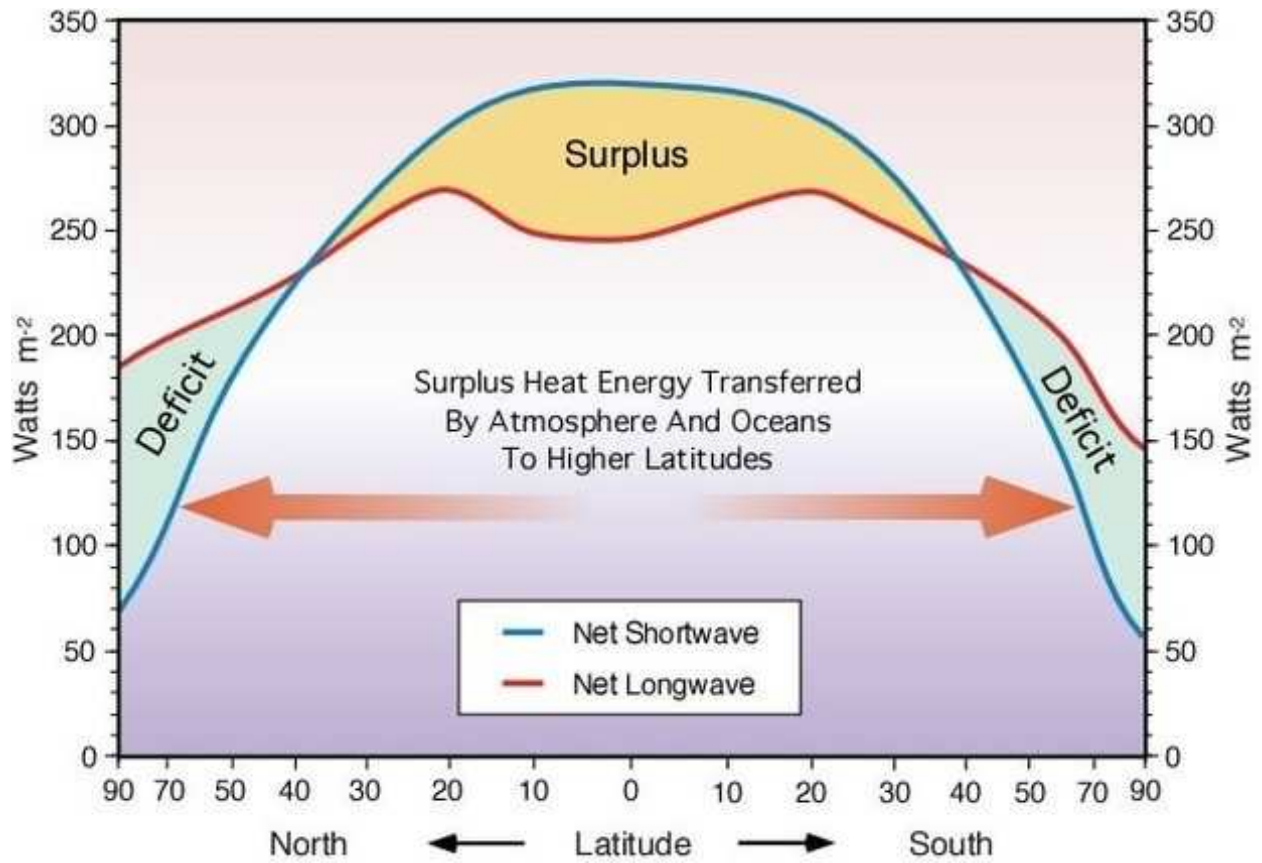


Figure 1.4. Energy balance of the Earth. The distribution of top-of-the-atmosphere net longwave and shortwave radiation. Adapted from NASA (2010).

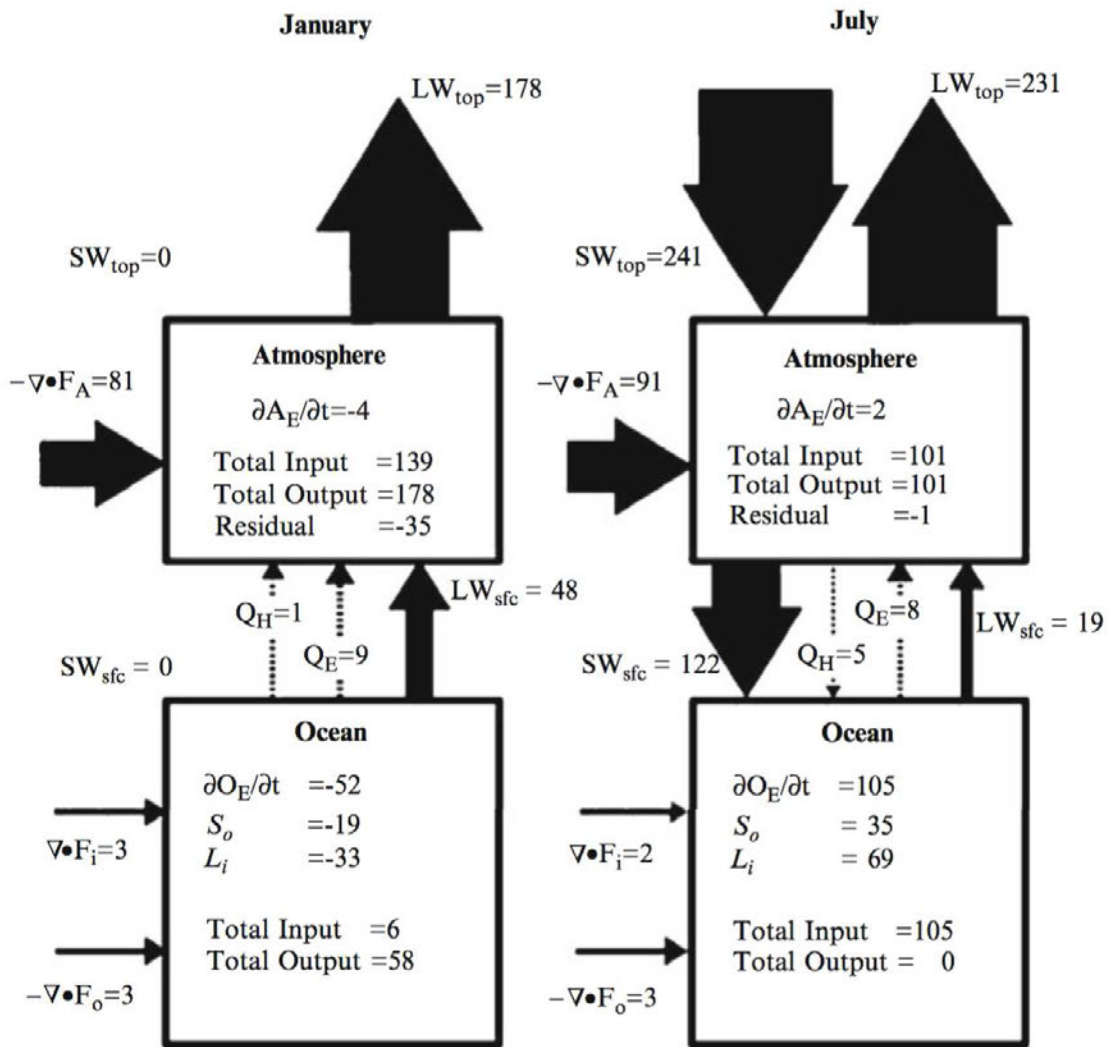


Figure 1.5. Schematic of the Arctic energy budget for January and July (Adapted from Serreze et al., 2007). Symbols are defined in the text. Units are in $W m^{-2}$. The width of the arrows is proportional to the size of the transports.

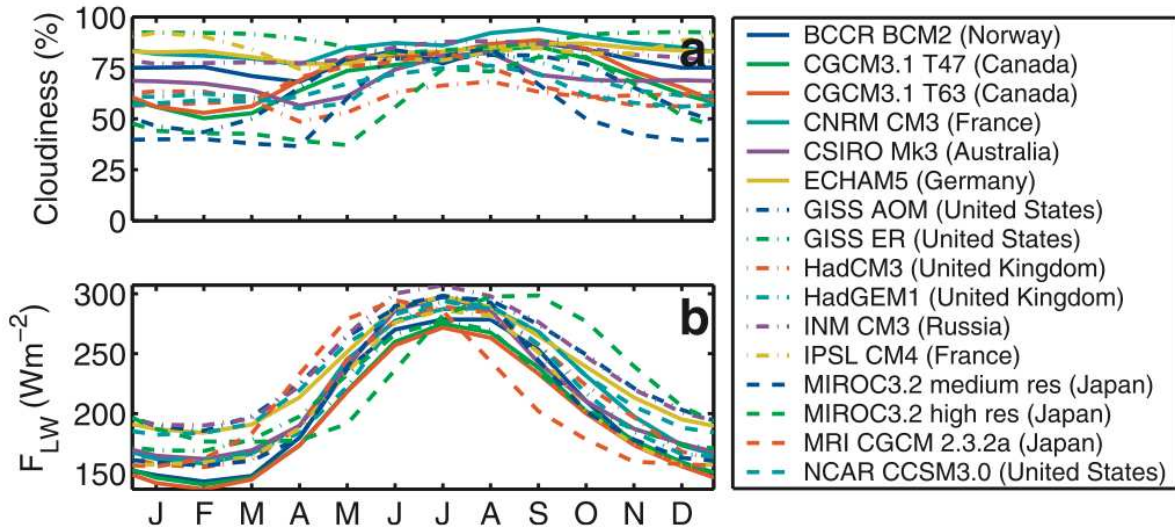


Figure 1.6. Simulated Arctic (70–90°N area average) 1980–1999 mean seasonal cycle in the “Climate of the 20th Century” GCM simulations for the IPCC AR4. (a) Total vertically integrated cloudiness. (b) Downward longwave radiation incident at the surface. Adapted from Eisenman et al., (2007).



Figure 1.7. Map of the Arctic Ocean and bordering countries from 60-90°N. (<http://geology.com/world/arctic-ocean-map.shtml>).

CHAPTER 2: THE EFFECTS OF DOWNWELLING LONGWAVE RADIATION ON ARCTIC AMPLIFICATION

The material presented in this chapter is based on Burt et al., (2016), with the exception of results shown in sections 2.1 and 2.2.5 which were added for the dissertation.

Burt, M. A., D. A. Randall, and M. D. Branson, 2016: Dark Warming, *J. Climate*, **29**, 705–719.

doi: <http://dx.doi.org/10.1175/JCLI-D-15-0147.1>

2.1 GLOBAL CLIMATE CHANGE

Before exploring Arctic climate change, we first set the stage by briefly analyzing the *global* climate response to elevated CO₂.

We performed a transient climate change simulation (i.e. a 1% per year increase in CO₂ until reaching 4xCO₂) with the Community Earth System Model (CESM). A detailed description of the CESM is given by Hurrell et al., (2013). We used the finite-volume dynamical core with a 1.9×2.5 degree latitude-longitude grid, and 30 levels. Microphysics was included using the available two-moment parameterization (Morrison and Gettelman 2008; Gettelman et al., 2008). The Rapid Radiative Transfer Model (Iacono et al., 2008) was used to calculate the radiative fluxes and heating rates. The Parallel Ocean Program (POP2) Ocean Model and the Los Alamos Sea Ice Model (CICE4) were run on the gx1v6 grid, which has a nominal resolution of 1° (Smith et al., 2010). CICE4 includes elastic-viscous-plastic sea-ice dynamics (Hunke and Dukowicz, 2002) and energy-conserving thermodynamics (Bitz and Lipscomb, 1999). It also includes the effects of multiple-scattering of shortwave radiation, an explicit simulation of melt pond

evolution, and the deposition and cycling of dust and black carbon (Hunke and Lipscomb 2008; Hurrell et al., 2013; Holland et al., 2012). CICE includes a simple melt-pond parameterization that simulates the pond volume and area as functions of the surface meltwater flux (Hurrell et al., 2013). These new capabilities allow for a more complete treatment of the surface albedo and shortwave radiative transfer in the ice and overlying snowpack (Holland et al., 2012).

The initial condition for our simulation was taken from an archived 500-year spin-up (CCSM4, 2° Pre-Industrial Control, case b40.1850.track1.2deg.003). For the first 25 simulated years, the CO₂ concentration was held constant at its pre-industrial value of 285 ppmv. This PI control was followed by 140 years of simulation during which the CO₂ concentration was increased by 1% per year until reaching four times its pre-industrial value (1139 ppmv). The CO₂ concentration was then held fixed for an additional 170 simulated years. Results presented are based on monthly averages over the last 25 years of the PI control and the 4xCO₂ simulations.

The global simulated surface temperature is presented here in two ways, first, through spatial maps based on annual and seasonal (annual (ANN), JJA (June-July-August), and DJF (December-January-February)) averages for the PI control and climate change (4xCO₂-PI Control) simulations (Figure 2.1a-f), and second through zonally averaged plots showing the change in temperature relative to the PI control (Figure 2.1g-i). The global mean and climate change values are also shown for PI control and 4xCO₂-Control. The Earth warms globally at 4xCO₂ by 5.6 K, with the greatest warming of 20-25 K at high latitudes of the winter hemispheres (Figure 2.1e-f). The atmospheric column warms from the surface through 100 hPa in the tropics and to 300 hPa in the high latitudes (not shown). At 4xCO₂, temperatures in the North Atlantic cool slightly (Figure 2.1d-f) which is associated with changes in the thermohaline

circulation (Otto-Bliesner et al., 2006). Figure 2.1g-i, shows that the surface temperature increases the greatest at high latitudes, especially in the Arctic, due to significant decreases in sea ice area.

With this warming, sea ice area decreases globally as shown in Figure 2.2d, with nearly 60% and 80% of the sea ice melting in the northern and southern hemispheres winters respectively. From Figures 2g-i, we can see that nearly half of the sea ice melts within the first 100 years of the simulation and only a small fraction persists throughout the remainder of the simulation.

As the air warms, the total column water vapor (shown in Figure 2.3) increases globally by 10.2 kg m^{-2} , with the greatest increases, as expected in the tropics. Although small in comparison to the tropics, water vapor in the high latitudes nearly doubles. This is important because water vapor is a greenhouse gas, which absorbs and emits longwave radiation.

The hydrological cycle strengthens at $4x\text{CO}_2$ with increases in total precipitation (Figure 2.4) and surface evaporation (Figure 2.5). Precipitation increases (decreases) on the southern (northern) side of the Inter-tropical convergence zone (ITCZ) in the eastern Pacific. Surface evaporation increases, and is greatest in regions where sea ice has melted and along the western coasts of South America and the eastern Pacific warm pool. Analysis of a few CMIP5 models from IPCC AR5 have a similar precipitation pattern at $4x\text{CO}_2$. There is a significant decrease in annual evaporation over the North Atlantic Ocean, due to the changing thermohaline circulation and colder surface temperatures.

Globally the percentage of the Earth covered by clouds decreases by 2.5% as presented in Figure 2.6. The Arctic becomes 5-10% cloudier and increased cloudiness is present along the

western boundary currents of Africa, Europe and over the eastern Pacific. Shortwave and longwave cloud forcing are presented in Figure 2.7 and 2.8 respectively. Total cloud radiative forcing (defined as shortwave plus longwave cloud forcing) decreases annually at 4xCO₂ (Figure 2.9). From Figures 2.7-2.9, we find that the clouds act to cool over the oceans and warm over the land. During winter at 4xCO₂, the clouds warm the atmosphere particularly in the Arctic and between 30°-60°S.

2.2 DARK WARMING

We now turn our attention to the impacts of dark-season¹ surface radiative processes in CO₂-induced Arctic climate change.

2.2.1 INTRODUCTION

In recent decades, the Arctic surface air temperature has been rising nearly twice as fast as the global mean (e.g., Stroeve and Meier 2012; Serreze and Barry 2011; Screen and Simmonds 2010a). This “Arctic amplification” is a robust feature of climate simulations with enhanced CO₂ (e.g., Manabe and Wehner 1975, 1980; Hansen et al., 1984; Holland and Bitz 2003; Lu and Cai 2010). The Fifth Assessment Report of the Intergovernmental Panel on Climate Change projects that anthropogenic warming over the Arctic will continue as the Arctic sea ice decreases in extent and thickness (Bindoff et al., 2013).

The high albedo of the sea ice limits the amount of solar radiation absorbed by the surface. As Arctic snow and ice melt, the dark ocean absorbs more of the sun’s energy during the summer months (Figure 2.10). This well known positive ice-albedo feedback is an important

¹ We use the term “dark season” to refer to the months when little or no solar radiation reaches the Arctic.

cause of Arctic amplification (e.g., Manabe and Wetherald, 1975; Hall, 2004; Winton, 2006; Serreze and Barry, 2011). During winter, solar radiation is absent and the main effect of the sea ice is to insulate the atmosphere from the relatively warm sea water below the ice. Decreases in ice thickness and extent reduce this insulating effect, and so can lead to a warming of the air near the surface

Hall (2004) found that the ice-albedo feedback accounts for only about half of the Arctic surface temperature increase associated with a CO₂-induced warming; similar conclusions were reached by Graversen and Wang (2009) and Graversen et al., (2014). These authors inferred that changes in sea-ice thickness and extent account for much of the remainder of the warming, consistent with earlier studies by Manabe and Stouffer (1980) and Robock (1980). Numerous studies have pointed to the importance of feedbacks involving water vapor (Ghatak and Miller, 2013; Graversen and Wang, 2009) and clouds (Winton, 2006; Francis and Hunter, 2007; Pithan and Mauritsen, 2014; Schweiger et al., 2008; Vavrus, 2004; Graversen and Wang, 2009).

Leads in the ice expose the warm ocean water to the cold atmosphere, and allow sensible heat and water vapor to enter the atmosphere, but in the present climate open water occupies only a small fraction of the Arctic Ocean during winter. As a result, longwave radiation is the main driver of the surface energy budget in winter. Recent work (e.g., Winton, 2006; Graversen and Wang, 2009) suggests that warming-induced increases in the surface downwelling longwave radiation (hereafter, DLR) are even more important than the ice-albedo feedback.

Previous analyses of observations (e.g., Walsh and Chapman, 1998; Francis and Hunter, 2007; Gorodetskaya and Tremblay, 2008; Lee et al., 2011), atmospheric reanalyses (e.g., Walsh

and Chapman, 1998; D.-S. Park et al., 2015; H.-S. Park et al., 2015), and modeling studies (e.g., Zhang et al., 1996; Abbot et al., 2009; Graverson and Wang, 2009) have shown the importance of increased DLR for Arctic amplification. Walsh and Chapman (1998) showed that during the polar night, the surface air temperature over sea ice increases when the DLR increases. A recent observational study by D.-S. Park et al., (2015) investigates the mechanisms that lead to increases in the DLR; later in this paper we compare our numerical results with their observational results.

Increases in the DLR can be partly due to increases in atmospheric water vapor, which in turn can be due to an increase of both local evaporation and transport from lower latitudes (e.g., Trenberth et al., 2005; Rinke et al., 2009; Jakobson and Vihma, 2010; Kurita, 2011, Di Biagio, 2012). As the sea ice retreats during spring and summer, and slowly reforms during autumn, an enhanced latent heat flux from the ocean surface to the atmosphere leads to a moistening of the Arctic lower tropospheric (Screen and Simmonds, 2010b; Ghatak and Miller, 2013). Kurita (2011) analyzed water isotopes as a proxy for the source region of water vapor and found a seasonally varying mixture of local and remote origins, with the local source dominating during late fall and early winter.

Simulations of climate change robustly project increases in the transport of water vapor into the Arctic, primarily during summer and autumn (Zhang et al., 2012; Bintanja and Selten, 2014), largely due to the increased water vapor content of the warmer air (Held and Soden 2006; Bengtsson et. al., 2011). Changes in the winds can also influence moisture transport into the Arctic, however, as discussed by Higgins and Cassano (2009), Skific et al., (2009 a, b) and Skific

and Francis (2013). Their results suggest that up to 25% of the future changes in moisture transport during summer into the Arctic can be attributed to changes in the circulation, rather than changes in atmospheric humidity. In the 2xCO₂ simulations of Vavrus et al., (2011a), increased Arctic water vapor results from both enhanced local evaporation and increased transport from lower-latitudes.

The DLR can also increase due to changes in cloudiness. As is well known, clouds strongly influence the surface fluxes of both shortwave and longwave radiation, and so changes in the clouds can influence the melting of snow and ice in the Arctic (Curry and Ebert, 1992). An observational study by Kay and Gettelman (2009) suggests that, in the current climate, year-to-year variability in Arctic cloudiness during early fall is controlled by year-to-year variability in the large-scale atmospheric circulation and the position of the sea-ice edge. Abbot and Tziperman (2008a, b), Abbot et al., (2009), Leibowicz et al., (2012), and Arnold et al., (2014) have proposed a positive wintertime feedback between convective clouds and Arctic sea ice loss. Walsh and Chapman (1998) and Gorodetskaya and Tremblay (2008) showed that clouds warm the surface by increasing the DLR, which can enhance sea ice melt and extend the melting season. Francis et al., (2005) suggested that “the relationship between DLR and ice edge position is also two-way. Additional open water will likely be warmer than the ice it replaced, and thus be a stronger emitter of longwave radiation. Cloud bases would absorb this energy, warm, and emit more radiation toward the surface. This relationship is a positive feedback in the system.”

The purpose of the present study is to investigate feedbacks that favor Arctic amplification during the dark winter season. We use a transient climate change simulation to address the following questions:

1. How do changes in the DLR interact with changes in the extent and thickness of the sea ice?
2. How do changes in the large-scale atmospheric circulation interact with changes in the extent and thickness of the sea ice?

The remainder of this paper is organized as follows: Section 2.2.2 describes the climate model, experimental design, and reanalysis data used. Section 2.2.3 presents results from a simulation of future climate change, with an emphasis on local processes. Section 2.2.4 describes simulated changes in the circulation that are linked to Arctic amplification. A preliminary analysis with selected CMIP5 models is presented in section 2.2.5. The paper concludes with a summary of our findings.

2.2.2 METHODS

CESM 1.1.1

To address the impacts of dark-season surface radiative processes in CO₂-induced Arctic climate change, we performed a transient climate change simulation with version 1.1.1 of the Community Earth System Model, which uses CAM5 atmospheric physics. We chose the CESM for our study because it is a full-featured climate model that is freely available, and a great variety of climate simulation results produced with the CESM have been analyzed by many investigators. In particular, previous versions of the CESM have been extensively used for

studies of Arctic processes and climate change and have been shown to perform quite well (e.g., Jahn et al., 2012; Vavrus et al., 2011b; Deser et al., 2010).

Unless otherwise stated, the analysis and results presented in this study with CESM are based on monthly averages over the last 25 years of the PI control and the 4xCO₂ simulations. Our analysis focuses on the Arctic poleward of 70° N during NDJ (November-December-January).

ERA-Interim

As discussed later, we have compared some of our model results with the European Center for Medium Range Weather Forecasts ERA-Interim dataset (Dee et al., 2011), which has been extensively used to study the ongoing changes in the Arctic climate (e.g., Lindsay et al., 2014; Zygmuntowska et al., 2012; Serreze et al., 2012). ERA-Interim combines information from a multitude of observations (surface-based observations, upper-air soundings, and satellites) with information from a short forecast started from a previous analysis (Dee et al., 2011). This process takes into account the uncertainties associated with both the model and the various observations to create a “best estimate” of the historical state of the atmosphere. ERA-Interim uses four-dimensional variational data assimilation (4D-Var) and has a horizontal resolution of T255 (nominally 0.70°; Dee et al., 2011).

2.2.3 THE ICE-INSULATION FEEDBACK

Figure 2.11 presents the seasonally varying trends of the simulated Arctic-means of selected fields. In these “seasonal trend plots”, the years of the simulation run from left to right along the horizontal axis, and the months of the year run from bottom to top along the vertical

axis, starting with June and ending with May, so that December is about in the middle. For convenience, the differences between the 4xCO₂ simulation and the PI control are plotted separately, as a kind of summary, on the right-hand side of each panel. Before plotting, each calendar-month of data has been subjected to a 5-year running mean, to generate, for example, a five-year running mean of Januaries, and so on for each month of the year.

Panel a of Figure 2.11 shows that, as expected from earlier work (e.g., Pithan and Mauritsen, 2014; Serreze and Barry, 2011; Screen and Simmonds, 2010a; Holland and Bitz, 2003), the simulated surface warming is largest in winter, reaching about 20 K in December. In contrast, the June surface air temperature increases by only about 5 K. Panel b provides an explanation for the strong seasonality of the surface temperature change, in terms of the insulating power of sea ice. During the early part of the simulation, the sea ice is thin and gappy by the end of the summer, but becomes thick and uniform by late autumn. The thick winter ice acts as an efficient thermal insulator that allows the near-surface air to be much colder than the freezing point of sea water, which is about 271 K. The summer sea ice extent and thickness decline rapidly during the first 50 years after CO₂ begins to increase, and by the time of CO₂ quadrupling the ice is extremely thin or absent altogether from July to December -- half of the year. At 4xCO₂, the reduced sea ice extent and thickness imply a decrease in the insulating power of the ice. That is why the air above the Arctic Ocean has a temperature only slightly colder than 271 K, even in late autumn (panel a of Figure 2.11), when the area-averaged ice thickness is less than 20 cm (panel b of Figure 2.11).

To further explore the insulating power of the sea ice we turn to Figure 2.12. The top panel of the figure presents the relationship of ice thickness to the ocean-air temperature difference. As the sea ice gets thicker, the temperature difference between the air and the ocean gets larger. The flow of energy through the sea ice which is dependent on ice thickness is illustrated in the bottom panel of Figure 2.12. As the thickness of the ice increases, the temperature difference between the ocean and the air is greater, resulting in less energy (i.e. stronger insulation) flowing from the ocean through the ice into the atmosphere. We return to this point later.

As the air warms, the total column water vapor increases, nearly doubling in winter (Figure 2.11c). This is important because water vapor is a greenhouse gas, which absorbs and emits longwave radiation. Clouds are also longwave absorbers and emitters, and Figure 2.11d illustrates that Arctic cloudiness increases during most seasons, especially during winter. The greatest increases in cloudiness are in the middle and upper troposphere (not shown), and are associated with an inflow of moisture from lower latitudes, consistent with results of Vavrus et al., (2011a).

We now examine the various components of the surface energy budget, averaged over the Arctic. Panels e and f of Figure 2.11 show that the sensible and latent heat fluxes increase, especially during autumn and winter. These fluxes tend to warm and moisten the air, and may also contribute to the increase in cloudiness. Panel g shows that the net longwave radiation at the surface (defined positive upward) also increases modestly during winter. The net longwave radiation is of course the relatively small difference between the strong upward and downward longwave radiation streams. The upwelling longwave radiation (ULR) increases because the

surface itself is warmer, and the DLR increases due to warmer air temperatures, combined with increases in water vapor, cloudiness, and of course CO₂. Interestingly, as the climate warms the *net* surface longwave flux actually decreases during summer. The DLR and the ULR both increase during summer, but the DLR increases more, resulting in a decrease in the net longwave radiation. Panel h of Figure 2.11 shows that the DLR increases by a very large 80 W m⁻² during winter. This is several times larger than the increase in the surface latent heat flux. The spatial pattern of the increase in the wintertime surface DLR is shown in Figure 2.13a. The increase is greatest over the Arctic Ocean, but it is also substantial over northern Europe and North America. Figure 2.13b shows that during NDJ about 40 W m⁻² of the increase in DLR comes from the effects of clouds (computed as the difference between all-sky DLR and clear-sky DLR); the remainder is due to the clear-sky effects of temperature, water vapor, and CO₂. In other words, the clouds account for less than half of the increase in the DLR during winter.

Of course, the ice-albedo effect also contributes to the Arctic warming. Figure 2.11i shows that the solar radiation absorbed by the surface increases by 60 W m⁻² during summer. This is true even though summer cloudiness increases slightly, as shown in Figure 2.11d. Note, however, that the absorbed solar radiation does not increase after about year 80, because by then the summer sea ice has disappeared.

The changes in the energy budget of the Arctic atmosphere are shown in panels j, k, and l of Figure 2.11. By the end of the simulation, the net energy flux at the surface (defined positive downward) increases by 80 W m⁻² during the summer months, due to the drastically decreased

surface albedo, but during winter the rate at which the surface loses energy increases by about 40 W m⁻². This energy loss by the surface is of course an energy gain for the atmosphere.

At the top of the atmosphere (panel k) the lower surface albedo causes an increase in the net downward radiation in summer, but during winter there is little change. The combined effects of the changes in the net energy fluxes at the surface and the top of the atmosphere are shown in panel l of Figure 2.11. The figure shows that throughout the simulation, and at all times of year, the Arctic atmosphere is cooled by the combined effects of the diabatic fluxes at the surface and the top of the atmosphere. This of course implies that the Arctic receives a net inflow of energy from lower latitudes. As the climate warms, the net diabatic cooling of the atmosphere changes little in summer, but the diabatic cooling becomes weaker in winter by about 30 W m⁻². As a result, the net atmospheric energy transport into the Arctic from lower latitudes also becomes weaker during winter in the warmer climate. The weaker meridional energy transport is consistent with the reduced pole-to-equator temperature gradient of the 4xCO₂ climate. In summary, the strong warming of the Arctic atmosphere is associated with weaker diabatic cooling, rather than increased energy transport into the Arctic by the atmospheric circulation.

To further explore the DLR increase shown in Figure 2.11h, we define an effective atmospheric emissivity, ϵ_s , by

$$F_{\downarrow,afc} \equiv \epsilon_s \sigma T_s^4, \tag{2.1}$$

where $F_{\downarrow sfc}$ is the surface downwelling longwave radiation, σ is the Stefan-Boltzmann constant, and T_s is the surface air temperature. With this definition, the initial value for emissivity, ϵ_s , is 0.8. By linearizing the right-hand side of equation (1), we can separate the change in DLR into two parts:

$$\Delta F_{\downarrow sfc} \cong \Delta \epsilon_s \sigma T_s^4 + 4 \epsilon_s \sigma T_s^3 \Delta T_s, \quad (2.2)$$

Here we use a capital delta to denote differences between 4xCO₂ and the PI control. The first term on the right-hand side of (2) is the contribution to $\Delta F_{\downarrow sfc}$ from the change in the emissivity, and the second term is the contribution from the change in T_s . Panels a and b of Figure 2.14 show the spatial distributions of the two terms. Averaged over the polar cap (70°-90° N, and including all longitudes), the changes in the emissivity and temperature contribute 9.5 W m⁻² and 51.9 W m⁻², respectively, to the increase in the wintertime DLR at 4xCO₂. The sum of these is 61.4 W m⁻², 12.5 W m⁻² less than the actual change in DLR of 73.9 W m⁻². The discrepancy is due to the linearization used to obtain (2).

It is interesting that during the summer the increase in DLR is mostly due to an increase in the emissivity rather than the warming of the air. Again, the summer warming is relatively small.

As mentioned earlier, Figure 2.11g shows that the cooling of the surface by the *net* surface longwave radiation increases slightly in the 4xCO₂ climate, relative to the PI control, because the strong increase in the DLR is slightly outweighed by an even stronger increase in the ULR. How

should we think about cause and effect here? Suppose that an increase in the dark-season surface temperature, associated with a thinning of the ice, drove an increase in the ULR, but that somehow the DLR did not change. The result would be a very rapid cooling of the surface (and thickening of the ice), which would be incompatible with the posited surface warming. This shows that the warmer surface temperature and decreased ice extent and thickness *are made possible* by the increased DLR. We cannot say that the warming and melting are *caused* by the increased DLR, but they could not happen without it. The thinning and/or disappearance of the ice leads directly to stronger ULR and warmer air temperatures. The warmer air and increased emissivity cause an increase in the DLR, which in turn makes it possible for the ice to become even thinner. In this way, the changes in ice thickness and DLR are mutually reinforcing, and create a positive local thermodynamic feedback, which we call the *ice-insulation feedback*.

The DLR increase shown in panel h of Figure 2.11 is substantial throughout the year, and is strongest during winter. The increased solar radiation acts only during summer, and has reached its maximum by about year 150 of our simulation, when the summer sea ice disappears. Figure 2.15 shows that, averaged over the entire year, the DLR increases by about three times as much as the absorbed solar radiation.

We close this section with Figure 2.16, which shows in a very simple way that the zonally and annually averaged DLR increases much more strongly in the Arctic than anywhere else on Earth. This is partly because the Arctic warms more strongly than anywhere else on Earth. A second reason is that in the Arctic the water vapor increases from very small values in the PI

climate. In lower latitudes, a substantial amount of water vapor is already present in the PI climate, so that adding even more water vapor has a relatively weak effect on the DLR.

2.2.4 THE BIRTH OF A NEW MONSOON

We now show that, during winter, the large-scale atmospheric circulation in the Arctic responds to the changing climate state in such a way as to *reinforce* the ice-insulation feedback discussed above. The circulation changes discussed below are a secondary effect. We do not claim that they *cause* or trigger the ice-insulation feedback described in Section 2.2.3; if anything, the circulation changes (and the associated secondary feedback) *are promoted by* the ice-albedo feedback and the ice-insulation feedback.

The seasonal trend plot presented in Figure 2.17a shows the evolution of *the difference between the surface air temperature over the Arctic Ocean and the surface air temperature over the surrounding continents poleward of 60°N*. We used the region poleward of 60°N (rather than 70°N) in order to incorporate more land points in the calculation. The figure shows that at the start of the simulation, the ocean is colder than the land during spring and summer (March through September) and a few degrees warmer than the land during winter. By the end of the simulation, however, *the air above the Arctic Ocean during December is more than 15 K warmer than the air above the surrounding land*.

The strong thermal contrast between the warmer ocean and the surrounding colder land during winter leads to a decrease in sea-level pressure over the Arctic Ocean (Figure 2.17b) relative to the surrounding continents. This can be described as a “thermal low,” which is defined by the *Glossary of the American Meteorological Society* as “An area of low atmospheric pressure

near the surface resulting from heating of the lower troposphere and the subsequent lifting of isobaric surfaces and divergence of air aloft.” Figure 2.18a shows a map of the simulated NDJ sea-level pressure at 4xCO₂ and panel b shows the difference in simulated sea-level pressure between 4xCO₂ and the PI Control. At 4xCO₂, the wintertime sea-level pressure over the Arctic Ocean has decreased by several hPa relative to the PI control. As a result, the sea-level pressure has become lower over the Arctic Ocean than over the surrounding continents.

Observations suggest that similar changes are occurring in the real world. Panel c of Figure 2.17 shows the observed evolution, from 1979 to 2012, of the difference between the surface air temperature over the Arctic Ocean and the surrounding continents, from 60°N to the pole, as reported in the ERA Interim reanalysis. During the northern summer, the air over the continents is warmer than the air over the surrounding ocean. During winter, however, the air over the ocean is warmer than the air over the land, and the figure shows that this difference has intensified over the 33-year record, especially since 2000. Panel d shows the corresponding trends in the sea-level pressure difference between the Arctic Ocean and the surrounding continents. After about 2000, there is a hint of decreasing sea-level pressure over the Arctic Ocean during winter, relative to the surrounding continents. The statistical significance of the trends has been assessed using a two-tailed t-test as in the study of Screen and Simmonds (2010b). Both are found to be statistically significant at the 95% level during winter. In short, the reanalysis data show trends that are similar to those found in our simulation.

Panels c, d, and e of Figure 2.18 respectively show the 970 hPa winds overlaid on surface temperature for PI Control, 4xCO₂, and the difference between the 4xCO₂ simulation and the PI control. In the winter of the 4xCO₂ climate, the surface air temperature over the Arctic Ocean is

considerably warmer than the temperature over the neighboring continents; the temperature gradients are much weaker in the PI control. The tremendous warming over the Arctic Ocean at 4xCO₂ has largely reversed the sign of the meridional temperature gradient near the borders of the Arctic Ocean. Panels c and d of Figure 2.18 also show that in the regions of the Barents, Kara, and Beaufort Seas, the low-level flow from land towards the Arctic Ocean has intensified at 4xCO₂. Despite the sea-level pressure decreases in winter, the warming of the lower troposphere leads to geopotential height *increases* in the middle troposphere of the 4xCO₂ simulation (not shown). The dynamic response to Arctic warming thus has a baroclinic vertical structure, as previously reported in climate-change simulations analyzed by Deser et al., (2010) and Sun et al., (2015).

Figure 2.19 shows the simulated total diabatic heating of the atmosphere at several levels in the lower troposphere, for NDJ and for both the PI control and 4xCO₂. In the PI control (left column), the air over the Arctic Ocean is being diabatically cooled at all levels. This cooling is due to longwave radiation. In contrast, at 4xCO₂ (right column) the lower troposphere is weakly heated everywhere over the Arctic Ocean at the lowest levels. The heating is due to a combination of processes including vertical diffusion of sensible heat and latent heat release. The heating continues up to the 887 hPa level over the Barents and Chukchi Seas. Cooling occurs above that level. During summer, diabatic cooling is found at all levels in the lower troposphere over the Arctic Ocean (not shown).

In the PI control, strong wintertime diabatic heating occurs over the North Atlantic and North Pacific Oceans, mainly below the Arctic Circle. This sub-Arctic heating is associated with

the strong temperature contrasts between the continents and oceans in those latitudes, e.g., between eastern North America and the western North Atlantic Ocean, which can be seen in Figure 2.18. Figure 2.19 shows that the sub-Arctic heating is considerably reduced in the 4xCO₂ climate. The reason is that the land-sea temperature contrasts are much weaker, as can be seen in Figure 2.18.

In summary, at 4xCO₂ the Arctic circulation regime can be described as a weak and shallow *winter monsoon*, in which the low-level winds flow from the cold continents out over the much warmer Arctic Ocean. This monsoon circulation is a consequence of the Arctic warming, which is mainly driven by the combination of the ice-albedo feedback in summer and the ice-insulation feedback in winter. The winter-monsoon circulation can also act to enhance the Arctic warming, however, as described below.

The changes in vertically integrated total column water vapor shown in Figure 2.11c motivate us to examine the vertically integrated Arctic water vapor budget, in which the two source terms are surface evaporation and moisture transport from lower latitudes. Figure 2.20 shows seasonal trend plots of the sources and sinks of precipitable water due to precipitation (top panel), evaporation (middle panel), and moisture convergence (bottom panel). The moisture convergence has been diagnosed as a residual, taking into account the small tendency term (not shown). The Arctic-averaged moisture convergence and evaporation are both positive throughout the year, and for the whole duration of the simulation. As the climate warms, moisture convergence increases substantially in late summer, but it hardly changes during the remainder of the year. In contrast, evaporation increases during late autumn and early winter.

Figure 2.21a shows a map of the increase in surface evaporation during NDJ. As expected from Figure 2.20, evaporation has intensified over much of the region, especially over the Chukchi, Greenland and Barents Seas. In the warmer climate, the enhanced wintertime evaporation is of course associated with the increase in open water, but comparison of panels a and b of Figure 2.21 shows that is also promoted by an increase in the surface wind speed. The stronger winds are found over the Barents Sea, and north of Eurasia. Comparison with panels c, d, and e of Figure 2.18 shows that these are regions of strong land-sea thermal contrast and enhanced low-level flow from land to sea. We conclude that the stronger surface winds associated with the winter monsoon circulation are promoting enhanced evaporation over the (relatively) warm water; similar evaporation maxima are associated with the winter monsoons of lower latitudes.

Recall from panel c of Figure 2.11, that the vertically integrated water vapor content of the Arctic atmosphere increases for all months of the year, at $4xCO_2$. The results shown in Figure 2.20 suggest that, in our simulation, the moistening of the Arctic atmosphere in summer, at $4xCO_2$, is due to increased moisture transport from lower latitudes, but that the moistening in winter is due to increased surface evaporation. Figure 2.21 shows that the increased evaporation in winter is partly due to stronger surface winds, which are associated with the winter monsoon.

2.2.5 COMPARISON WITH CMIP5 MODELS

The results presented up to this point are based on a single climate model, namely the CESM. To investigate the model-dependence of our findings, we have examined output from six other climate models that participated in the Coupled Model Inter-comparison Project phase 5

archive (CMIP5, Taylor et al., 2012). The six models are CCSM4, GFDL-ESM2M, GISS-E2-R, HadGEM2-ES, MIROC5, and MPI-ESM-MR. Table 1 summarizes some basic properties of the six models. We used the “abrupt 4xCO₂” simulations from CMIP5, in which the models were run with pre-industrial CO₂ for 500 simulated years, and then responded to an instantaneous quadrupling. Only the first member of each ensemble (r1i1p1 in the CMIP5 protocol) has been analyzed. A detailed description of the experiments is given by Taylor et al., (2012).

Polar amplification is evident in Figure 2.22, which shows how winter Arctic (60° - 90° N) surface temperatures change, relative to the 25-year pre-industrial control, as the simulation progresses. The greatest warming occurs poleward of 70°N, with values ranging from 15-30 K, depending on the model. Warming is also substantial in the lower Arctic, from 60-70°N, but it is quite a bit weaker, with values ranging from 4-12 K. MIROC5 has the strongest warming, while GISS-E2-R has the weakest. The differences in warming over the Arctic Ocean are associated with differences in Arctic sea ice loss. The models with the most (least) sea ice loss have the strongest (weakest) warming (not shown). For each model, Figure 2.23 (left column) shows the difference in surface temperature between the ocean and land from the last 50 years of the PI control through the abrupt 4xCO₂ simulation. The results from the CMIP5 models are qualitatively similar to those from our simulations with CESM, as shown in Figure 2.11. At the end of the pre-industrial control, the ocean is colder by 4-10 K than the land from late winter (February) through summer (August/September). During winter (October-February), the ocean temperatures are within 2 K of the atmosphere for CCSM4, GFDL-ESM2M, and MIROC5, and warmer than the land by 2-6 K for HadGEM2-ES, GISS-E2-R, and MPI-ESM-MR. After adjustment to the quadrupled CO₂, the ocean is significantly warmer than the land from autumn

into spring. The most pronounced difference occurs in the HadGEM2-ES simulation, which has a warming of 4-10 K and the most extended seasonal ocean warming, from September through March. GFDL-ESM2M has the weakest and shortest seasonal warming (2-4 K, September through December). The surface warming is accompanied by moistening of the air. In the PI climate the winter Arctic atmosphere is extremely dry ($<1 \text{ g kg}^{-1}$). At $4\times\text{CO}_2$, the water vapor concentration nearly triples in the lowest two kilometers of the troposphere (not shown).

As a result of the strong temperature contrast between the Arctic Ocean and surrounding land, the sea level pressure decreases over the Arctic, as shown in Figure 2.22 (right column). Figure 2.23 (right column) presents the difference in surface pressure between the ocean and land from the PI control through the abrupt $4\times\text{CO}_2$ simulation. As in results shown with CESM, the CMIP5 models show a decline in surface pressure over the ocean at $4\times\text{CO}_2$. Surface pressure is lower in CCSM4 compared to the other model at the start of the simulation and the pressure continues to decrease at $4\times\text{CO}_2$. Figure 2.24 shows the spatial pattern of this pressure change. The simulated patterns of sea level pressure change differ considerably among the models, but generally have lower pressure over the ocean and higher pressure over land). MPI-ESM-MR has the strongest pressure decrease, about 20 hPa, over the central Arctic Ocean. CCSM4 has a well defined low over the North Slope of Alaska, while MIROC5 has a low over the Canadian Archipelago and Greenland. In contrast, HadGEM2-ES and MPI-ESM-MR have more of an elongated low pressure pattern over the central Arctic Ocean, with a deeper low in MPI-ESM-MR. GISS-E2-R and GFDL-ES exhibit dipole patterns with sea level pressure minima over the East Siberian Sea and Bering Strait and high pressure over Scandinavia. GFDL-ES has the strongest pressure increase, extending from North America to Northern Europe.

The simulated winter SLP changes are consistent with a shift towards positive polarity of the Arctic Oscillation identified by Thompson and Wallace (1998, 2000). This is consistent with a multi-model average of the CMIP3 models, in which a 21st-century decrease in the Arctic surface pressure is associated with a shift towards positive polarity of the Northern Annular Mode (NAM; Solomon et al., 2007). The CMIP3 multi-model analyses found that more than half of the models exhibit a positive trend in the NAM (Rauthe et al., 2004; Miller et al., 2006). Although the magnitudes of the trends vary considerably among the models, Miller et al., (2006) found that none of the 14 models exhibits a trend towards a lower NAM index or a higher Arctic SLP.

In addition to the shift towards lower wintertime Arctic surface pressure, we find changes in the near-surface winds. Figures 2.25a, 2.25b, and 2.26 illustrates the changes in the low level (925 hPa) wind fields, overlaid on the changes in the surface air temperature for the CMIP5 models, and can be compared with our CESM results as shown in Figure 2.18.

As in the results from CESM, decreased sea level pressure over the Arctic leads to low-level convergence and rising motion. Figures 2.27a and 2.27b shows that the strength of DLR increase varies among the CMIP5 models. CCSM4, MIROC5 and HadGEM2-ES have increases of about 100 W m^{-2} over the central Arctic, while GISS-E2-R produces “only” a 50 W m^{-2} increase. Clouds contribute between $10 - 30 \text{ W m}^{-2}$ to the DLR increase.

The changes in the energy budget of the Arctic atmosphere for the CMIP5 models are shown in Figure 2.28. By the end of the simulation, the net energy flux at the surface (defined positive downward) increases by $25-80 \text{ W m}^{-2}$ during the summer months, depending on the

model, with MIROC5 having the greatest increase. As with CESM, this is due to the drastically decreased surface albedo. During winter the rate at which the surface loses energy increases by about 40 W m^{-2} . This energy loss by the surface is of course an energy gain for the atmosphere. At the top of the atmosphere the lower surface albedo causes an increase in the net downward radiation in summer, but little to no change during winter. The combined effects of the changes in the net energy fluxes at the surface and the top of the atmosphere are shown in Figure 2.28 (right column). The figure shows that throughout the simulation, and at all times of year, the Arctic atmosphere is cooled (negative values) by the combined effects of the diabatic fluxes at the surface and the top of the atmosphere. The cooling is the strongest in HadGEM-ES, MIROC5, and MPI-ESM-2M. The cooling is apparent in CCSM4, GFDL-ESM2M and GISS-E2-R but is weaker. This implies that the Arctic receives a net inflow of energy from lower latitudes but the inflow becomes weaker during winter, similarly to CESM.

The vertically integrated water vapor content of the Arctic atmosphere increases for all months of the year, at $4x\text{CO}_2$ in the CMIP5 models and the results shown in Figure 2.29 suggest that, in these simulation, the moistening of the Arctic atmosphere in summer, at $4x\text{CO}_2$, is due to increased moisture transport from lower latitudes, but that the moistening in winter is due to increased surface evaporation, especially in simulations with HadGEM2, MIROC5, and MPI-ESM2M.

In summary, the CMIP5 simulations are broadly consistent with our CESM results.

2.2.6 DISCUSSION

Figure 2.30 summarizes the results presented in sections 2.2.3-2.2.5 of this chapter. The local ice-insulation feedback, shown in red in the figure, favors warming over the Arctic Ocean in winter. This leads to a reversal of the low-level meridional temperature gradient near the boundaries of the Arctic Ocean. The Arctic winter monsoon is a dynamical response to this reversed temperature gradient. The monsoon circulation is weak and shallow, and has only a qualitative resemblance to the powerful winter monsoons of the tropics, but it strongly contrasts with the pre-industrial Arctic winter circulation. Figure 2.31 summarizes the three feedbacks that we have shown to contribute to Arctic warming. The local ice-insulation feedback is the strongest feedback and is permanent, while the ice-albedo feedback is strong but temporary, as it will only operate as long as there is summer sea ice available to melt.

D.-S. Park et al., (2015; hereafter DSP) recently presented an observational study of the mechanisms that lead to decreases in Arctic sea ice concentration (SIC) during winter. They found that the chain of events begins with an intrusion of warm, humid, cloudy air into the Arctic from lower latitudes. The resulting increases in humidity, cloudiness, and temperature drive an increase in the DLR, which then leads to a decrease in the SIC and an increase in the sea surface temperature. The reduced SIC allows an increase in the surface sensible and latent heat fluxes. Based on these results, DSP concluded that reductions in SIC are primarily caused by intrusions of warm, humid air into the Arctic, associated with large-scale dynamical interactions between the Arctic and lower latitudes, and that the increased humidity is caused by meridional moisture transport rather than stronger surface evaporation. Although the various observed fluctuations discussed by DSP occur on the time scale of days to weeks, they suggested that the observed

multi-decadal decline in SIC is associated with similar causal mechanisms involving changes in large-scale dynamics and the resulting changes in the transport of warm, humid air into the Arctic. This would imply that Arctic amplification is substantially driven by dynamical interactions with lower latitudes. H.-S. Park et al., (2015) suggest that such interactions can involve convective disturbances in the tropics.

The processes at work in our climate-change simulation are different from those described by DSP. As shown in Section 2.2.3, the simulated Arctic warming in winter is primarily due to a weakening of the diabatic cooling of the Arctic atmosphere; the energy transports from lower latitudes actually decrease during winter, as the climate warms. We also showed, in Section 2.2.4 with CESM and Section 2.2.5 with the CMIP5 models, that the simulated moistening of the Arctic atmosphere during winter is primarily due to an increase in surface evaporation, rather than an increase in poleward moisture transport. Our results do not necessarily contradict those of DSP, because we have analyzed simulated climate change on century time scales, while they studied observations of Arctic variability in the present climate.

2.3 SUMMARY

As the Arctic sea ice thins and ultimately disappears in a warming climate, its insulating power decreases. This causes the surface air temperature to approach the temperature of the relatively warm ocean water below the ice. The resulting increases in air temperature, water vapor and cloudiness lead to an increase in the surface downwelling longwave radiation (DLR), which enables a further thinning of the ice. This positive ice-insulation feedback operates mainly

in the autumn and winter. In our climate change simulations, the increase in Arctic DLR is three times stronger than the increase in Arctic absorbed solar radiation at the surface.

The warming of the surface air over the Arctic Ocean during fall and winter creates a strong thermal contrast with the colder surrounding continents. Sea-level pressure falls over the Arctic Ocean, and the high-latitude circulation reorganizes into a shallow "winter monsoon." The resulting increase in surface wind speed promotes stronger surface evaporation and higher humidity over portions of the Arctic Ocean, thus reinforcing the ice-insulation feedback.

Our study has been based on a transient CO₂-warming simulation with the CESM, and the results are of course model-dependent. We performed a preliminary analysis of the "instantaneous quadrupling" experiments in the CMIP5 archive, and find that many but not all of the CMIP5 models produce results similar to those reported here. Further research is needed to quantify and understand the model-dependence of our results.

In the next chapter, we explore the effects of super-parameterization on the Arctic climate.

2.4 FIGURES

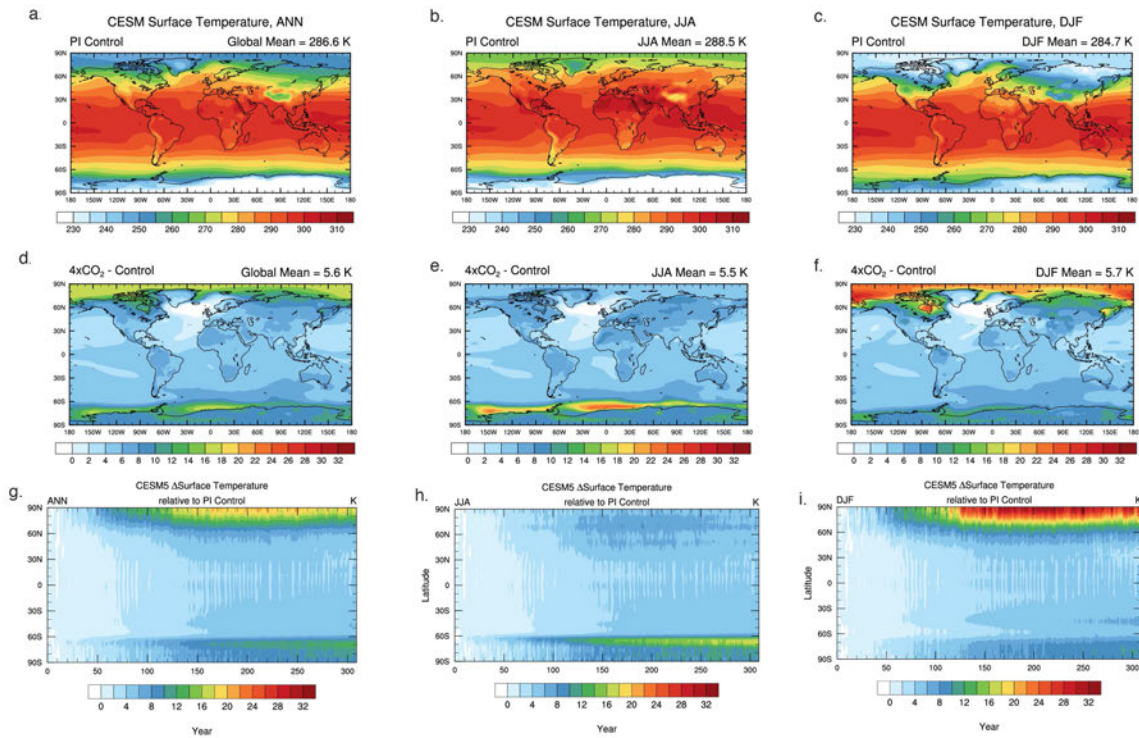


Figure 2.1. Panels a-f: Global maps of annual and seasonal simulated surface temperature (K) for the PI control and climate change (4xCO₂ minus PI Control). Panels g-i: Latitude-time plot of the climate change (4xCO₂ minus PI Control) for surface temperature (K, zonally averaged) relative to the mean of the 25-year control.

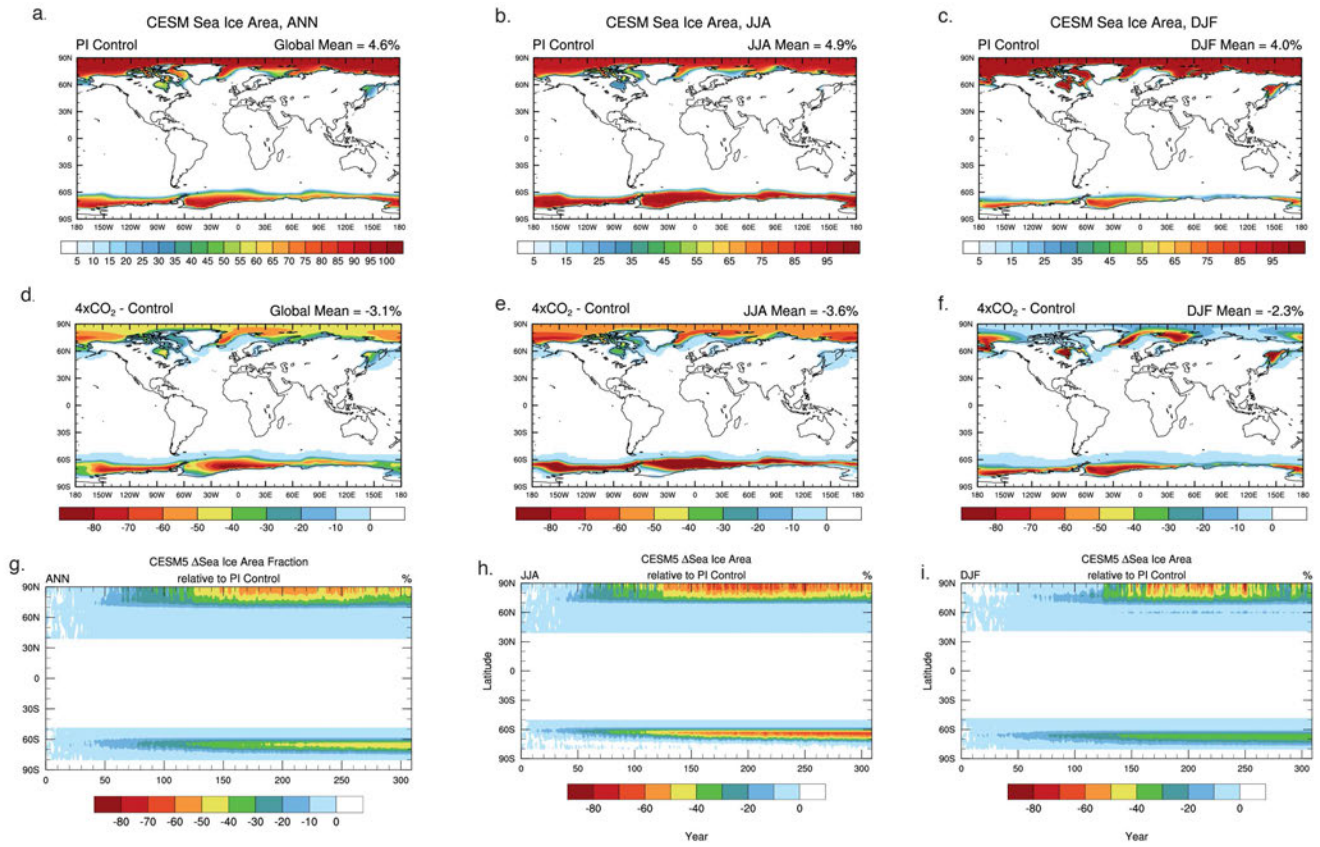


Figure 2.2. As in Figure 2.1, but for sea ice area (%).

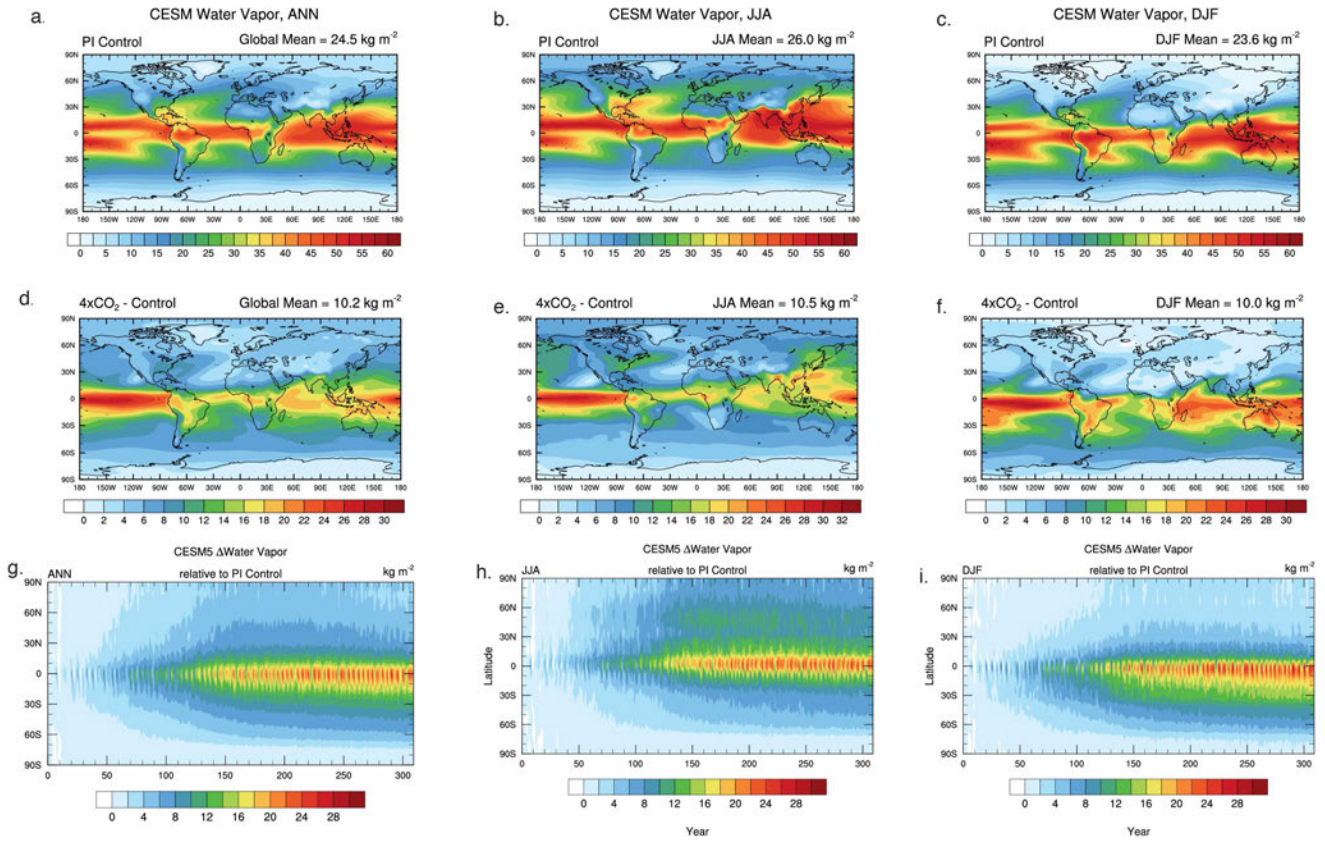


Figure 2.3. As in Figure 2.1, but for vertically integrated water vapor (kg m⁻²).

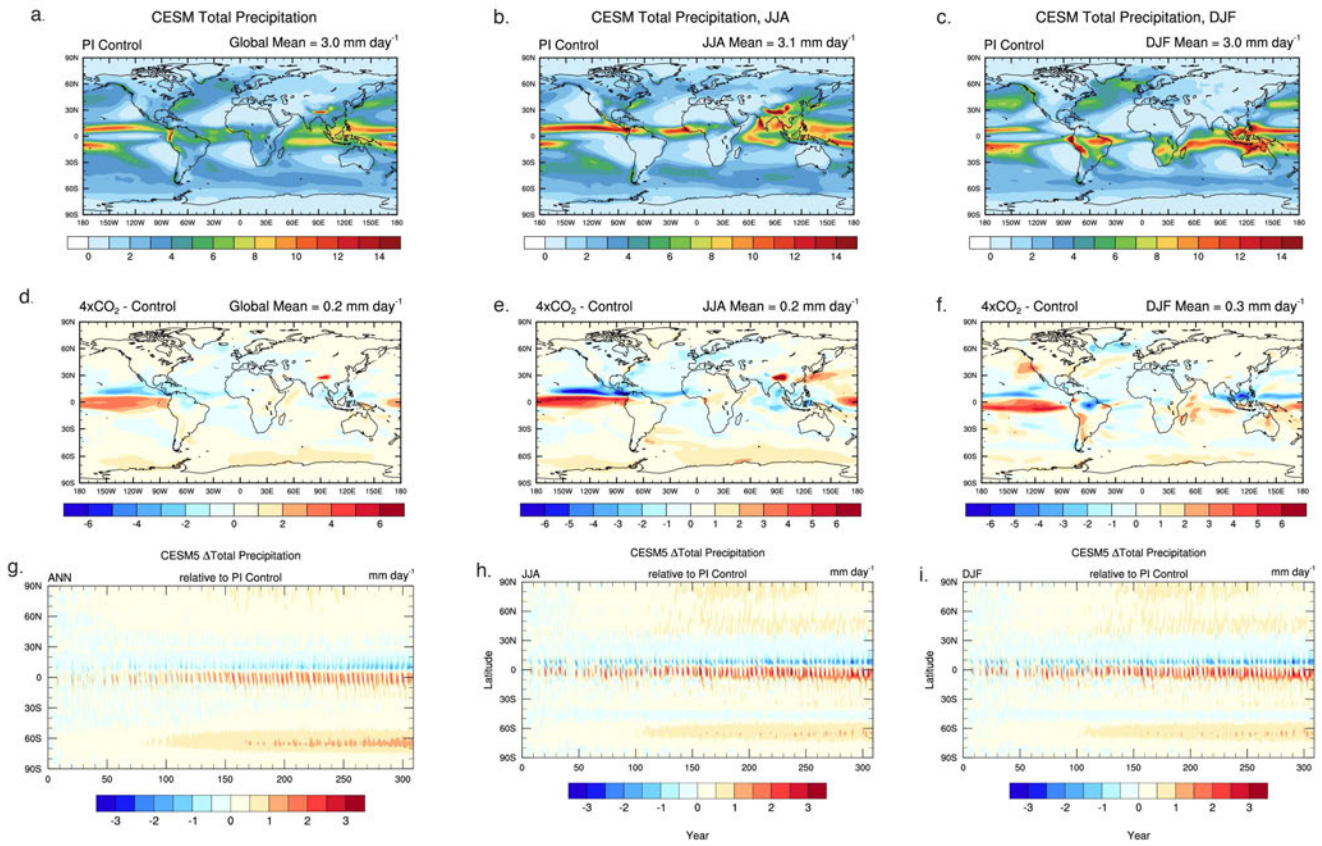


Figure 2.4. As in Figure 2.1, but for total precipitation (mm day⁻¹).

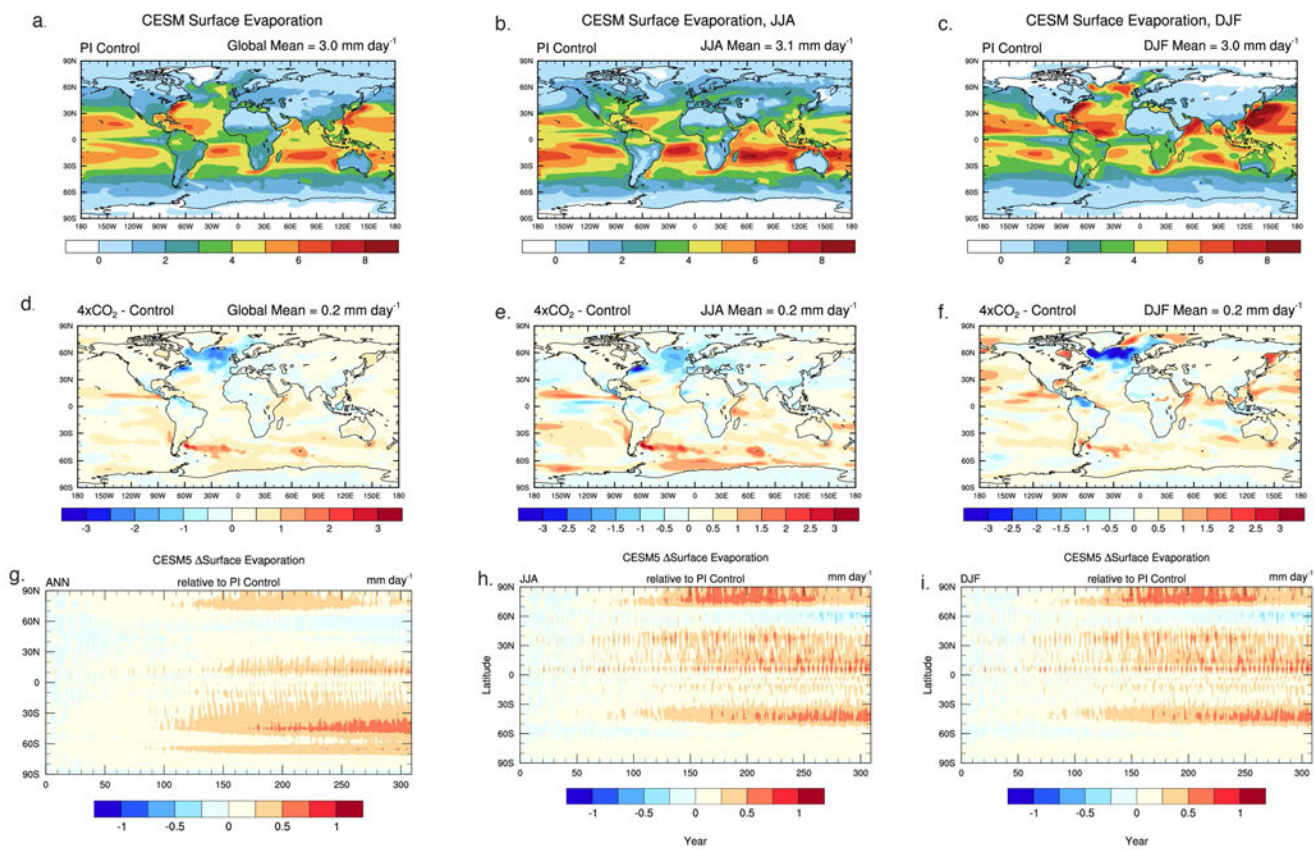


Figure 2.5. As in Figure 2.1, but for surface evaporation (mm day⁻¹).

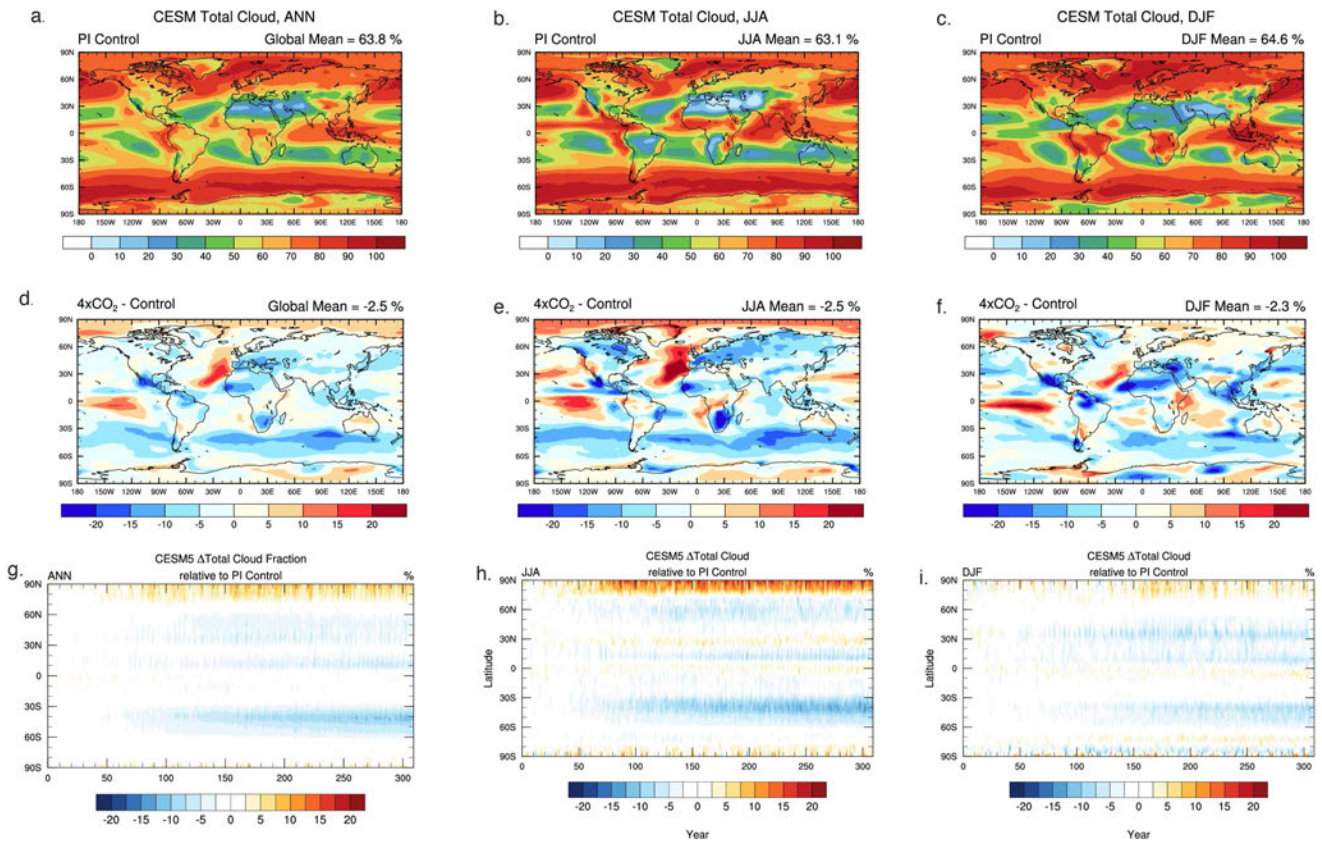


Figure 2.6. As in Figure 2.1, but for total cloud (%).

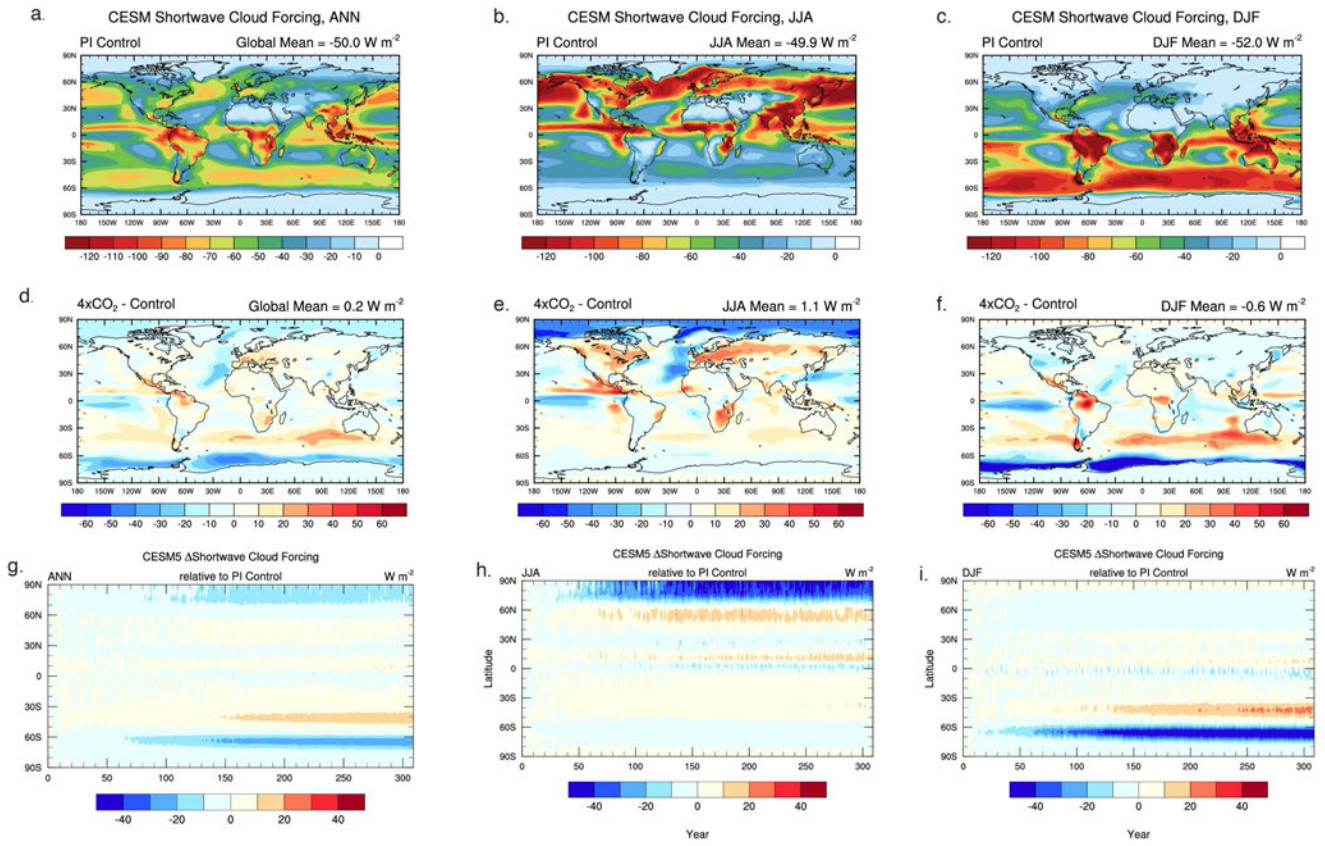


Figure 2.7. As in Figure 2.1, but for shortwave cloud forcing (W m^{-2}).

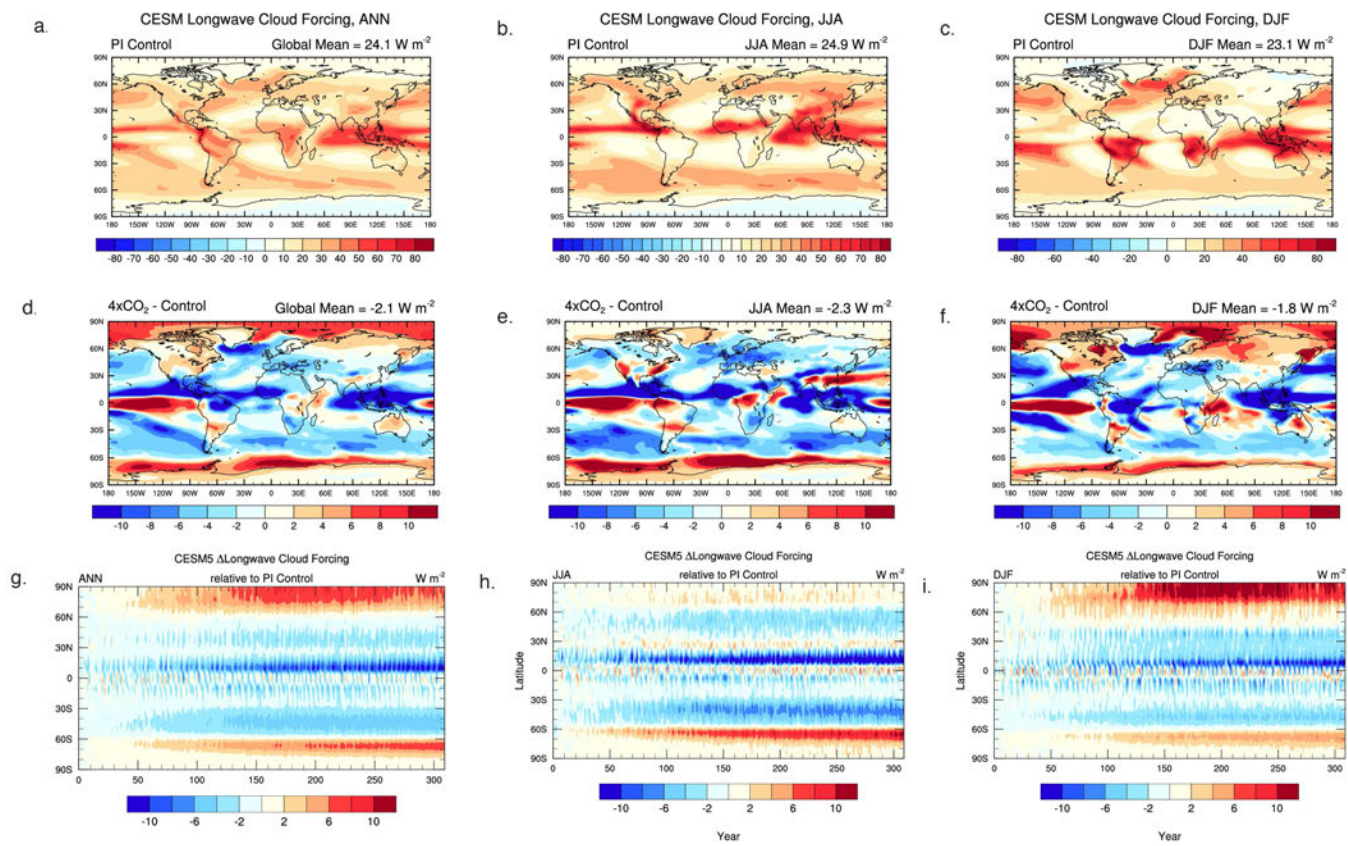


Figure 2.8. As in Figure 2.1, but for longwave cloud forcing ($W m^{-2}$).

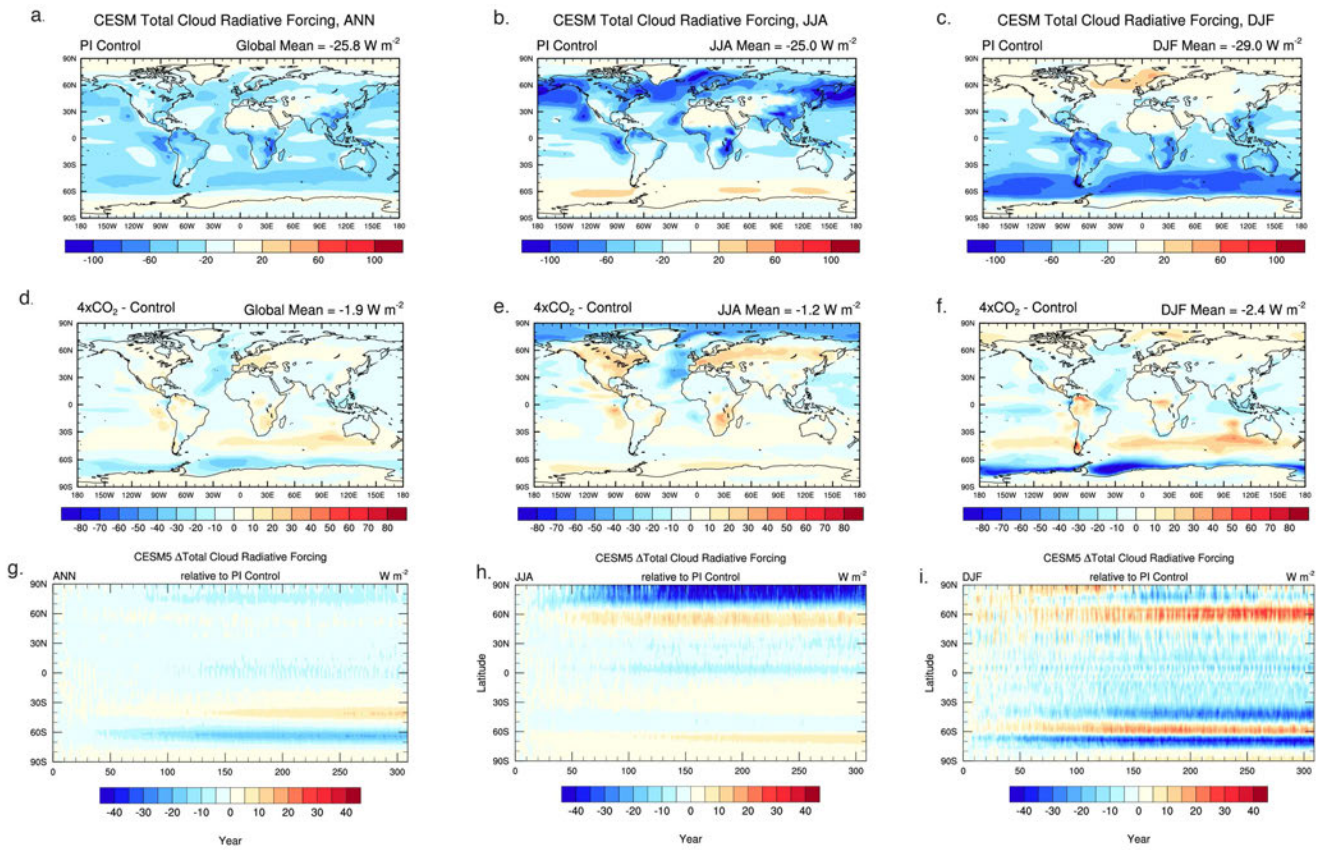


Figure 2.9. As in Figure 2.1, but for total cloud radiative forcing (SWCF plus LWCF, $W m^{-2}$).

Ice-Albedo Feedback (Summer Only)

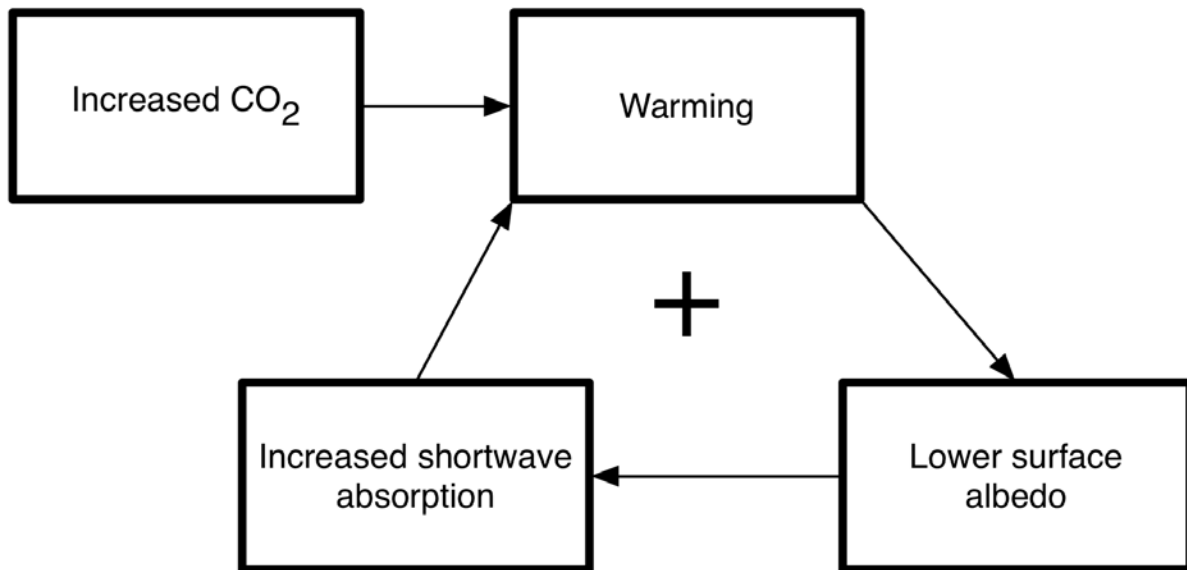


Figure 2.10. Schematic of the ice-albedo feedback, which is only active during the summer months.

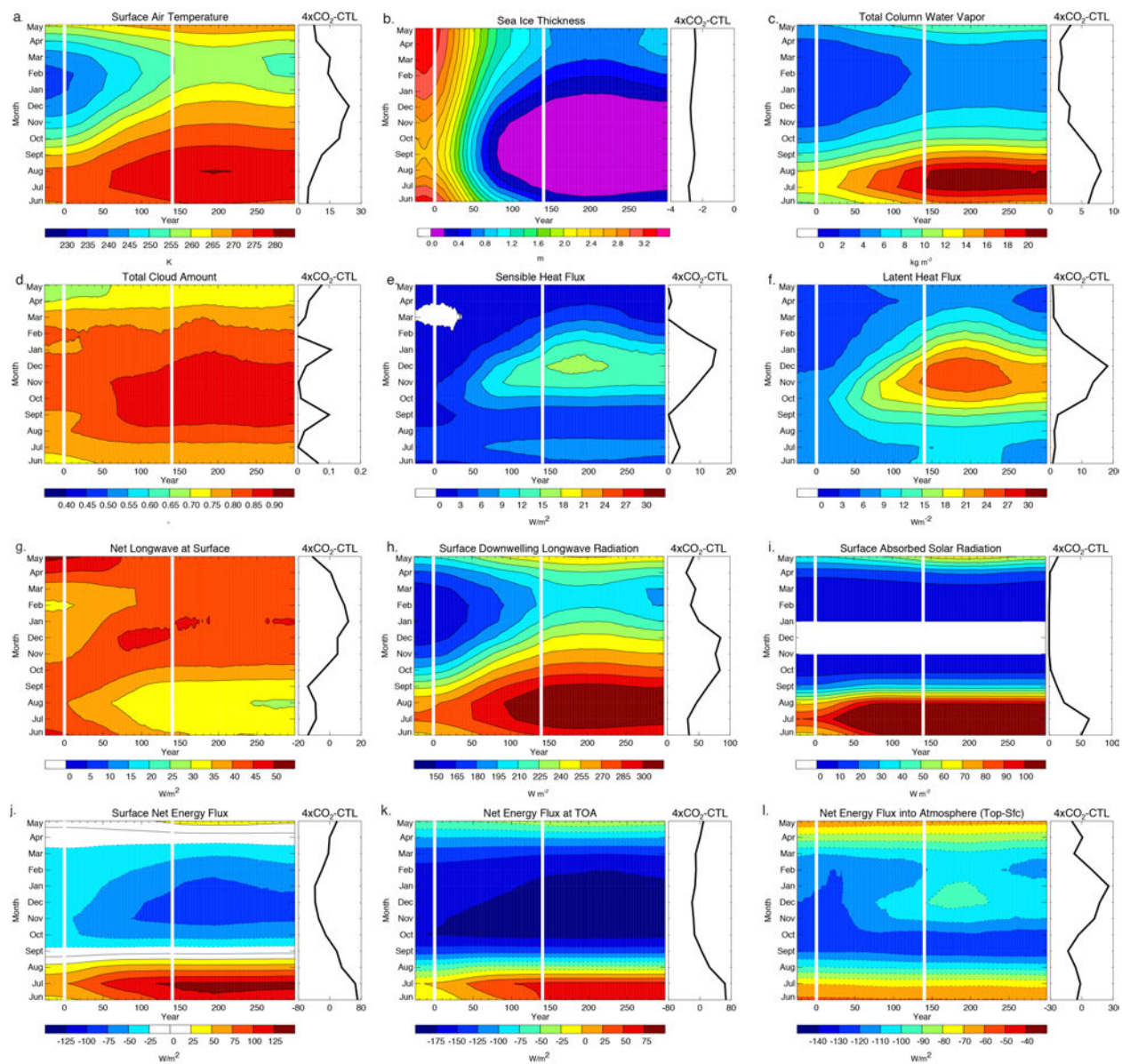


Figure 2.11. Arctic-mean seasonal trends based on calculations with CESM. The quantities shown are averaged from 70°N to the pole. The horizontal axis in each panel is time in years, and the vertical axis shows the season by month, starting with June at the bottom and running to May at the top. In each panel, the first white vertical line shows the end of the 25-year control and the beginning of the 1% per year CO₂ increase. The second vertical white line shows when 4xCO₂ has been reached.

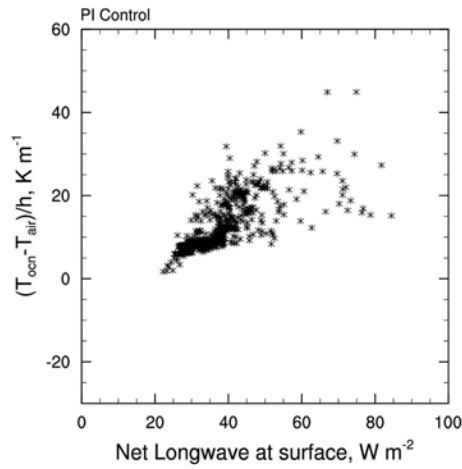
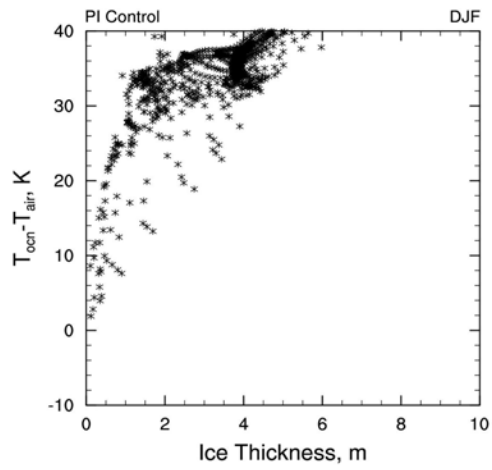


Figure 2.12. (top) Scatter plot of difference in T_{ocn} and T_{air} vs. ice thickness for CESM. (bottom) Scatter plot of difference in T_{ocn} and T_{air} divided by the ice thickness vs. net longwave.

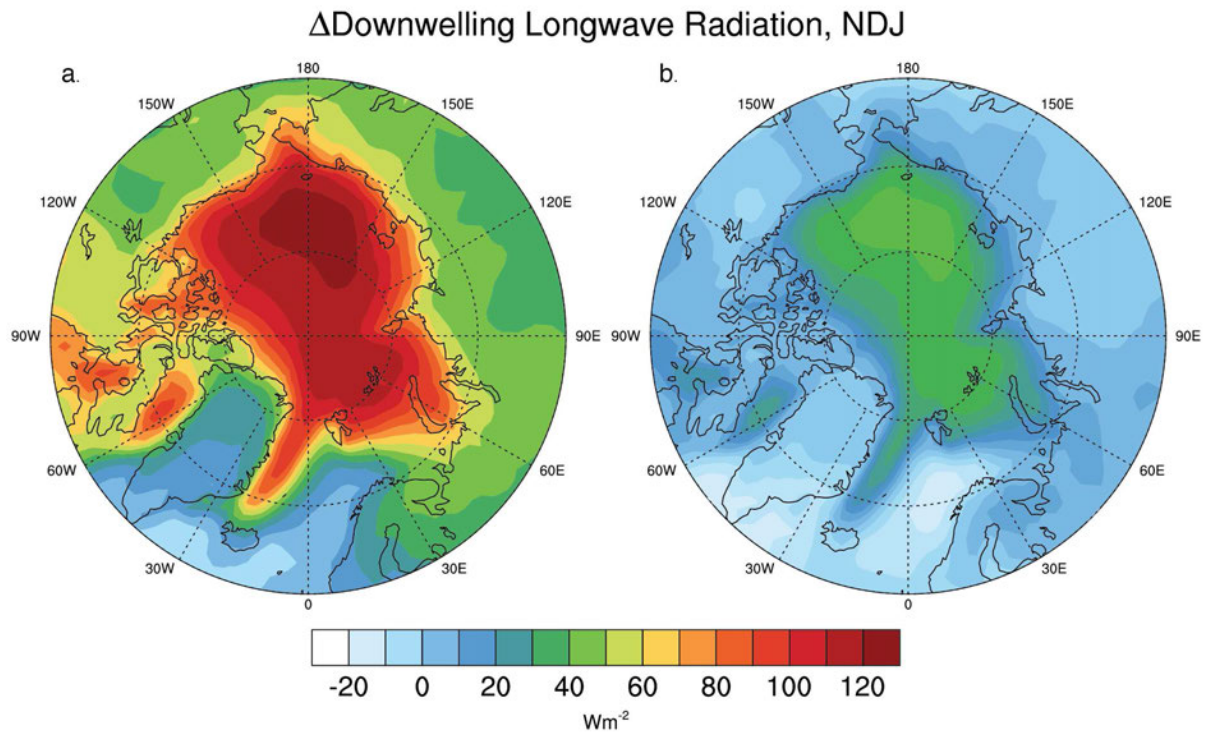


Figure 2.13. Polar stereographic map of change ($4\times CO_2$ minus PI Control) in CESM wintertime a) downwelling longwave radiation ($W m^{-2}$) and b) the contribution to a) from clouds.

CESM Δ DLR, NDJ

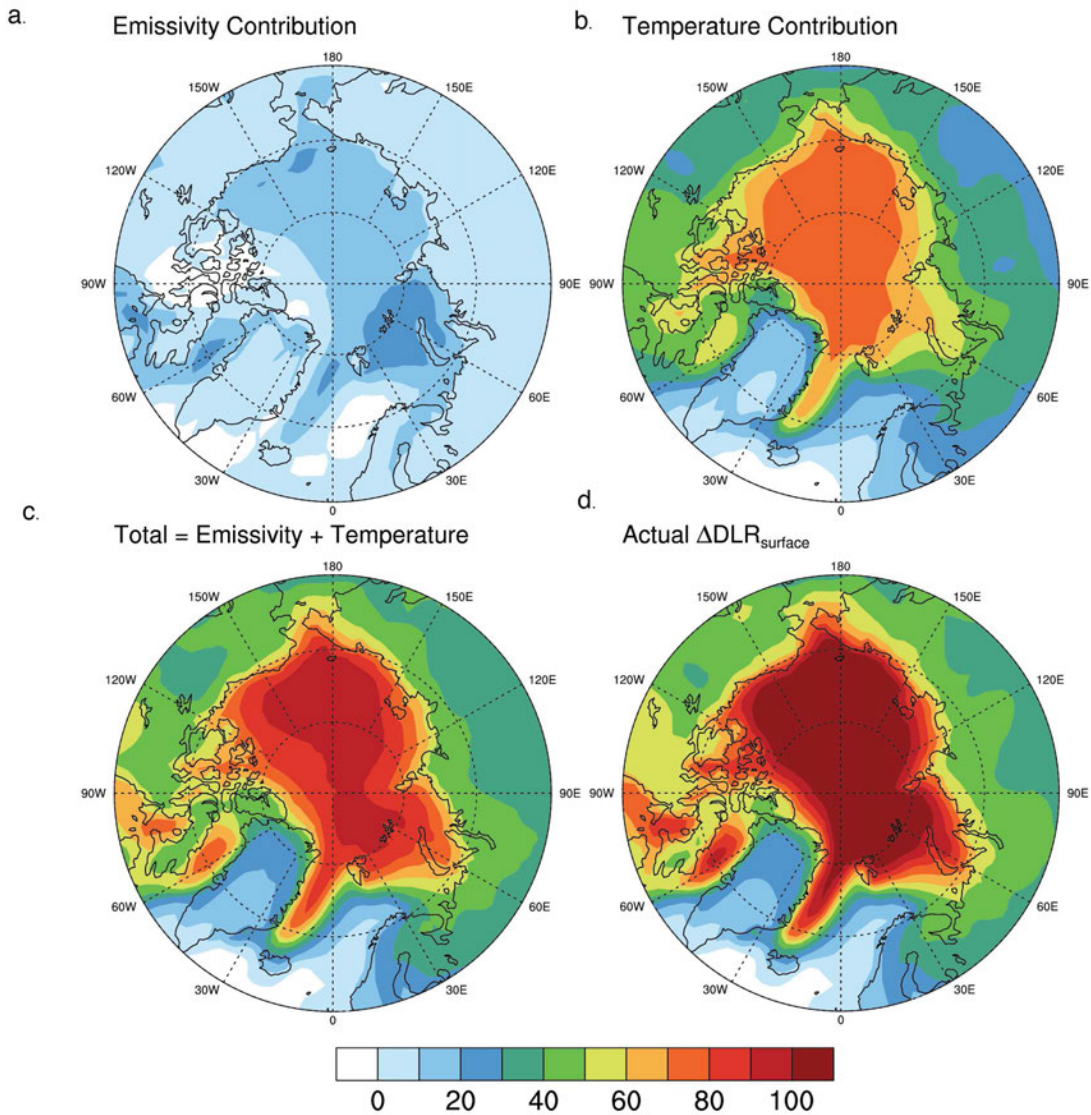


Figure 2.14. Polar stereographic maps of the wintertime contributions to $\Delta F_{\downarrow, sfc}$ (W m^{-2}) from the changes in the a) the emissivity, and b) the temperature. The calculations are based on the linearization shown in Eq. (2.2). Panel c is the sum of a) and b). Panel d is the actual change in downwelling longwave radiation. The differences between panels c and d show the errors due to the linearization.

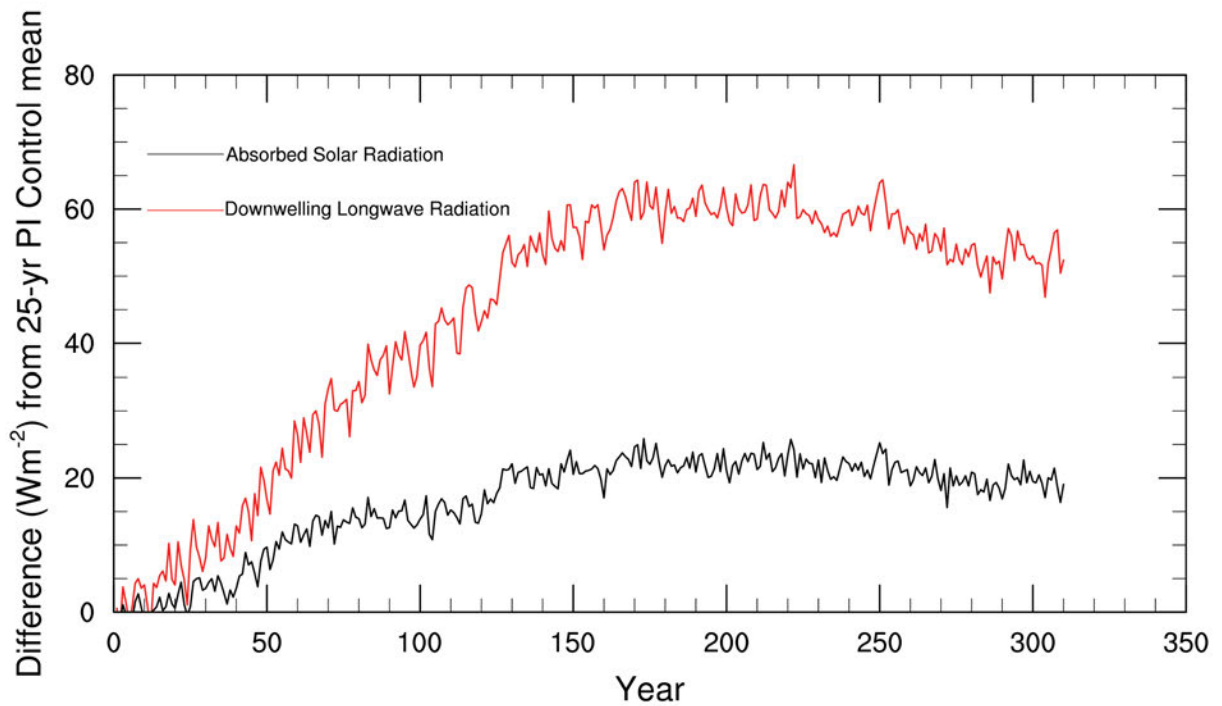


Figure 2.15. Time series of CESM-simulated annual mean change in surface downwelling longwave radiation (red) and surface absorbed solar radiation (black) relative to the mean of the 25-year control. These results are averaged over the polar cap, from 70° to 90°N.

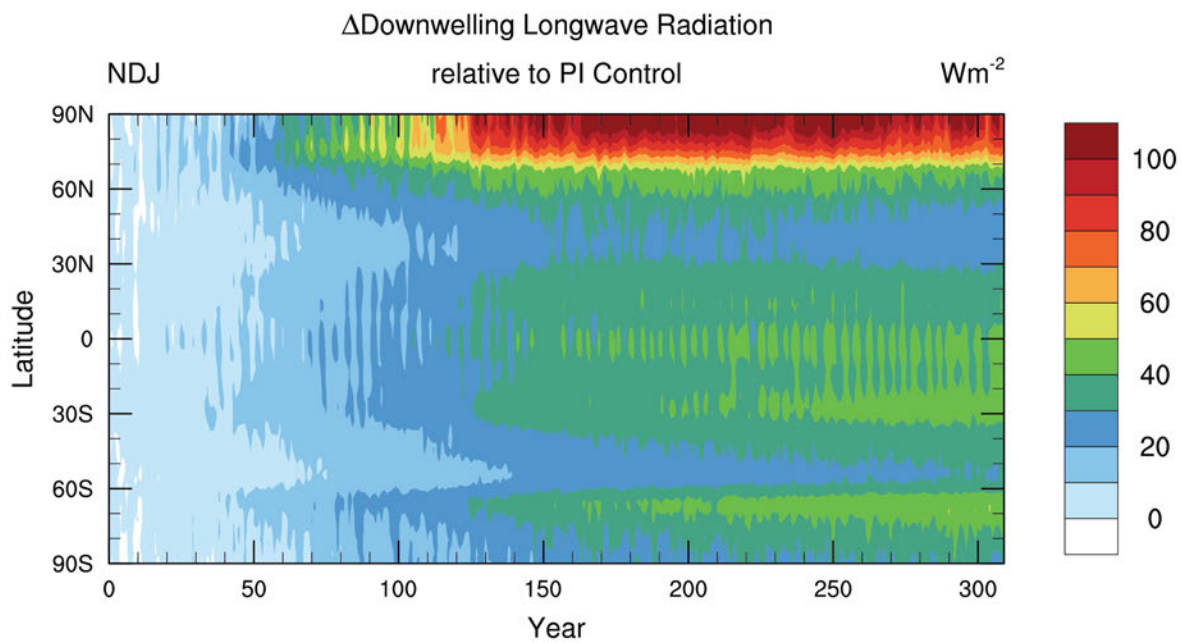


Figure 2.16. Latitude-time plot of change ($4\times\text{CO}_2$ minus PI Control) in CESM-simulated wintertime surface downwelling longwave radiation (zonally averaged) relative to the mean of the 25-year control.

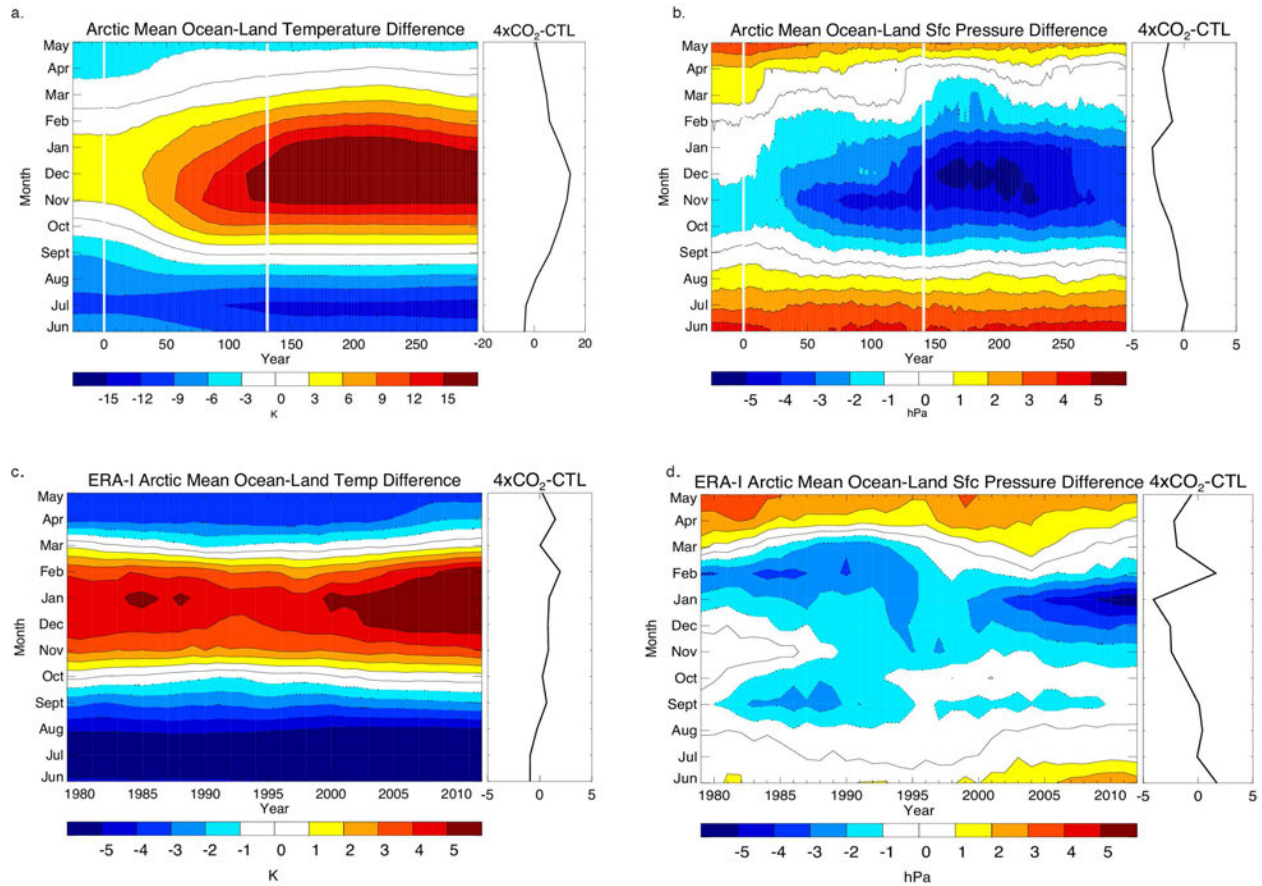
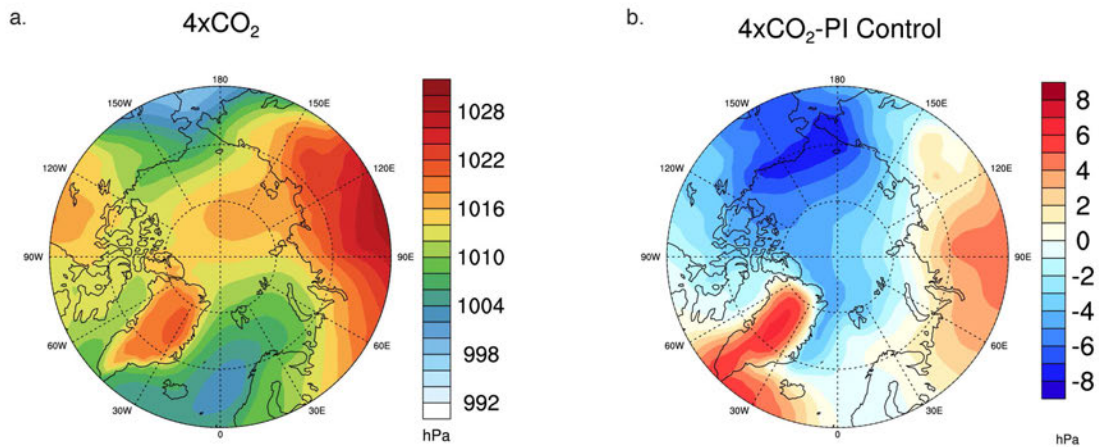


Figure 2.17. Panel a): As in Figure 2.11, but for: the CSM-simulated difference in surface air temperature between the Arctic Ocean (including areas covered by sea ice) and the surrounding land, from 60°N to the pole. Warmer colors indicate the ocean is warmer than the land and cooler colors indicate the land is warmer than the ocean. Panel b): As in panel a), but for the difference in surface pressure between the Arctic Ocean (including areas covered by sea ice) and the surrounding land, from 60°N to the pole. Panel c): The difference in surface air temperature between the Arctic Ocean (including areas covered by sea ice) and the surrounding land, from 60°N to the pole, as reported in the ERA Interim reanalysis for the years 1979 to 2012. Panel d): As in panel c), but for the difference in surface pressure between the Arctic Ocean (including areas covered by sea ice) and the surrounding land, from 60°N to the pole.

Mean Sea Level Pressure, NDJ



970 hPa Winds and Surface Temperature, NDJ

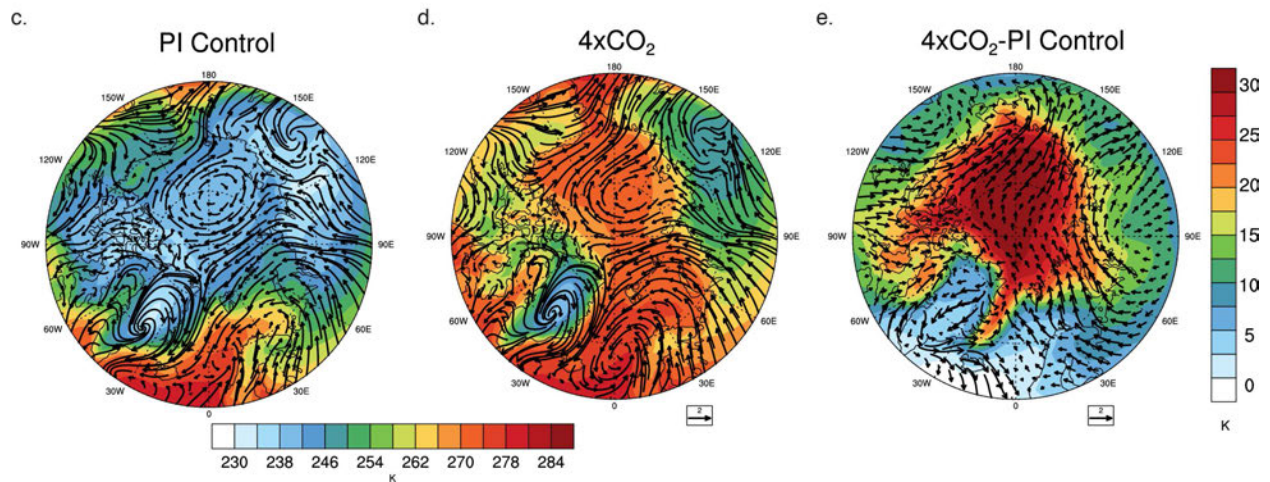


Figure 2.18. Panel a): Map showing the $4xCO_2$ CESM-simulated wintertime sea level pressure and b) difference ($4xCO_2$ minus PI control). Panels c), d) and e) respectively show maps of the CESM-simulated wintertime (November, December, and January) 970 hPa winds (vectors) with overlaid on the surface temperature (filled contours) for PI Control, $4xCO_2$, and the difference ($4xCO_2$ minus PI control).

Total Diabatic Heating, NDJ

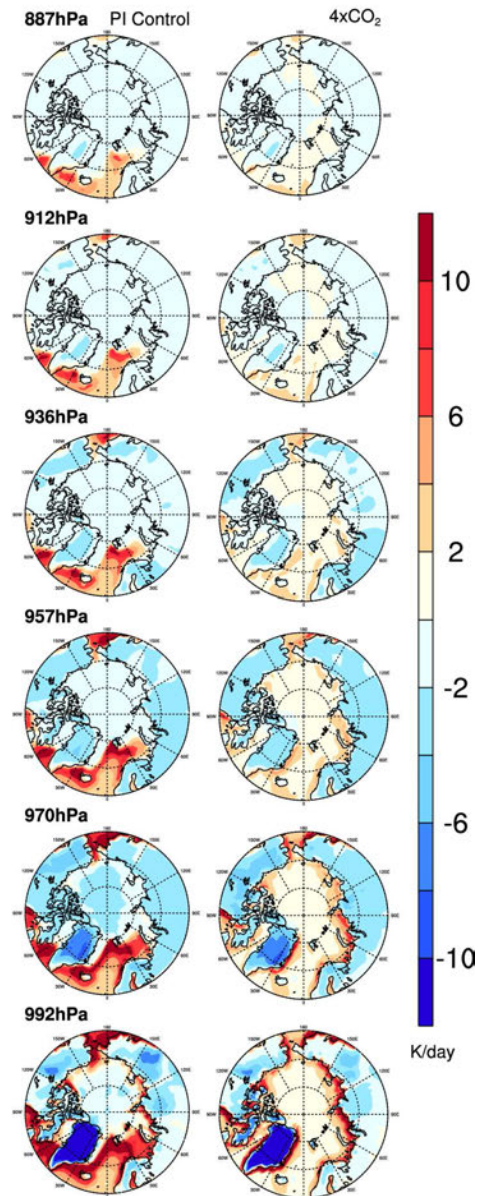


Figure 2.19. Maps of the CESM-simulated wintertime diabatic heating at several levels in the lower troposphere for both the PI control (left column) and 4xCO₂ (right column).

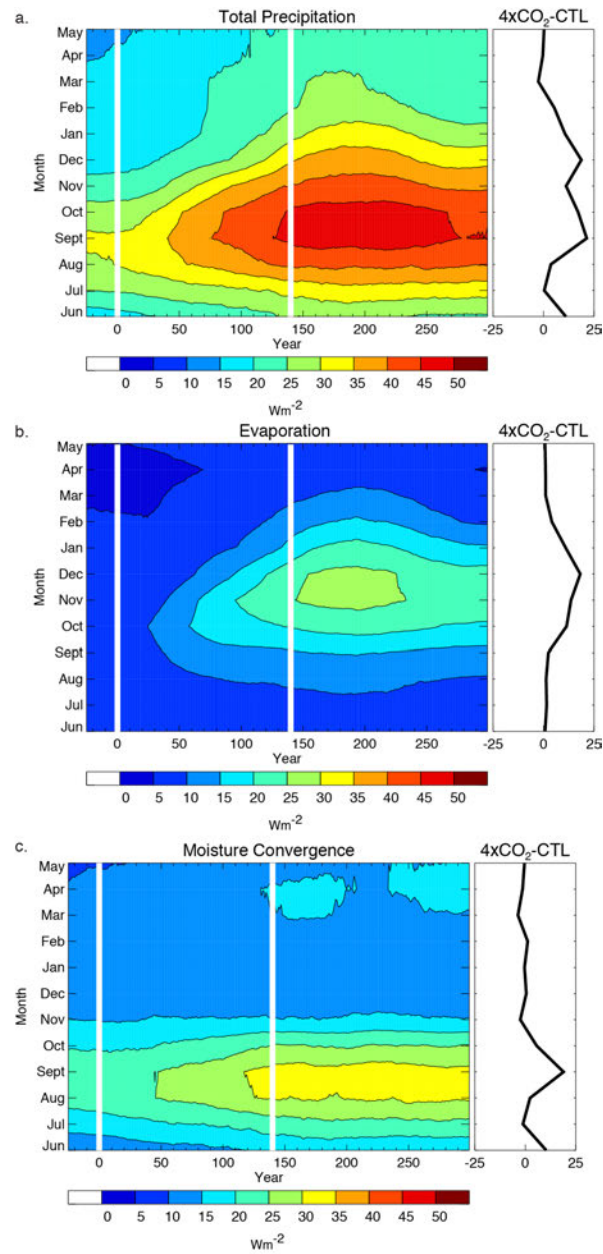
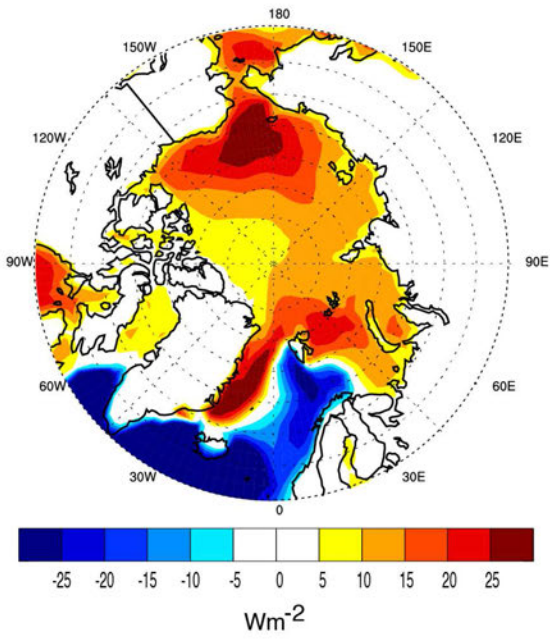


Figure 2.20. As in Figure 2.11, but for a) total precipitation, b) surface evaporation and c) moisture convergence. Units are $W m^{-2}$ for all three panels.

a.

Δ Evaporation, NDJ



b.

Δ Surface Wind Speed, NDJ

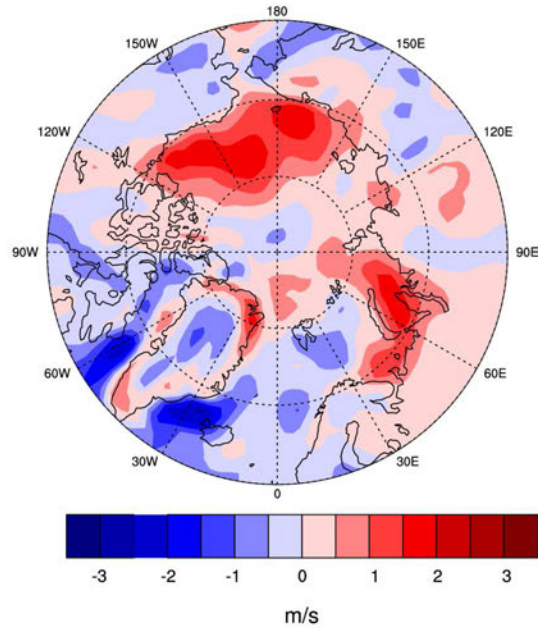


Figure 2.21. Polar stereographic map of change (4xCO₂ minus PI Control) in CESM wintertime for a) evaporation (W m⁻²) and b) surface wind speed (m s⁻¹).

TABLE 1. Selected features of the CMIP5 climate models. This information was extracted from the IPCC AR5 Appendix 9.A (Flato et al., 2013).

Model	Atmosphere resolution (lat x lon)	No. of vertical levels	Ocean resolution (lat x lon)	No. of vertical levels	Main Reference
CCSM4	0.9° x 1.25°	27	Nominal 1° (1.125° in longitude, 0.27–0.64° variable in latitude)	60	Gent et al. 2011
GFDL-ESM2M	2° x 2.5°	24	1° tripolar 360 x 200L50	50	Dunne et al. 2013
GISS-E2-R	2° x 2.5°	40	1° x 1.25°	32	Schmidt et al. 2006
HadGEM2-ES	N96 (1.25° x 1.875°)	38	1° x 1° between 30 N/S and the poles; meridional resolution increases to 1/3° at the equator	40	Collins et al. 2011
MIROC5	T85 (1.40625° x 1.40625°)	40	1.4° (zonally) x 0.5-1.4° (meridionally)	50	Watanabe et al. 2010
MPI-ESM-MR	T63 (1.8° x 1.8°)	96	TP04 (0.4° x 0.4°)	40	Stevens et al. 2012

Δ Surface Air Temperature, NDJ

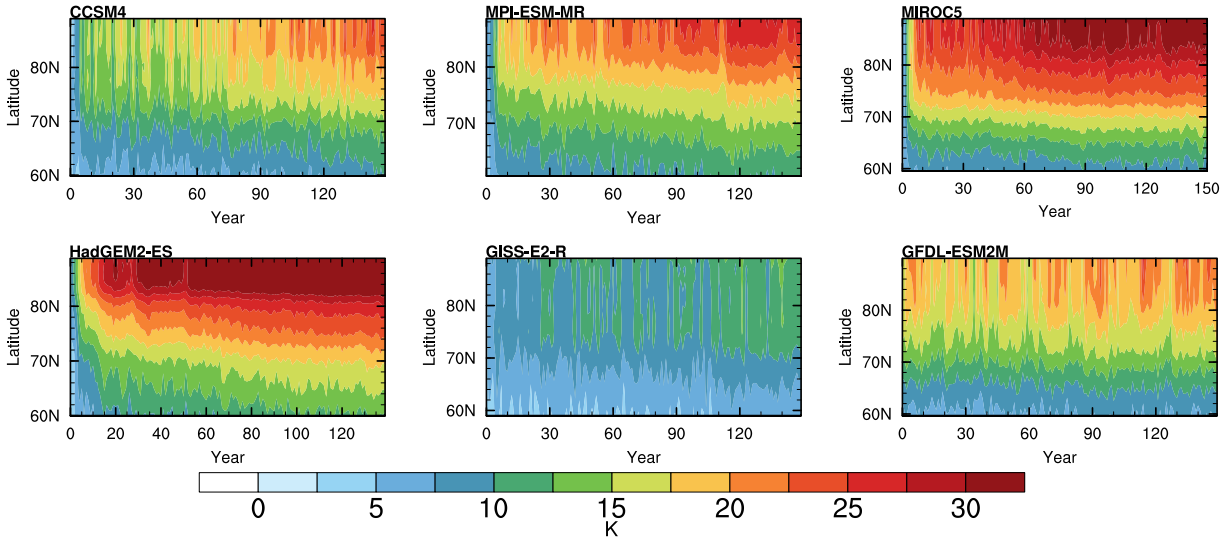


Figure 2.22. Latitude-time plot of change (abrupt 4xCO₂ minus PI Control) for wintertime surface temperature (K, zonally averaged) relative to the mean of the 25-year control for the CMIP5 models.

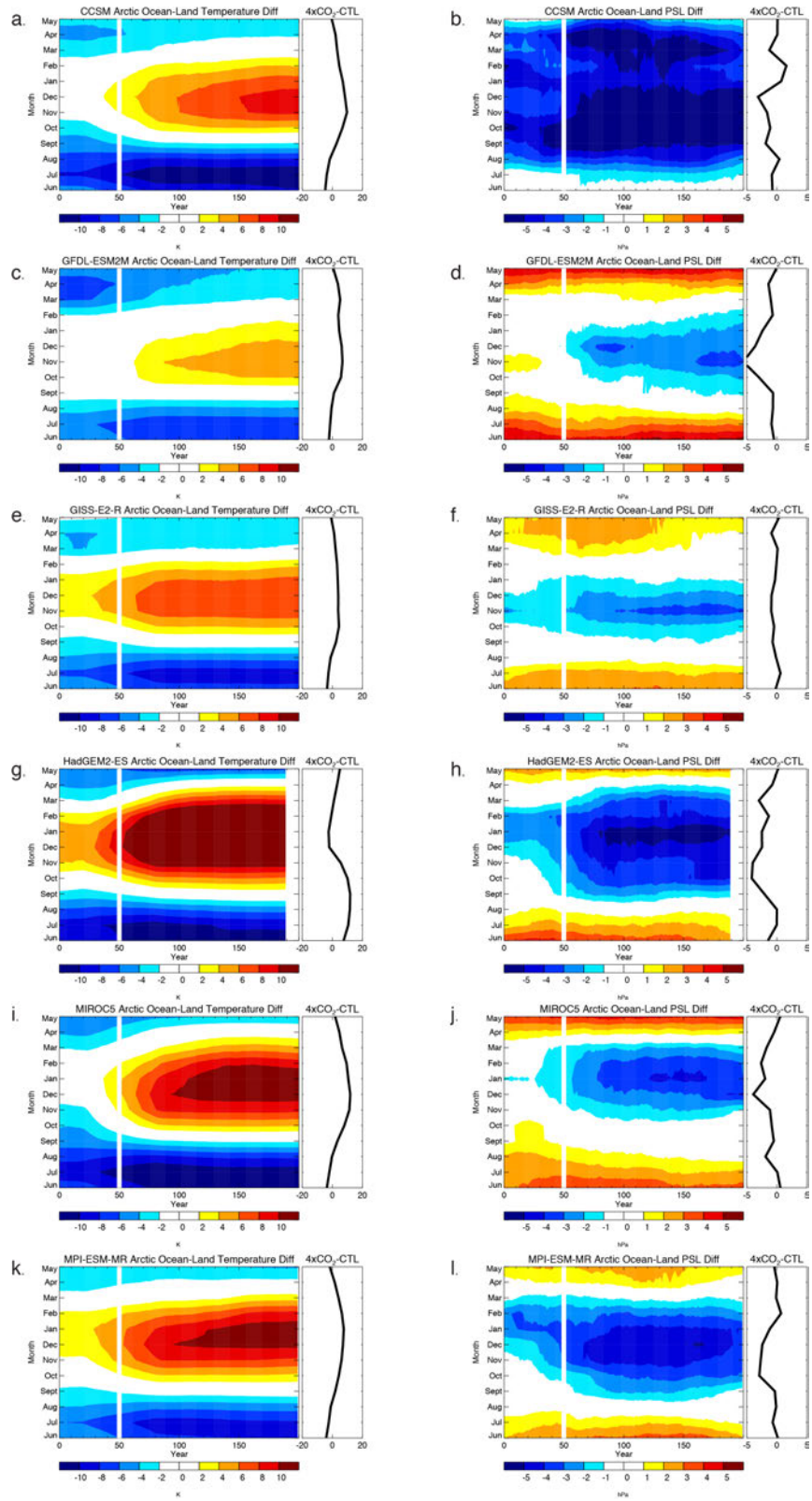


Figure 2.23. As in Figure 2.17a and 2.17b, but for the CMIP5 models.

Δ Mean Sea Level Pressure, NDJ

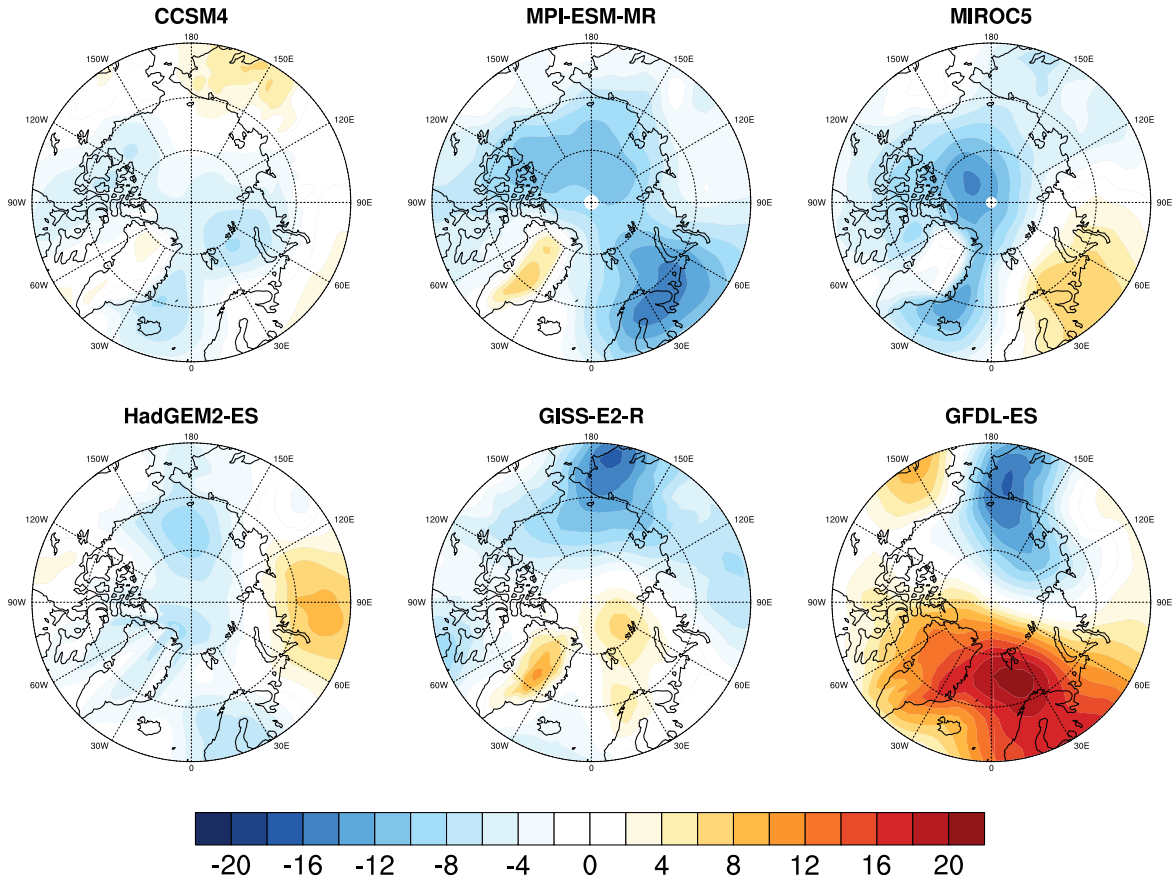


Figure 2.24. Maps of the change ($4\times\text{CO}_2$ minus PI Control) in wintertime mean sea level pressure (hPa) for the CMIP5 models.

925 hPa winds and Surface Air Temperature, NDJ

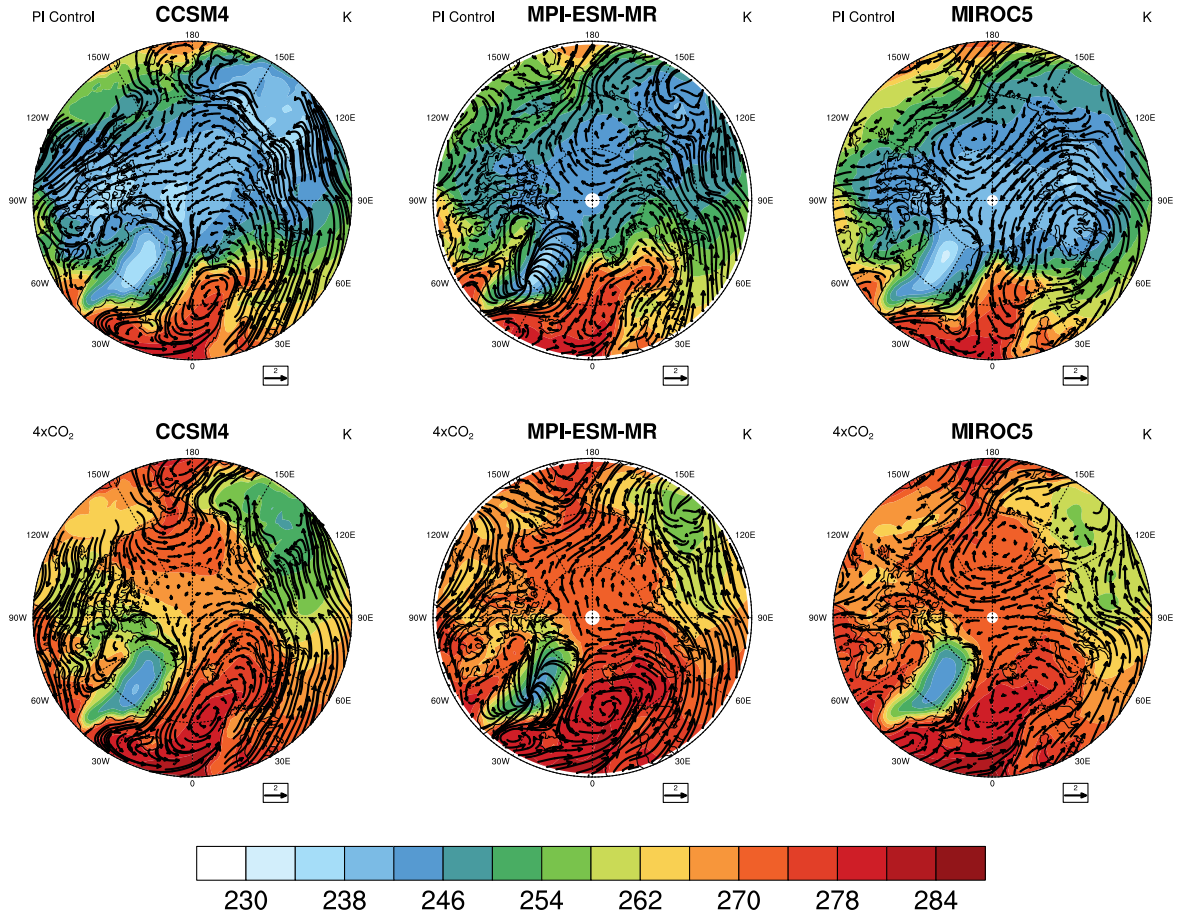


Figure 2.25a. Maps of the CMIP5 models simulated wintertime 925hPa winds (vectors, m s⁻¹) overlaid on the surface temperature (filled contours, K) for PI Control (top) and 4xCO₂ (bottom).

925 hPa winds and Surface Air Temperature, NDJ

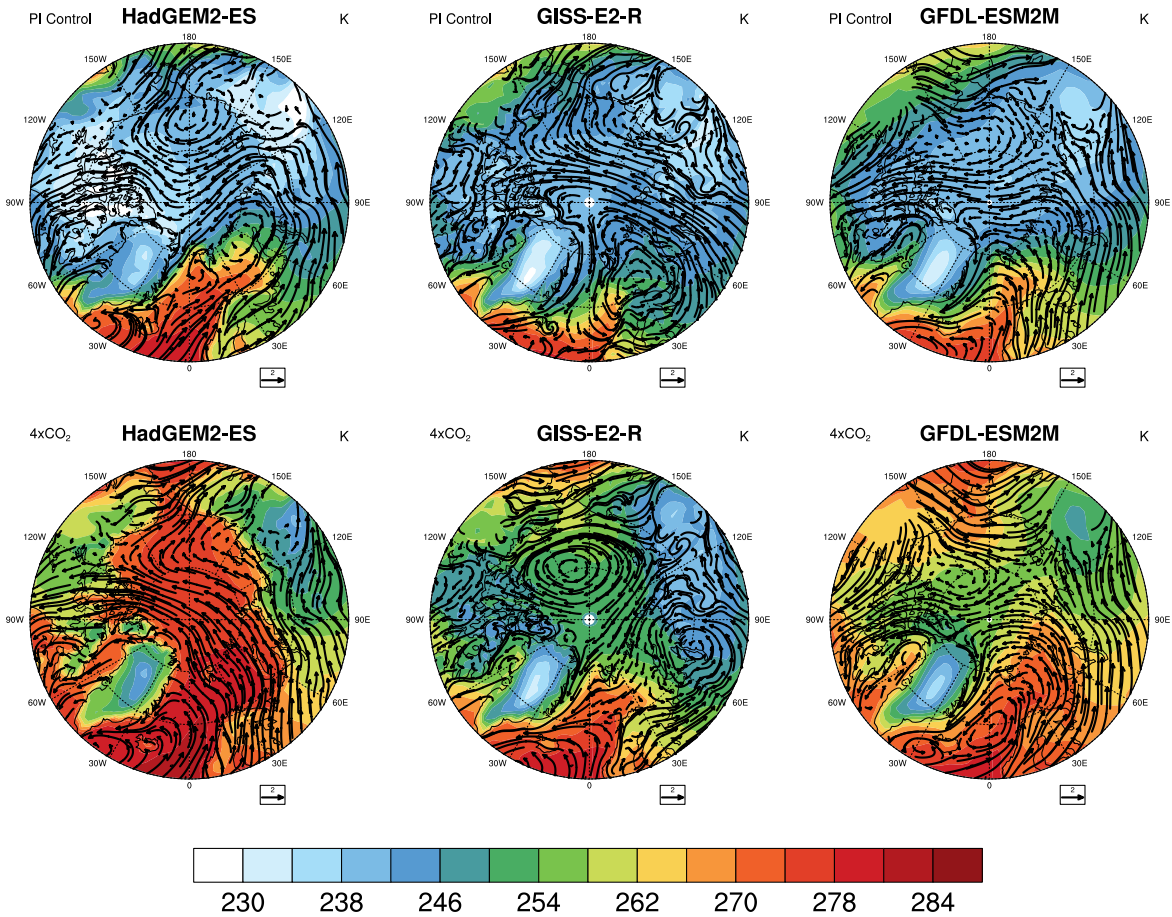


Figure 2.25b. Maps of the CMIP5 models simulated wintertime 925hPa winds (vectors, m s^{-1}) overlaid on the surface temperature (filled contours, K) for PI Control (top) and 4xCO₂ (bottom).

$\Delta 925$ hPa winds and Surface Air Temperature, NDJ

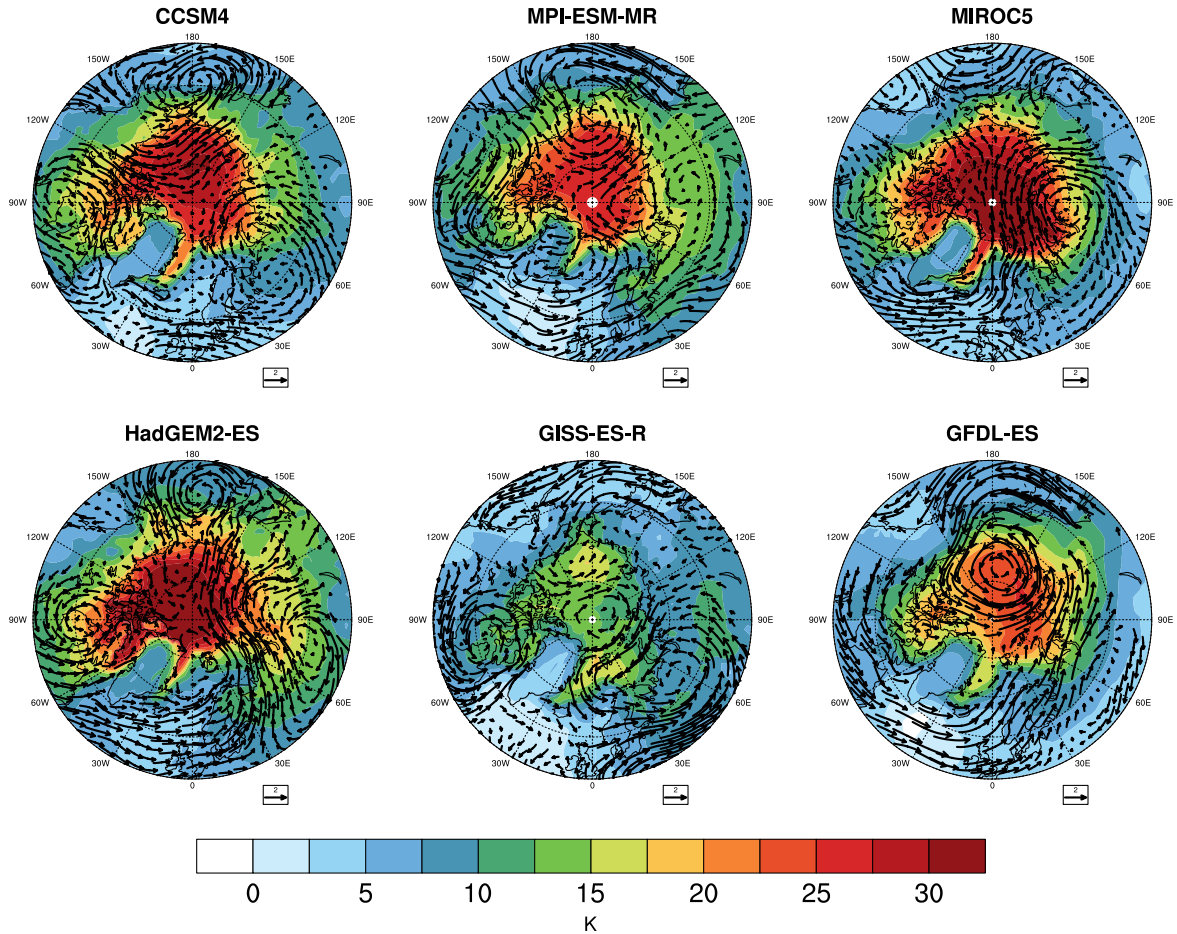


Figure 2.26. Maps of the CMIP5 models simulated wintertime 925hPa winds (vectors, m s^{-1}) overlaid on the surface temperature (filled contours, K) for the difference 4xCO₂ minus PI Control.

Δ Downwelling Infrared Radiation, NDJ

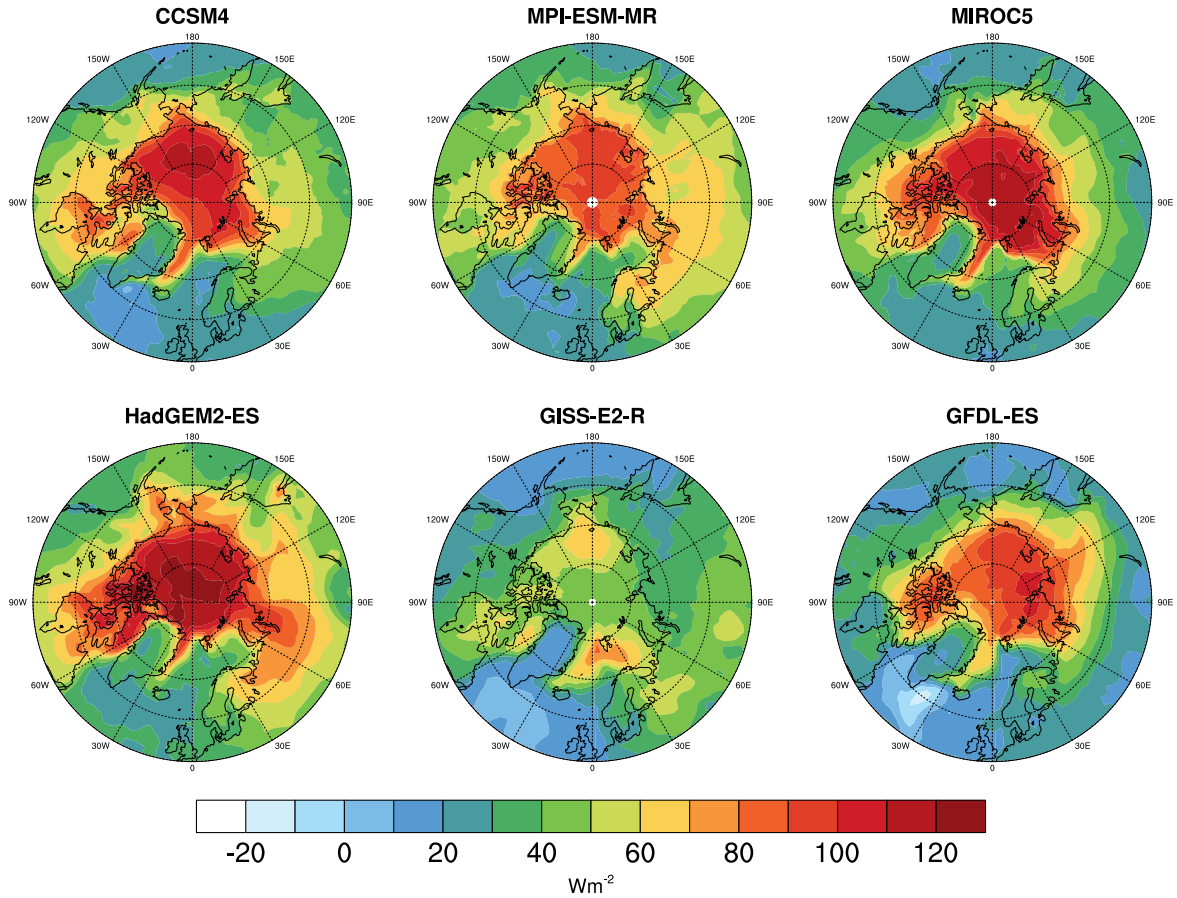


Figure 2.27a. Maps of the change ($4\times\text{CO}_2$ minus PI control) in CMIP5 wintertime downwelling longwave radiation (W m^{-2}).

Cloud Contribution to Δ Downwelling Infrared Radiation, NDJ

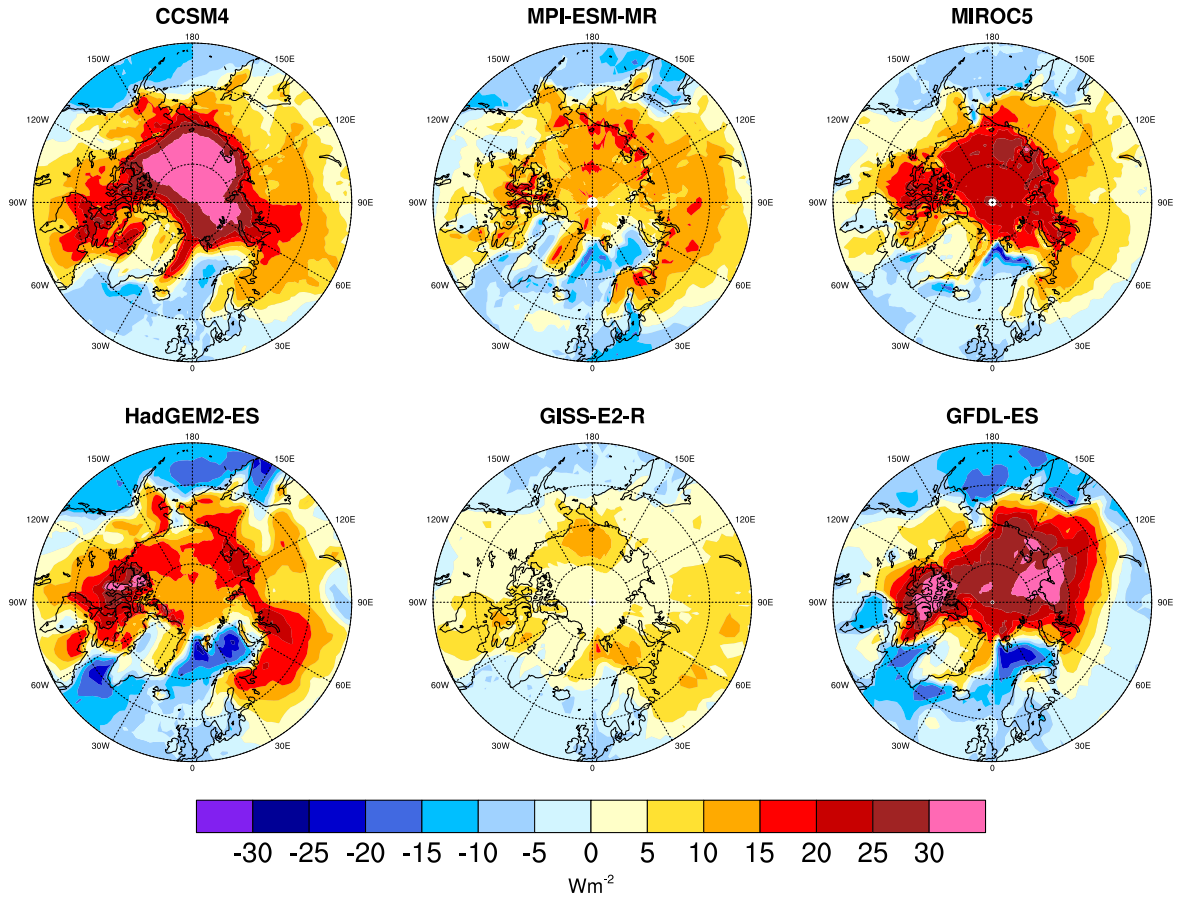


Figure 2.27b. Maps of the cloud contribution to the change ($4xCO_2$ minus PI control) in CMIP5 wintertime downwelling longwave radiation ($W m^{-2}$).

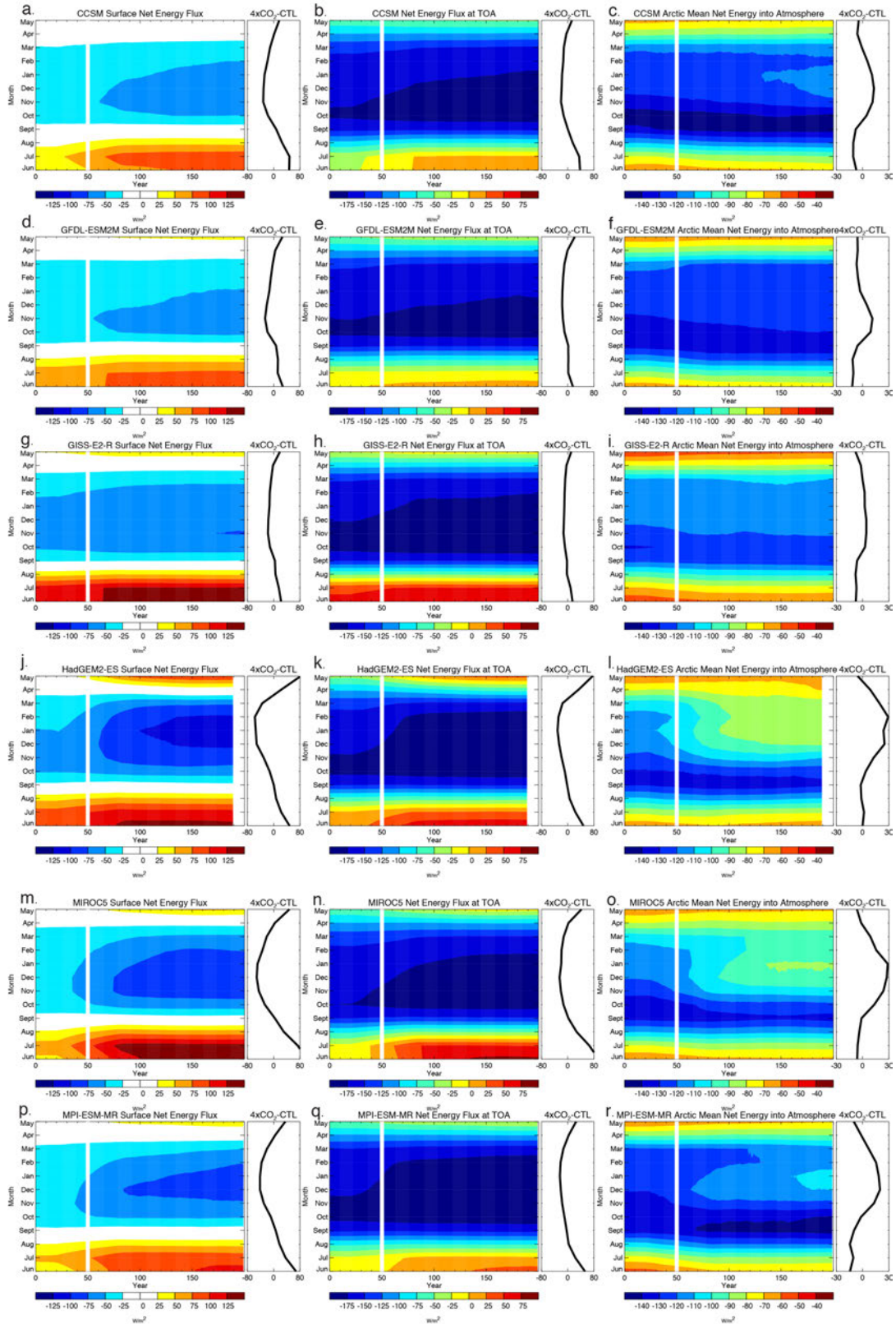


Figure 2.28. As in Figure 2.11j-l, but for the CMIP5 models.

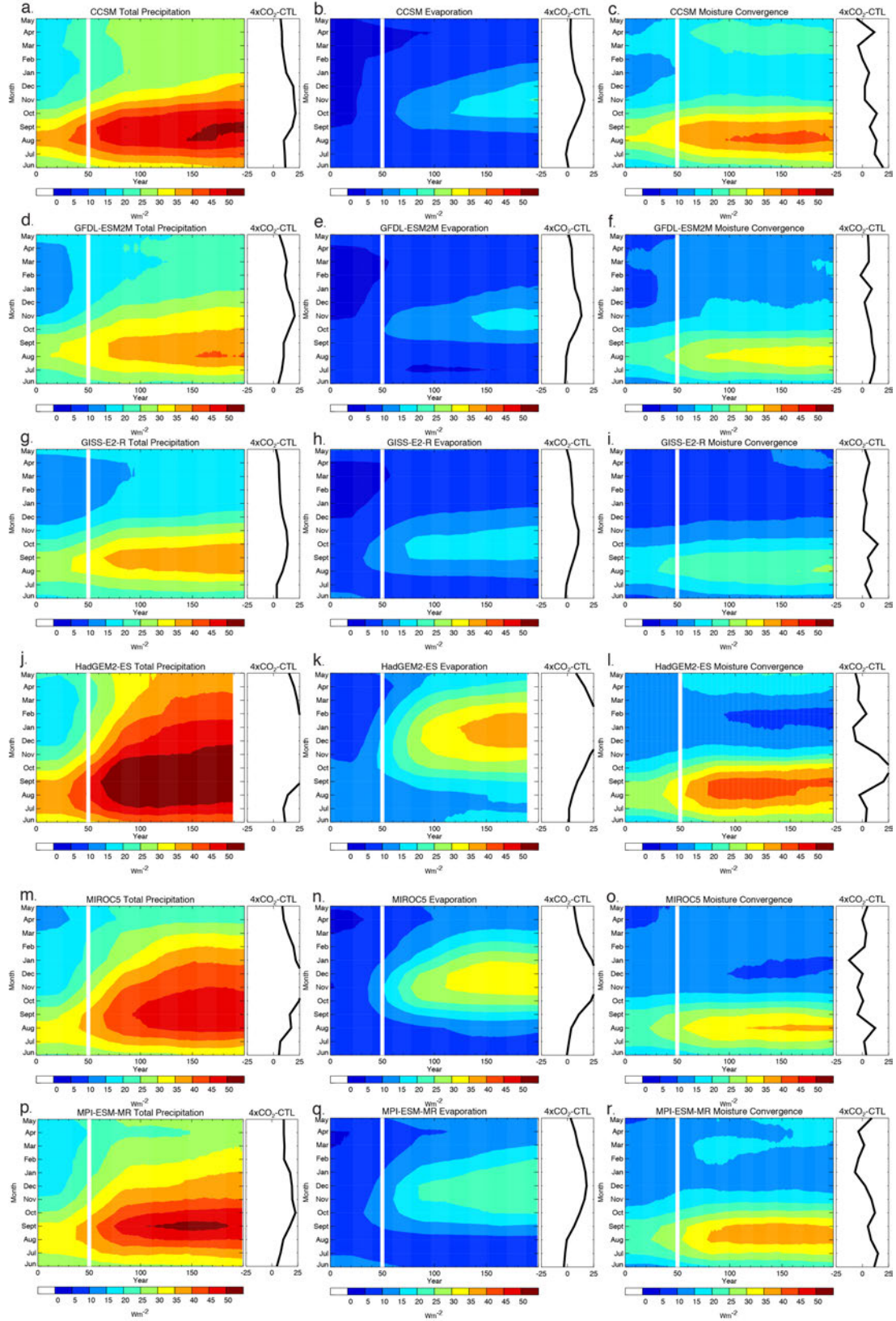


Figure 2.29. As in Figure 2.21, but for the CMIP5 models.

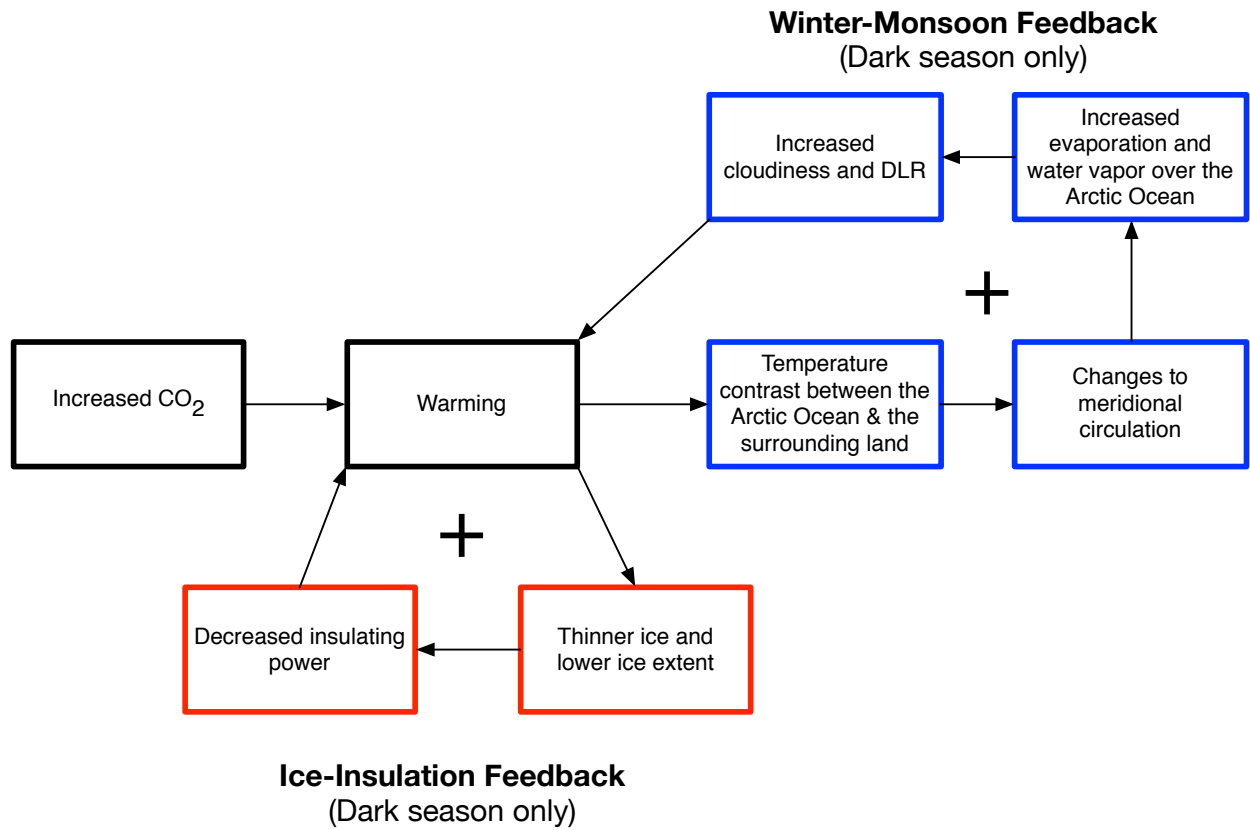


Figure 2.30. Schematic of the ice-insulation and winter-monsoon feedbacks.

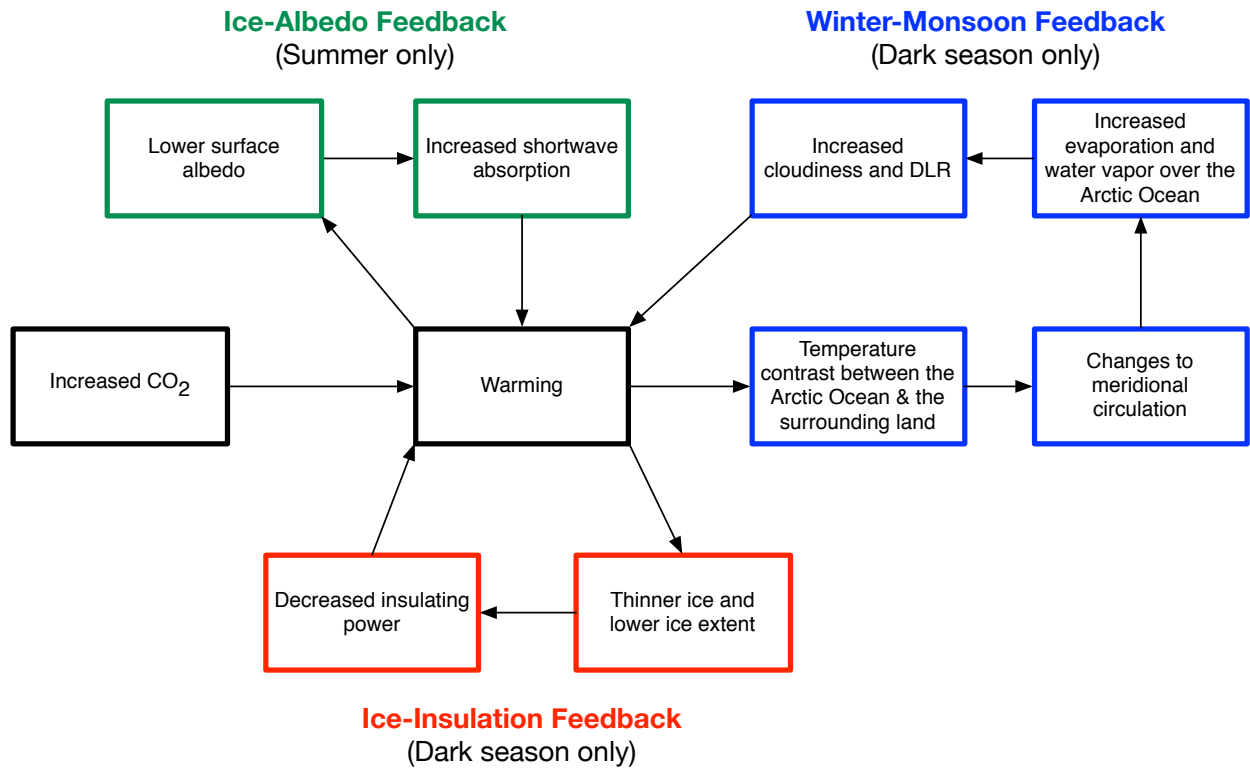


Figure 2.31. Schematic of the three feedbacks that contribute to Arctic warming.

CHAPTER 3: THE CLIMATE OF THE SUPER-PARAMETERIZED CESM

This chapter explores the climate of the super-parameterized Community Earth System Model (SP-CESM), described below, and how it compares to the conventional CESM. We first examine the global climate change simulated with SP-CESM and then compare the 4xCO₂ climate of SP-CESM with the conventional CESM. As described below, simulations with super-parameterization have improved many aspects of the simulated global climate and we explore this briefly by discussing selected features of the Arctic atmosphere. We then evaluate the distribution of clouds, radiation, and Arctic weather states in the simulated climate, compared to observations. The chapter ends with a discussion of the influence of super-parameterization on the feedbacks associated with Dark Warming.

The super-parameterized Community Earth System Model (SP-CESM) is a fully coupled global circulation model (a modified version of CESM), in which the conventional physical parameterizations have been replaced by embedding a two-dimensional (2D) cloud resolving model (CRM) into each atmospheric grid column. In the simulation discussed here, the CRMs have 32 columns oriented in the north-south direction, a horizontal grid spacing of 4 km, and 28 levels that are collocated with the lowest levels of the large-scale model. The CLM, CICE, and POP2 are the same as those used in CESM (see discussion in Chapter 2). Figure 3.1 illustrates how the GCM works with and without super-parameterization. In the conventional GCM, the model is forced by large-scale advection and the smaller-scale processes are parameterized (i.e. convection, microphysics, radiation, and turbulence). With super-parameterization, cloud microphysics and radiation are still parameterized, but are computed on the finer CRM grid. The

momentum transport associated with the 2D CRM is unrealistic, so momentum feedback from the CRM to the large scale is not included (Khairoutdinov et al., 2005). The CRMs are forced by the large-scale advection of heat, moisture, and momentum. The GCM, in turn, feels the domain-averaged CRM tendencies of temperature, water vapor, and non-precipitating liquid water. The CRMs embedded within each grid-column have periodic lateral boundary conditions. More detailed information about the embedded CRM and coupling between the GCM and the CRM is discussed in Khairoutdinov and Randall (2001, 2003) and Khairoutdinov et al., (2005).

As with conventional parameterizations, the CRM is assumed to be representative of the cloud processes that occur in the entire grid column, rather than representing an exact representation of specific clouds. The embedded CRM and the conventional cloud parameterizations play the same role, to namely estimate the characteristics that clouds would have based on the large-scale conditions in the grid-box. The main difference between the convective parameterization and the CRM is that the CRM can explicitly represent some of the sub-grid dynamical processes, as well as fractional cloudiness.

In this study, SP-CESM was configured similarly to CESM, with a GCM horizontal resolution of 1.9° latitude by 2.5° longitude and 30 levels. The SP-CESM PI control simulation was branched from the CESM control simulation and was run with constant pre-industrial greenhouse gas concentrations and external forcings for ten years. The SP-CESM $4\times\text{CO}_2$ simulation was a branch from the 1% per year run described in Chapter 2, after the CO_2 concentration was held fixed for 170 simulated years. The SP-CESM $4\times\text{CO}_2$ was run for an additional ten years.

Super-parameterization has been shown to improve the simulation of many aspects of the global climate, including the Madden–Julian oscillation (MJO; Benedict and Randall 2009, 2011; Thayer-Calder and Randall, 2009), the Asian monsoon (DeMott et al., 2011, 2013), El Niño– Southern Oscillation (Stan et al., 2010), precipitation intensity (DeMott et al., 2007), the diurnal cycle of rainfall over continents and oceans (Khairoutdinov et al., 2005), the diurnal propagation of convection in the lee of the Rocky Mountains (Pritchard et al., 2011), the West African Monsoon (McCrary et al., 2014a), African Easterly waves (McCrary et. al., 2014b), and daily rainfall intensity in the Inter-Tropical Convergence Zone (Kooperman et al., 2016). These studies demonstrate that simulations with super-parameterization are more realistic than conventional models because of the super-parameterization’s ability to represent the vertical structure of diabatic heating and moistening in a wide range of environments.

Studies with super-parameterization have mostly focused on the tropics. One exception is the study of Arnold et al., (2014), who proposed a positive wintertime feedback between convective clouds and Arctic sea ice loss. They found that super-parameterization produces greater Arctic cloud cover and reduced sea ice extent at high CO₂, relative to the conventional model. In their study, given the strong feedbacks due to sea ice melting, they tested the robustness of the stronger sea ice response in SP-CESM, to ensure that it was not merely an amplification of a random perturbation (Arnold et al., 2014). The authors initialized CESM with the final state of SP-CESM at 4xCO₂ and found that the model quickly went back to its CESM state, including a larger sea ice cover. This suggests the robustness of behavior of SP-CESM.

This chapter has five primary objectives:

1. Explore the representation of the Arctic atmosphere in SP-CESM by diagnosing key features of the Arctic climate.
2. Examine the distribution of Arctic clouds and evaluate how CESM and SP-CESM simulate these unique and complex clouds.
3. Quantify the Arctic top-of-the-atmosphere (TOA) and surface net radiation biases and determine how clouds influence these biases.
4. Examine the distribution of Arctic weather states in the present-day climate and determine the role of cloud properties.
5. Examine the global and Arctic climate change simulated by SP-CESM as it compares to results from the conventional CESM.

3.1. SIMULATION OF THE PRESENT-DAY ARCTIC ATMOSPHERE

To explore the representation of the Arctic atmosphere in SP-CESM, we evaluate a few key features of the Arctic climate. These atmospheric characteristics are chosen because of their significance for regional and global climate. We evaluate model results using reanalysis products together with satellite and ground-based observations.

Surface temperature

Comparisons of seasonal mean surface air temperature are presented in Figure 3.2 for ERA-Interim (top row), CESM minus observations (middle row), and SP-CESM minus observations (bottom row). Both models generally simulate Arctic surface temperatures reasonably well across all seasons. With a few exceptions, biases are negative and generally

small (2-4 K) and within a few degrees of observations. Some of these apparent negative biases during winter are likely the result of the positive warm bias in ERA-Interim Arctic temperatures as discussed in Simmons and Poli (2015). The cold bias is present year-round, but the magnitude is significantly decreased during the rest of the year. For CESM, the most notable differences include a cold bias of up to 18 K along eastern Greenland and the Barents Sea during winter. This bias is also present in SP-CESM but is much weaker. Much of the Arctic Ocean is too cold during winter, spring, and fall, especially in CESM with cold biases up to 10 K. In SP-CESM, the Arctic Ocean cold bias is only 2-4 K. Summer surface temperatures are simulated reasonably well with a small warm bias up to 4 K over Scandinavia, southern Greenland and Siberia in both models.

Sea level pressure

Accurate simulation of sea level pressure (SLP) is important because of its influence on surface wind speed and direction, temperature, and precipitation. Wind speed and direction are particularly important in the Arctic as the wind drives the advection of sea ice (DeWeaver and Bitz 2006) and influences the heat exchanges between the ocean, land, and atmosphere. Figures 3.3a and 3.3b illustrate the simulated winter (DJF, December-January-February) and spring (MAM, March-April-May) mean sea level pressure compared to ERA-Interim observations. Main features of the DJF mean SLP field are the Aleutian Low, Siberian High, and Icelandic Low as pointed out in Fig 3.3a. Both models capture the Aleutian Low reasonably well. Both models also capture the Siberian High, but it is elongated and more pronounced in CESM with a bias up to 12 hPa. SP-CESM underestimates the Icelandic Low by 2-4 hPa. During spring (MAM), the Beaufort High is the main driver of sea ice advection throughout the Arctic Ocean. SP-CESM simulates the Beaufort High quite well, while CESM overpredicts it by 2-6 hPa. Most strikingly,

the mean SLP is generally too high in CESM, especially over the eastern Arctic Ocean during spring.

Sea ice area and thickness

To assess the simulated sea ice area, we use the sea ice concentration dataset from Comiso (2008), which is derived using the Advanced Microwave Scanning Radiometer for Earth Observing System (EOS) (AMSR-E) bootstrap algorithm applied to the brightness temperature data from the Scanning Multichannel Microwave Radiometer (SMMR) on the Nimbus-7 satellite and from three Special Sensor Microwave Imager (SSM/I) sensors on the Defense Meteorological Satellite Program's (DMSP's) F8, F11, and F13 satellites. Figure 3.4 illustrates the spatial distribution of sea ice area for March and September compared to observations. The model biases are shown in the bottom panel. We find that the simulated spatial sea ice concentration pattern is in close agreement with the satellite data, with a few exceptions. During March, the period when sea ice reaches its maximum in the Northern Hemisphere, the sea ice is too extensive in the Barents Sea (North of Norway), off the eastern coast of Greenland, and the Bering Sea in both models. The sea ice minimum typically occurs in September and the distribution is simulated reasonably well. SP-CESM better simulates the sea ice edge in the central Arctic Ocean, although both models have too much ice along the northern Eurasian coast.

Large-scale gridded sea-ice thickness data for the Arctic have only recently started to become available and are based on satellite altimeter measurements (e.g., Laxon et al., 2003; Kwok et al., 2004). Here we combine the gridded sea-ice data from Kwok et al., (2008), which are derived from Ice, Cloud, and Land Elevation Satellite (ICESat) measurements and the Pan-Arctic Ice-Ocean Modelling and Assimilation System (PIOMAS). PIOMAS is a coupled ocean

and sea ice model that, unlike other numerical models, assimilates sea ice data by including measurements of near-real-time sea ice (Zhang and Rothrock (2003)). Figure 3.5 illustrates the large-scale pattern of the sea ice thickness for the observations and models for March, September, and the model biases (bottom panels). The distribution of sea ice thickness for SP-CESM is strikingly similar to the observations, with a few exceptions. The largest biases in SP-CESM are found around the sea ice edge in the Siberian Sea, where the ice is too thin (~ 1 m) and the very thick ice off the coast of Greenland during March. September ice thickness is simulated reasonably well, although the same biases from March appear again during this season. On the other hand, CESM has ice that is too thick (bias of 2 m) over much of the central Arctic Ocean during March and September compared to observations.

From this brief evaluation of a few key atmospheric variables, SP-CESM tends to provide a more consistent representation of present-day Arctic climate. The biases shown indicate the shortcomings of the model and highlight there is room for improvement.

3.2 ARCTIC CLOUDS AND RADIATION

Clouds remain among the largest sources of uncertainty in climate simulation (Solomon et al., 2007). In particular, high-latitude clouds (e.g., mixed-phase and ice clouds) have proven challenging for models to simulate correctly (e.g., Klein et al., 2009; Kay et al., 2011), in part due to how different Arctic atmospheric conditions can be from the rest of the world. High latitude clouds are important because of their ability to influence changes in Arctic Ocean mixed layer temperature and sea ice melting rates (e.g., Eisenman et al., 2007; Gorodetskaya et al., 2008) and precipitation, both of which regulate surface albedo.

Arctic field programs like the Surface Heat Budget of the Arctic (SHEBA) experiment in the late 1990s and the Mixed-Phase Arctic Cloud Experiment (M-PACE) in the early 2000s have observed and shown that the Arctic is a very a complex environment and an all around cloudy place. Cloud cover is on the order of 60-90% seasonally, with late summer and early fall being the cloudiest seasons and winter having the least percentage of total cloudiness (Intrieri et al., 2002). As is well known, clouds strongly influence the top-of-the-atmosphere radiation by reflecting incoming solar radiation and reducing the emission of infrared radiation to space. The presence or absence of clouds has a large impact on the surface radiation budget through two competing factors: (1) cooling the surface by shading downwelling shortwave (SW) radiation and (2) warming the surface through the emission of longwave (LW) radiation. Since clouds are a key part of the surface radiation budget of the Arctic, it is ever more so important to understand how they interact with the surface and how certain properties are more or less important, especially as the climate continues to change.

We utilize the Cloud–Aerosol Lidar and Infrared Pathfinder Satellite Observations GCM-Oriented *CALIPSO* Cloud Product (CALIPSO-GOCCP) lidar observations (Chepfer et al., 2010) to assess cloud amount and spatial distribution of Arctic clouds. CALIPSO-GOCCP is well suited for Arctic assessments and has been utilized in other model-to-observation comparisons (Kay et al., 2012; Barton et al., 2012; English et al., 2014) as it detects up to 82° N. CALIPSO-GOCCP cloud detection is unaffected by the surface conditions or thermal structure of the atmosphere and is therefore more reliable than passive remote sensing in the Arctic. CALIPSO-GOCCP has 330 m horizontal resolution and 30 m vertical resolution from the surface to 8 km

altitude, and 1 km horizontal resolution and 60 m vertical resolution above 8 km. CALIPSO-GOCCP is able to detect near-surface clouds as well as optically thin clouds, which are both common in polar regions. We average CALIPSO-GOCCP monthly observations from 2007 to 2013 and compare to CESM and SP-CESM model output. We use this satellite dataset to evaluate our model results bearing in mind that there are uncertainties in the retrieval algorithms as well as the model.

The CERES-EBAF (Energy Balanced and Filled) dataset is used for climate model evaluation, estimating the Earth's global mean energy budget, and is one of the only available sources for basin-wide TOA and surface radiative fluxes in the Arctic. CERES-EBAF is able to distinguish clouds from underlying sea ice and snow cover by utilizing cloud radiances from the collocated Moderate Resolution Imaging Spectroradiometer (MODIS) and sea ice concentration fields from the National Snow and Ice Data Center (NSIDC, Hollinger et al., 1990). We analyze 15 years of data (2000–14) from CERES-EBAF version 2.87, which further improves the calculation of clear-sky fluxes by including CERES partly cloudy data points in the calculation. We use CERES-EBAF all-sky, clear-sky, and cloud forcing fluxes to identify TOA and surface radiative biases and the relative contributions of clouds.

Seasonal cycle of cloud amount and cloud distribution

To evaluate cloud amount and distribution, we present an analysis of clouds seasonally and spatially. Figure 3.6 illustrates the seasonal cycle of cloud fraction averaged between 70-82°N for a) total, b) low, c) middle and d) high clouds. The model data evaluated here is averaged over the last 25 years of the PI control simulations. From observations, peak cloudiness

occurs during the summer months and a minimum in cloud amount occurs during late winter and early spring. Total cloud amount never drops below 50 percent at anytime. Figure 3.6b shows that low cloud fraction makes up the majority of the total cloud coverage with 40% coverage during the winter months and 60% total coverage during summer. Both middle and high clouds account for 20% coverage throughout the year as shown in Figures 3.6c and 3.6d. Overall, SP-CESM better captures the annual cycle of total cloud coverage in the Arctic compared to observations. Biases arise during the summer months, where SP-CESM overestimates the low cloud fraction up to 20%, but generally agrees with observations during the remainder of the year. CESM overpredicts total cloud fraction by nearly 20% during the winter months. Now we examine the seasonal distribution of clouds across the Arctic basin.

Figure 3.7a and 3.7b illustrate the seasonal distribution of total cloud fraction for SP-CESM and CESM, respectively, compared to CALIPSO-GOCCP. During winter, SP-CESM slightly overestimates the cloud amount over the continental land masses and underestimates over the ocean, but generally agrees well with CALIPSO-GOCCP over the Beaufort Sea and western North America. The opposite is true during summer months, when SP-CESM underestimates cloud amount over much of the basin with the exception of a slight overestimation over the Beaufort Sea and Queen Elizabeth Islands. CESM over predicts basin-wide during winter with a positive bias as high as 40% over the land. During the rest of the year, this overestimation is significantly reduced and cloud amount is only slightly underestimated over land during summer and overestimated during spring and fall. Low clouds tend to dominate in the Arctic region and Figures 3.8a and 3.8b illustrate the spatial distribution of low cloud fraction. The Barents Sea is the cloudiest region during all seasons in the observations and both

models capture the coverage in this region, although CESM tends to slightly overestimate the cloudiness during summer. We also find that both models generally have more clouds over the ocean and less clouds over land, although CESM overpredicts land coverage and severely overestimates the coverage during winter. SP-CESM generally overestimates coverage over land.

From this cloud assessment with CALIPSO-GOCCP, we can see that the clouds are generally simulated in the right place although the actual amount may be slightly overestimated or underestimated. One problem that should be taken into consideration when comparing cloud amount or fraction, in models versus observations, is how a cloud is defined. Because of this definition problem, it is also important to examine cloud forcing.

We next evaluate the net surface and TOA radiative fluxes in the models. This is where the effects of clouds come into play. The seasonal cycles of CESM and SP-CESM surface LW and SW all-sky and clear-sky radiative fluxes across the Arctic basin (70° - 90° N) are compared to CERES-EBAF in Figures 3.9 and 3.10, respectively. For all-sky downwelling and upwelling longwave radiation biases (3.9e and 3.9f) are within 20 - 40 W m^{-2} , resulting in a net LW bias (Figure 3.19d) within 5 - 10 W m^{-2} of CERES-EBAF all year, except during summer, when the bias is larger with CESM. The biases in SP-CESM are smaller in magnitude than those of CESM. When comparing surface net LW clear-sky to CERES-EBAF (Figure 3.9j), both models generally have a negative bias, except during summer. For downwelling SW all-sky (Figure 3.10e), the bias in CESM and SP-CESM are opposite signs, with CESM having too much SW and SP-CESM having too little SW absorbed by the surface during summer. This is due in part to the clouds but also the extent of sea ice in the central Arctic and the amount of snow cover on land in the models. The magnitudes of winter SW all-sky biases are smaller compared to

summer due in part to little to no incoming solar insolation in winter. The upwelling SW bias (Figure 3.10f) is small in SP-CESM while CESM has too much reflected SW. The clear-sky SW biases are generally much better for both models with the exception of CESM upwelling SW clear-sky, with an overestimation of 85 W m^{-2} during summer.

The seasonal cycles of TOA SW and LW radiative fluxes across the Arctic basin are presented in Figure 3.11. The LW TOA all-sky and clear-sky are in good agreement with observations with biases less than 10 W m^{-2} (Figure 3.11f and 3.11i). The SW TOA all-sky are also in agreement throughout most of the year with the exception of late spring and early summer [April–June] with biases between $20\text{--}30 \text{ W m}^{-2}$. Both models have a SW clear-sky bias that is too low by about 80 W m^{-2} in spring and early summer [April–June] and too high by $\sim 20 \text{ W m}^{-2}$ in late summer [July–September]. This clear-sky bias appears to be due to a shift in the maximum of SW at TOA in the models to later in the year or could be from a retrieval error. This should be looked at more closely.

From this analysis, we can say that insufficient cloud amount contributes to SW biases, while excessive middle and high cloud amount year-round contribute to LW biases. The SP-CESM simulated radiative fluxes and distribution of clouds tend to be closer to observations compared to CESM. In this work, the radiative influence of the clouds are most important because of the cloud influence on the surface budget.

3.3 ARCTIC WEATHER STATES

Recent analysis of observations from the Surface Heat Budget Experiment (SHEBA) provides evidence that in winter the Arctic exhibits two preferred and persistent states (Stramler et al., 2011). These observed states, termed “radiatively clear” (hereafter, RC) and “opaquely

cloudy” (hereafter, OC), correspond to cold episodes with cloud emissions close to clear-sky and warm episodes with near-unit emissivity clouds located at or below the peak of an elevated temperature inversion, respectively. (Stramler et al., 2011). In this section, we explore the radiative and microphysical properties of these Arctic clouds and present an analysis of the mechanisms and processes that give rise to them.

Figure 3.12 presents histograms of the seasonal distribution of net surface longwave radiation for SHEBA observations (black) compared to the simulated distributions with SP-CESM (red) and CESM (blue). Stramler et al., (2011) noted a bimodal distribution of winter-weather states during SHEBA, defined by the frequency distribution of net surface longwave radiation, with a peak near 0 W m^{-2} and a secondary peak at roughly -40 W m^{-2} , representing the OC and RC states respectively. The OC state typically has thick, low level, liquid-containing clouds and is characterized by warmer surface temperatures, lower surface pressure, and a near balance between surface downwelling and emitted longwave radiation, while the RC state with ice clouds is characterized by a negative surface longwave budget, high surface pressure, and cold surface temperatures (Morrison et al., 2012).

Liquid-containing clouds in the Arctic generally have large optical depths and a dominant influence on net surface longwave radiation (Shupe and Intrieri, 2004), and can therefore help explain the OC state (Doyle et al., 2011). Ice clouds present during the RC state tend to have small optical depths and a weak influence on net surface longwave radiation (Cesana et al., 2012). From Figure 3.12, during winter (DJF) both models have a peak at -40 W m^{-2} , with a frequency of occurrence similar to SHEBA observations. During the OC state, super-parameterization (SP-CESM) improves the probability distribution compared to CESM, by better

reproducing the observed peak near 0 W m^{-2} . The probability distributions during spring, summer, and fall show the shift towards the OC state throughout the remainder of the year. Since temperature and emissivity drive the amount of net longwave radiation at the surface, in particular the upwelling component, we found winter temperature and humidity also have a bimodal distribution similar to Stramler et al., (2011).

To explain the differences between the models, we turn to the microphysical characteristics. The atmosphere components of CESM and SP-CESM both use the same microphysical scheme, in which cloud phase is predicted based on important processes such as explicit ice nucleation and the Wegener-Bergeron-Findeisen (WBF) process (Wegener, 1911; Bergeron, 1935; Findeisen, 1938). Both models include representations of processes known to be important for the ice-liquid partitioning in clouds. Results show that CESM underestimates the occurrence frequency of the OC state. An underestimation of cloud liquid water amounts in CESM is a known bias (Liu et al., 2011; Barton et al., 2012; Cesana et al., 2012), and likely contributes to the inability of CESM to reproduce observed surface net longwave distribution.

We see that SP-CESM during winter is able to reproduce both radiative peaks in the Arctic much better than the conventional CESM. The microphysics parameterization is the same in the two models, recall from Figure 3.1, the input is very different in SP-CESM, as the microphysics scheme interacts with the CRM rather than the GCM. We expect differences among the models but SP-CESM is generally *better*. SP-CESM is able to resolve key small-scale dynamical processes and therefore as a result, the feedback to the larger-scale model is different.

To further explore the surface and atmospheric processes that influence these states, Figure 3.13 and 3.14 show the mean vertical profiles of temperature and humidity for the

radiatively clear and opaquely cloudy states, respectively, as observed during SHEBA(black), and simulated by SP-CESM (blue) and CESM (red). Temperature inversions are present in both states with a colder surface-based inversion occurring during the RC state (net LW $\sim -40 \text{ W m}^{-2}$) and a peak at -30°C and -20°C at roughly 1 km for CESM and SP-CESM, respectively. The stable layer associated with the OC state is elevated in observations which neither model is able to capture. The surface is warmer during the OC state (net LW $\sim 0 \text{ W m}^{-2}$) with an elevated inversion at 900 hPa ($\sim 2 \text{ km}$) peaking at -14°C (CESM) and -18°C (SP-CESM). Humidity inversions are also present during both states and tend to coincide with the peaks of the temperature inversions. Humidity at the surface is lower during the RC state and increases as the atmosphere transitions to the OC state. The elevated inversions of both temperature and humidity typically occur at the top of the mixed layer. Stramler (2006) found that over the SHEBA drift station typical temperature inversions associated with Net LW $\sim 0 \text{ W m}^{-2}$ had a peak at 2°C at 2 km and net LW $\sim -40 \text{ W m}^{-2}$ had a peak at -24°C about 1km lower. Results shown here are slightly colder compared to SHEBA, but that is expected since our results are for profiles averaged over the whole Arctic basin.

Cloud phase is an important indicator of the Arctic winter state. Figure 3.15 presents the vertical distribution of DJF cloud ice (mg kg^{-1}) and DJF cloud liquid (mg kg^{-1}) mixing ratios for the climate models. Liquid water during winter is typically found between $60^\circ\text{-}70^\circ\text{N}$, below 4 km with more liquid water in SP-CESM compared to CESM. This is not surprising given the frequency-of-occurrence probability distributions shown in Figure 3.12. Ice water path is also higher in SP-CESM. A maximum in ice water path is found between $80^\circ\text{-}90^\circ\text{N}$ in the lowest kilometer of the atmosphere and also higher in the atmosphere around 10 km. There is drastically

less ice in CESM and it tends to occur at higher altitudes between 60-70°N. To take a more detailed look at the clouds during each winter state, a composite analysis was conducted to examine the clouds during individual events. Ten radiatively clear and ten opaquely cloudy events were identified based on the distribution of daily net longwave radiation. Figure 3.16 shows the vertical distribution of cloud ice and cloud liquid for events that occurred during the three-month period DJF. Panels a-b and e-f show the distributions of cloud ice and liquid (mg kg⁻¹) during the radiatively clear state for CESM and SP-CESM respectively, and panels c-d and g-h are for the opaquely cloudy state. During the radiatively clear state in CESM, Arctic ice clouds are present (mixing ratios less than 3 mg kg⁻¹), with a maximum near 70°N and a small amount of cloud liquid in the lowest 2 km between 60-70°N. SP-CESM generally has more cloud ice at 90°N and between 70°-80°N. Liquid clouds are also present between 60°-70°N. The opaquely cloudy state is quite different between the models. SP-CESM has a significant amount of cloud ice, four times more ice than during the clear state, throughout the Arctic from the surface through 10 km. Liquid clouds are also present closer to the surface, with mixing ratios on the order of 35 mg kg⁻¹. During the radiatively clear state in CESM, cloud ice only appears between 60°-70°N with little to no cloud liquid.

This evaluation shows that the input from super-parameterization makes a dramatic difference in the representation of the weather states, and even more so with the microphysical characteristics of the clouds.

3.4 EFFECTS OF SUPER-PARAMETERIZATION ON ARCTIC WARMING

3.4.1 GLOBAL CLIMATE CHANGE

As in Chapter 2, we begin this chapter by analyzing the global climate response to elevated CO₂ but with SP-CESM. Later, we also compare the 4xCO₂ climates between the conventional CESM and SP-CESM.

The global surface temperature simulated by SP-CESM is shown in Figure 3.17, in terms of annual and seasonal averages for the PI Control (a-c) and climate change (4xCO₂ minus PI Control, panels d-f). Similarly to CESM, the Earth warms globally at 4xCO₂ by 4.9 K (0.7 K cooler than CESM), with the greatest warming during the winter at high latitudes. Simulated Arctic warming ranges from 14-18 K with SP-CESM, which is 2-7 K less than the warming simulated by CESM. Cooling over the North Atlantic is also present in SP-CESM at 4xCO₂. Panels g-l of Figure 3.17, show the 4xCO₂ surface temperature for CESM and SP-CESM and the difference is shown in panels m-o. Spatially, surface temperatures are similar for the two models at 4xCO₂, but with a few exceptions. SSTs in the southern ocean are slightly warmer in SP-CESM (1-2 K). Greater differences are found over the continents, where SP-CESM is 1-5 K warmer, especially over Antarctica during JJA and over the western United States. During DJF, surface temperatures over South America and Australia are also warmer by a few degrees.

As the Earth warms, sea ice cover decreases (Figure 3.18). In the annual mean, more than half of the sea ice area disappears in SP-CESM and nearly all of the ice melts near Antarctica. A comparison of the 4xCO₂ climates, illustrates that SP-CESM generally has more sea ice in the Northern Hemisphere compared to CESM, while both models have little to no sea ice in the Southern Hemisphere.

As the air warms, the total column water vapor (shown in Figure 3.19) increases globally by 8.5 kg m^{-2} in SP-CESM ($\sim 2 \text{ kg m}^{-2}$ less than CESM), with the greatest increases in the tropics. As in CESM, water vapor in the high latitudes nearly doubles. At $4x\text{CO}_2$, SP-CESM tends to have more (less) water vapor in the Southern (Northern) Hemisphere compared to CESM. The greatest differences are found in the region of the Inter-Tropical Convergence Zone (ITCZ). Interestingly, there is an increase over central Africa and northern Australia during JJA. The increase over central Africa may be due to a more pronounced Atlantic cold tongue (James et al., 2013).

The hydrological cycle strengthens in SP-CESM, with both precipitation and evaporation increasing in the warmer $4x\text{CO}_2$ climate (Figures 3.20 and 3.21). There is a decrease in evaporation in the North Atlantic at $4x\text{CO}_2$ due to colder sea surface temperatures in the region. Annually and seasonally at $4x\text{CO}_2$, SP-CESM tends to have less precipitation and evaporation over land compared to CESM. During JJA, SP-CESM has increased precipitation over the eastern warm pool and central Africa, compared to CESM.

Figures 3.22 and 3.23 present the global distribution of total and low cloud amount. As the climate changes, the global distribution of low clouds in SP-CESM decreases by a few percent. It is important to note that the clouds are strikingly different between CESM and SP-CESM. Recall from Chapter 2, the global mean total cloud amount with CESM was 63% and in SP-CESM, it is 55%. Observations from ISCCP, indicate that the global annual mean cloud amount is roughly $\sim 67\%$, and therefore in the global mean, CESM is more realistic. There is roughly a 10% decline in cloud amount between the two simulations, which has an impact on not only the cloud forcing, but also the amount of energy within the atmosphere. This is also why the

land warms up more in CESM compared to SP-CESM. Comparing the cloud amount at $4\times\text{CO}_2$ between the models, SP-CESM has about 14% less total cloud globally. Besides the differences in global mean cloud amount, the other striking difference is the presence of more Arctic clouds during summer in SP-CESM. As the climate warms in SP-CESM, the clouds cool the atmosphere by a few W m^{-2} which is shown in the shortwave cloud forcing (SWCF) presented in Figure 3.24. The difference between CESM and SP-CESM at $4\times\text{CO}_2$ is small ($< 0.5 \text{ W m}^{-2}$). Larger differences arise in the longwave cloud forcing (LWCF) presented in Figure 3.25. The warmer climate in SP-CESM has a decrease in annual mean longwave cloud forcing of 4 W m^{-2} which is due in part to the decrease in clouds, resulting in less warming of the atmosphere and surface from the clouds. There is a 3 W m^{-2} difference between CESM and SP-CESM at $4\times\text{CO}_2$ in LWCF. The changes in SWCF and LWCF balance and this is shown in Figure 3.26 with the total cloud radiative forcing.

3.4.2 DARK WARMING IN SP-CESM

We now return to our discussion in Chapter 2 related to the mechanisms that explain Arctic amplification during winter, but this time with the super-parameterized CESM (SP-CESM).

Effects of super-parameterization on the ice-insulation feedback

Figure 3.27 presents the seasonally varying trends of the simulated Arctic means of selected fields. The first 15 years of the plots are from the end of the CESM $4\times\text{CO}_2$ simulation and the vertical white line delineates the beginning of the SP-CESM $4\times\text{CO}_2$ simulation. The response to increased CO_2 are similar to those obtained with CESM, although slightly weaker, but we will discuss the major differences in some detail.

Surface temperatures (Figure 3.27a) are slightly cooler in SP-CESM compared to CESM during winter and summer. Sea-ice thickness is larger during winter as shown in Figure 3.27b and returns earlier in the season. The amount of total column water vapor during winter is about the same but we can see that the atmosphere has slightly less moisture during the summer (Figure 3.27c). Figure 3.27d illustrates an abrupt decline in total cloudiness (i.e. both low and high cloud) from November through May and a slight increase during the summer months. As expected, this would have a significant impact on the amount of net longwave reaching the surface, which is shown in Figure 3.27g, with a sharp 5-10 W m^{-2} decrease in net longwave during winter and summer. Both the sensible and latent heat fluxes decrease from October through January, as shown in Figures 3.27e and 3.27f respectively, due to the increase in sea ice extent and thickness, as there is more insulation at the surface and less evaporation taking place. Due to the decreases in these fluxes, there is a little less warming and moistening of the atmosphere. With the change in total cloudiness, downwelling longwave radiation decreases (increases) by a few W m^{-2} during winter (summer). The spatial pattern of the downwelling longwave radiation is shown in Figure 3.28a. Similar to CESM, DLR increases over the whole Arctic basin, and is the greatest over the Arctic Ocean, in particular over the Beaufort Sea. Figure 3.28b shows that during NDJ about 20 of the 70 W m^{-2} (28%) comes from the effects of clouds. Recall from Chapter 2, that clouds accounted for 40 of the 80 W m^{-2} (50%) increase in CESM. Roughly one-third of the DLR increase is from the effects of clouds in SP-CESM, and the rest is due to clear-sky effects. Figure 3.29 shows the contribution of the DLR increase from emissivity and

temperature. Averaged over the polar cap, the changes in emissivity and temperature contribute 8.78 W m^{-2} and 49.27 W m^{-2} , respectively, to the increase in wintertime DLR. As in CESM, the increase in DLR is mostly due to an increase in the warming of the air.

Surface absorbed solar radiation is nearly the same between CESM and SP-CESM. The changes in the energy budget of the Arctic are shown in panels j, k, and l of Figure 3.27. The changes are not too different compared to CESM, although the cooling at the surface increases during winter due to the increased sea ice and results in more energy loss into the atmosphere from November through March. The Arctic atmosphere in SP-CESM is still cooled by the diabatic effects at the surface and the top of the atmosphere, but cools more strongly than results shown with CESM.

The Arctic Winter Monsoon in SP-CESM

We now turn to the large-scale atmospheric circulation that acts to reinforce the ice-insulation feedback. Similar to CESM, Figure 3.30a shows the evolution of the difference between the surface air temperature over the Arctic Ocean and the surface temperature over the continental land masses poleward of 60°N . The air above the Arctic Ocean cools by 3 K compared to CESM but is still 12 K warmer than the surrounding land. The strong thermal contrasts between the warmer ocean and surrounding continents is still in place and Figure 3.30b illustrates that during winter a thermal low is still present due to the decrease in sea level pressure.

To examine the large-scale circulation further, Figure 3.31a and 3.31b shows maps of the NDJ sea level pressure at $4\times\text{CO}_2$ and the difference between $4\times\text{CO}_2$ and PI Control respectively, as simulated by SP-CESM. The low pressure system is just as

strong as in CESM, but it has shifted towards the east over the Bering Sea and across the eastern Arctic seas. The high pressure systems over Greenland and the North Atlantic have strengthened, while the Siberian High has weakened. Panels c, d, and e of Figure 3.31, show that the winter monsoonal circulation is still present and in some regions has intensified relative to CESM. At $4xCO_2$, there is a strong thermal gradient between the continental land masses and the Arctic Ocean, and the meridional temperature gradients near the land-ocean borders of have reversed. The low-level flow from land towards the Arctic Ocean has intensified in the regions of the Beaufort, Barents, and Kara Seas. SP-CESM has stronger low-level winds over the Beaufort Sea, compared to those in CESM.

The SP-CESM simulated total diabatic heating of the atmosphere is shown in Figure 3.32. In the PI control, there is stronger diabatic cooling at all levels due to the longwave radiation — similar to CESM. At $4xCO_2$, the Arctic atmosphere is weakly heated in the regions of the Chukchi (992-957 hPa) and Barents (992-887 hPa) seas. The atmosphere is not heated as much with SP-CESM because vertical diffusion of sensible heat and latent heat release are weaker. Similar to CESM, a strong diabatic warming occurs equator-ward of the Arctic region in the PI control because of the ocean-land temperature gradients in those regions and this heating is reduced at $4xCO_2$ due to the weaker temperature gradient. As shown in Chapter 2 for both CESM and SP-CESM, the simulated Arctic warming in winter is primarily due to a weakening of the diabatic cooling of the Arctic atmosphere and the energy transported from lower latitudes decreases during winter, as the climate warms.

In summary, processes at work in CESM and SP-CESM are quite similar. Their strength is slightly weaker in SP-CESM. Some differences between CESM and SP-CESM, for example, the sharp decline in cloudiness at $4xCO_2$, are quite striking, and call for further research.

3.4.3 ARCTIC WEATHER STATES AT $4xCO_2$

Under increased carbon dioxide in the atmosphere, how will the Arctic weather states change? At $4xCO_2$ the winter climate is 20 K warmer and sea ice has decreased to less than 10 cm. Thinner sea ice and larger fluxes of water vapor could yield different frequencies of occurrence of the radiatively clear (RC) and opaquely cloudy (OC) states, as well as higher temperatures at the interfaces between atmosphere, snow, and ice (Stramler et al., 2011).

In the present-day climate, the distinct bi-modal regime is commonly found during winter (DJF). At $4xCO_2$, there is still evidence of these distinct states during winter as presented in Figure 3.33a. SP-CESM has two peaks ~ 0 and -60 W m^{-2} and the frequency of occurrence has decreased compared to the present-day climate. There does not appear to be a state at $4xCO_2$ that is more preferred than the other. CESM at $4xCO_2$ during winter has the RC state but struggles to have the second peak during the OC state, again due to the lack of ice clouds. Interestingly, we also see two distinct regimes arise during spring (Figure 3.33b) especially with SP-CESM. The OC state is associated with a surface net LW of 0 W m^{-2} and the RC peak has shifted by 20 W m^{-2} to -60 W m^{-2} , compared to the present-day climate. The vertical profiles of specific humidity and temperature (Figure 3.34) are quite different compared to the present day climate. The atmosphere has become more humid with humidity values nearly doubling. The surface-based inversions during the RC state have collapsed. The structure of the humidity profile from the

surface to 900 mb is quite interesting. SP-CESM has a stable atmosphere and humidity increases from the surface to the peak of the inversion at 900 mb, while the humidity inversion in CESM begins around 950 mb and is almost 1.5 g kg^{-1} more humid than SP-CESM. Surface temperatures have warmed and the temperature distinction between the two states has decreased (Figure 3.34 top). The temperature inversion during the cloudy state is quite similar between CESM and SP-CESM, with CESM being slightly warmer. Simulated cloud structures have changed dramatically compared the present-day climate and the models suggest more mixed-phase clouds. CESM has more ice in the lower levels during the RC states as compared to SP-CESM and virtually no cloud liquid, where SP-CESM has 20 mg kg^{-1} . During the cloudy state, both models have more cloud liquid compared to the present-day state, but SP-CESM has significantly more liquid near the surface throughout the Arctic as shown in Figure 3.35.

3.5 SUMMARY

In this chapter, we examined the effects of super-parameterization on the Arctic climate. We explored the representation of the Arctic atmosphere in SP-CESM, by evaluating several important atmospheric characteristics because of their significant implications on the regional and global climate. We also found that SP-CESM better simulates surface temperature, sea ice area and thickness, and sea level pressure compared to the to the conventional CESM. We examined the distribution and seasonal cycle of clouds and radiation with SP-CESM and found the simulated results to be closer to observations.

The presence of the Arctic winter states is a distinct and persistent feature of the Arctic climate. We showed that these states are influenced by the radiative and microphysical features

of the clouds, and affect the surface radiative fluxes. Due to better representation of the cloud microphysics, we find that the SP-CESM is able to better reproduce both of the preferred winter states, compared to CESM.

The results shown here as well as in previous studies, shows that the SP-CESM is able to do a reasonable job representing key features of our global climate. The causes are unclear as to why SP-CESM is able to better simulate these key features of the Arctic climate, but we think it may be due to improved simulations of tropical convection. Further investigations are needed but are beyond the scope of this study.

3.6 FIGURES

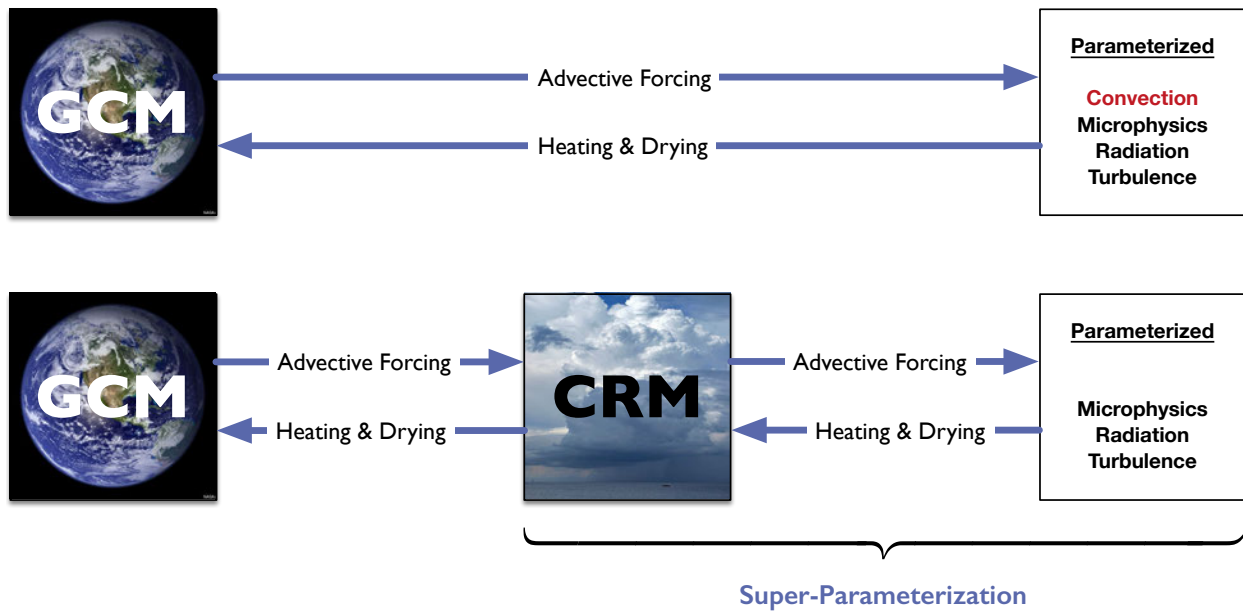


Figure 3.1 Illustration of the differences in the GCM with and without super-parameterization.

Surface Temperature

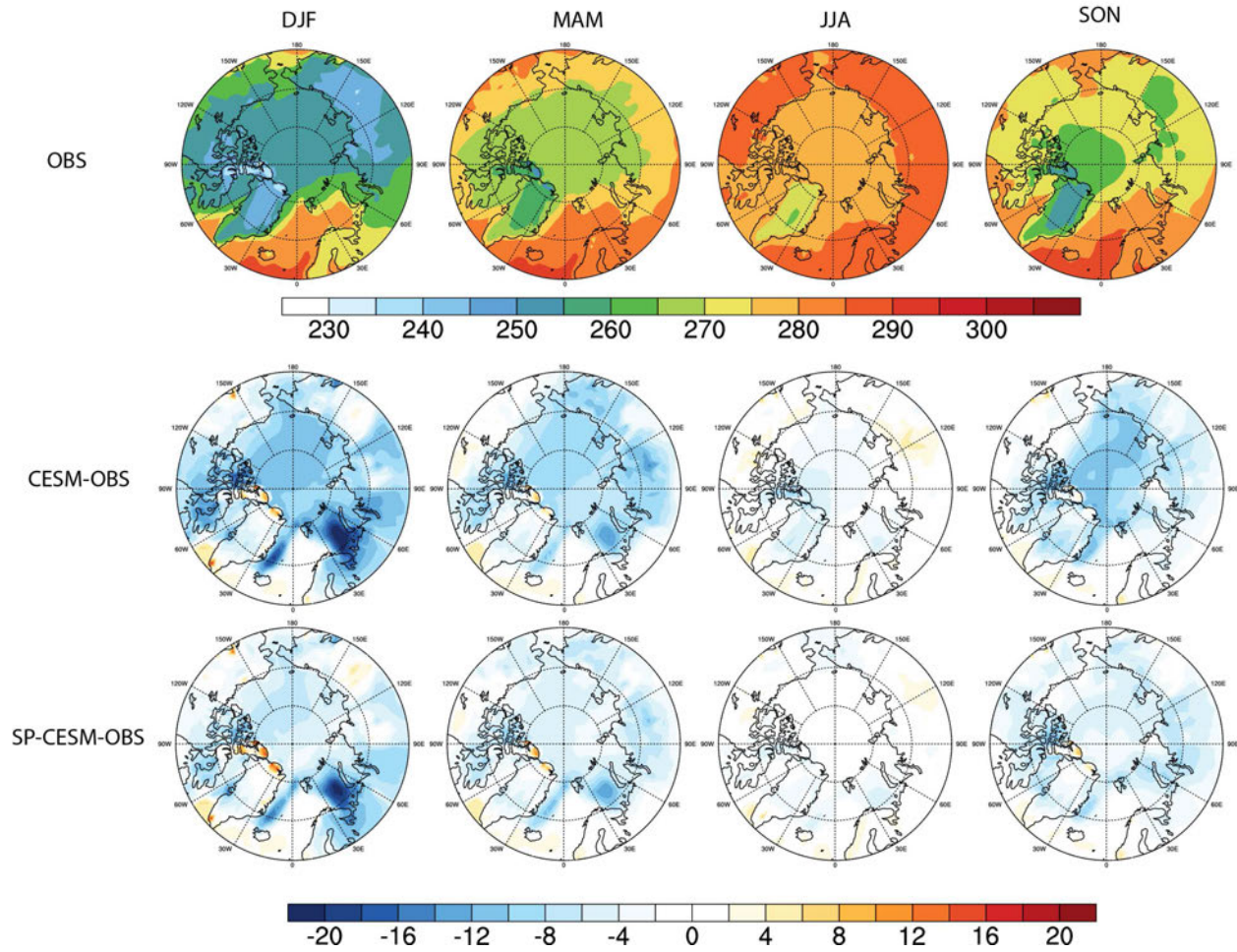


Figure 3.2. Polar stereographic maps of seasonal surface temperature (K) for observations, CESM, and SP-CESM.

Mean Sea Level Pressure, DJF

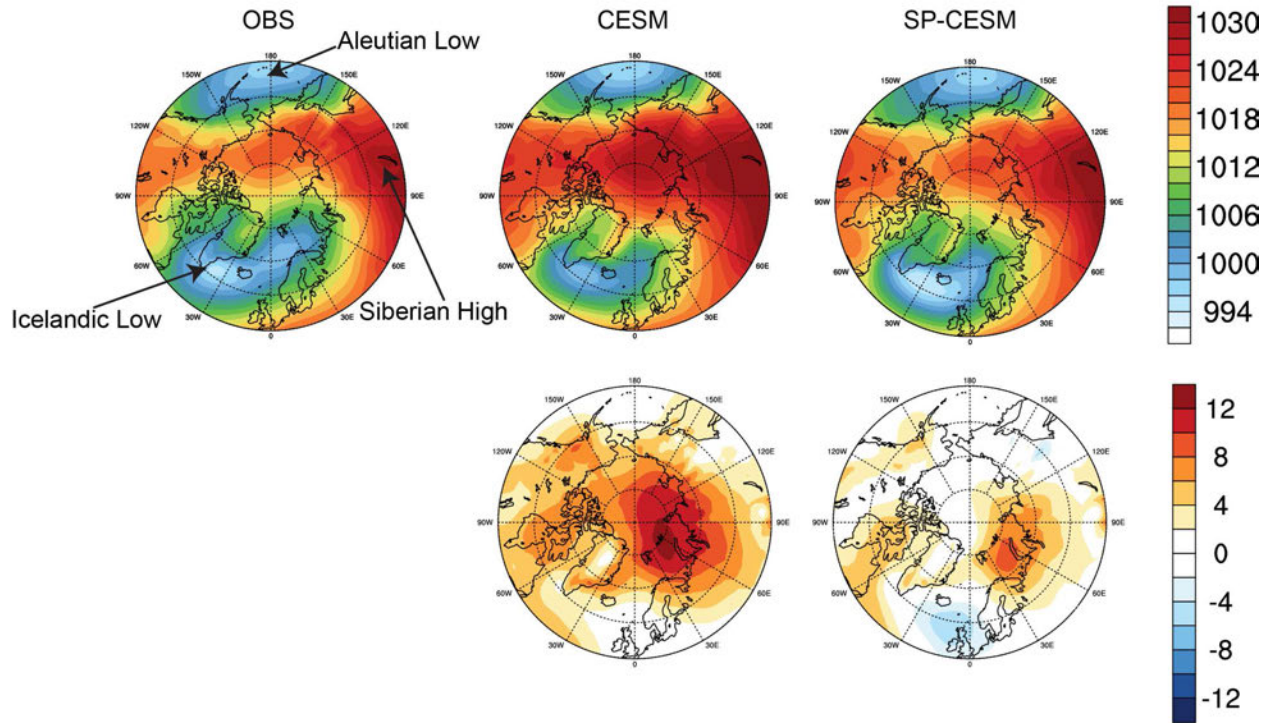


Figure 3.3a. Polar stereographic maps of DJF (December-January-February) mean sea level pressure (hPa) for observations, CESM, and SP-CESM.

Mean Sea Level Pressure, MAM

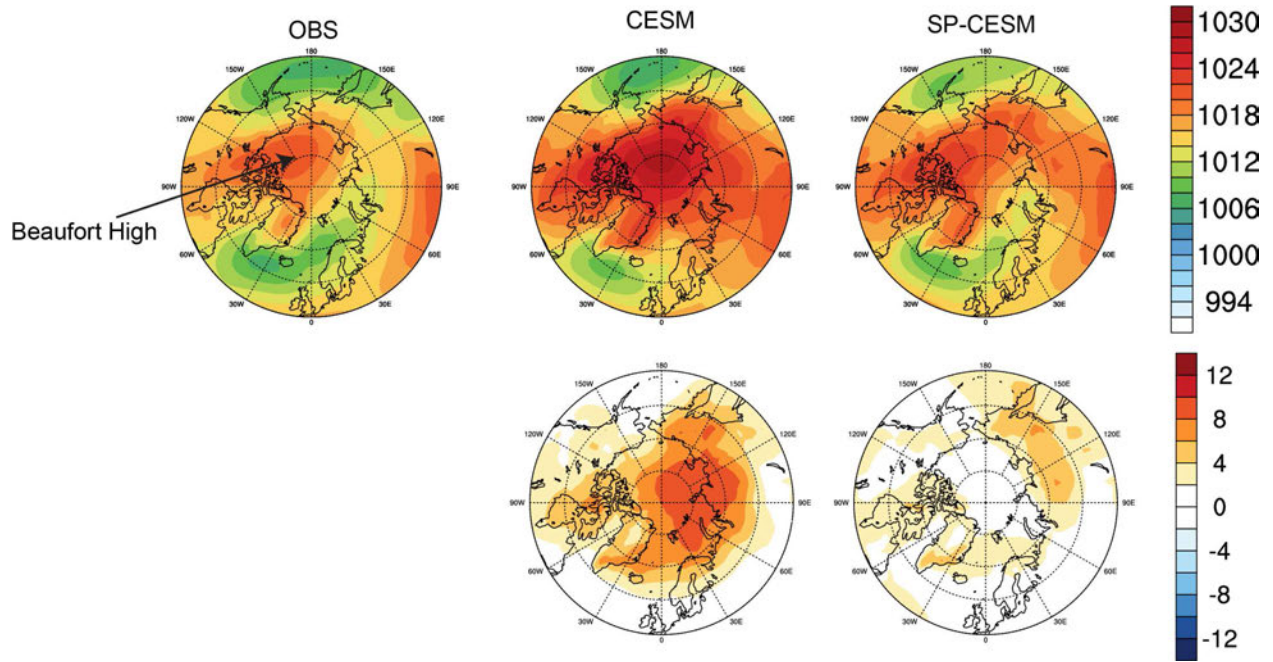


Figure 3.3b. As in Figure 3.3a but for MAM (March-April-May).

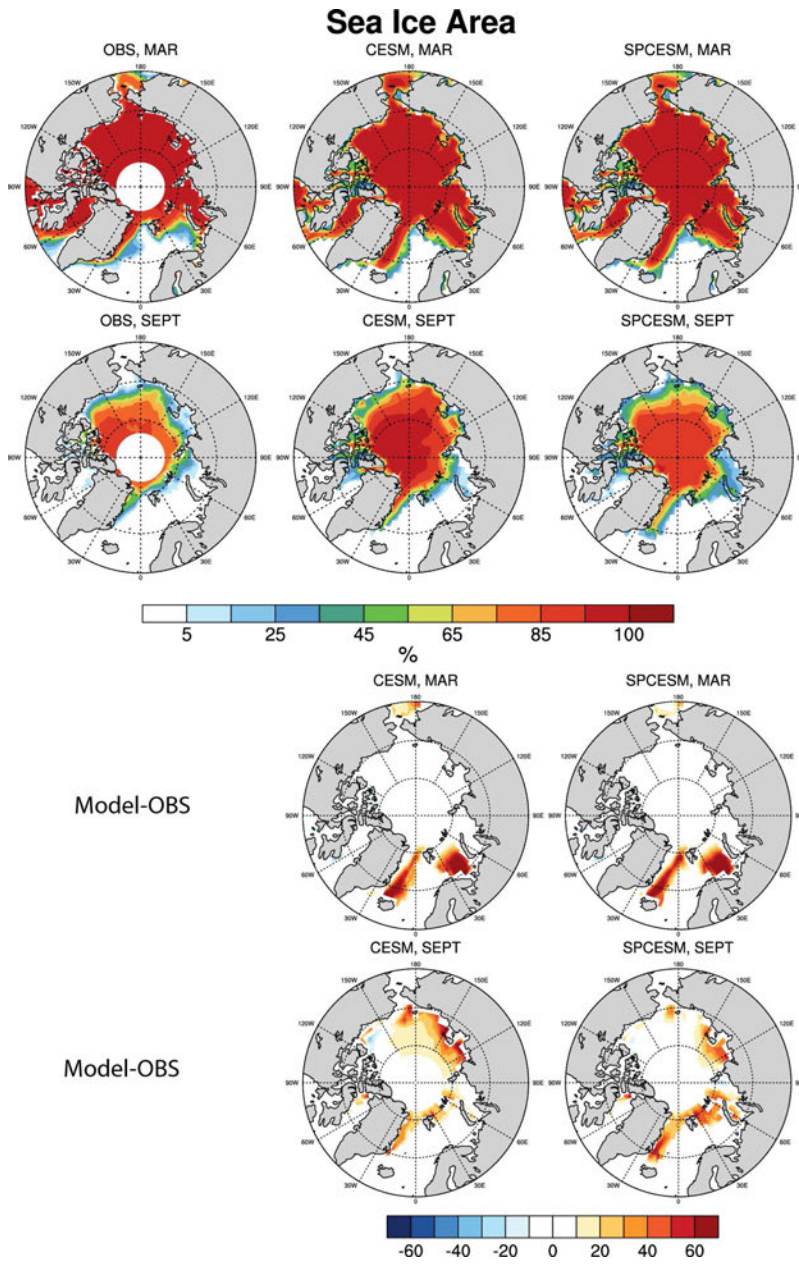


Figure 3.4. Polar stereographic maps of sea-ice area (%) for observations, CESM, and SP-CESM for March (top row) and September (bottom row). The model biases are shown in the bottom two panels.

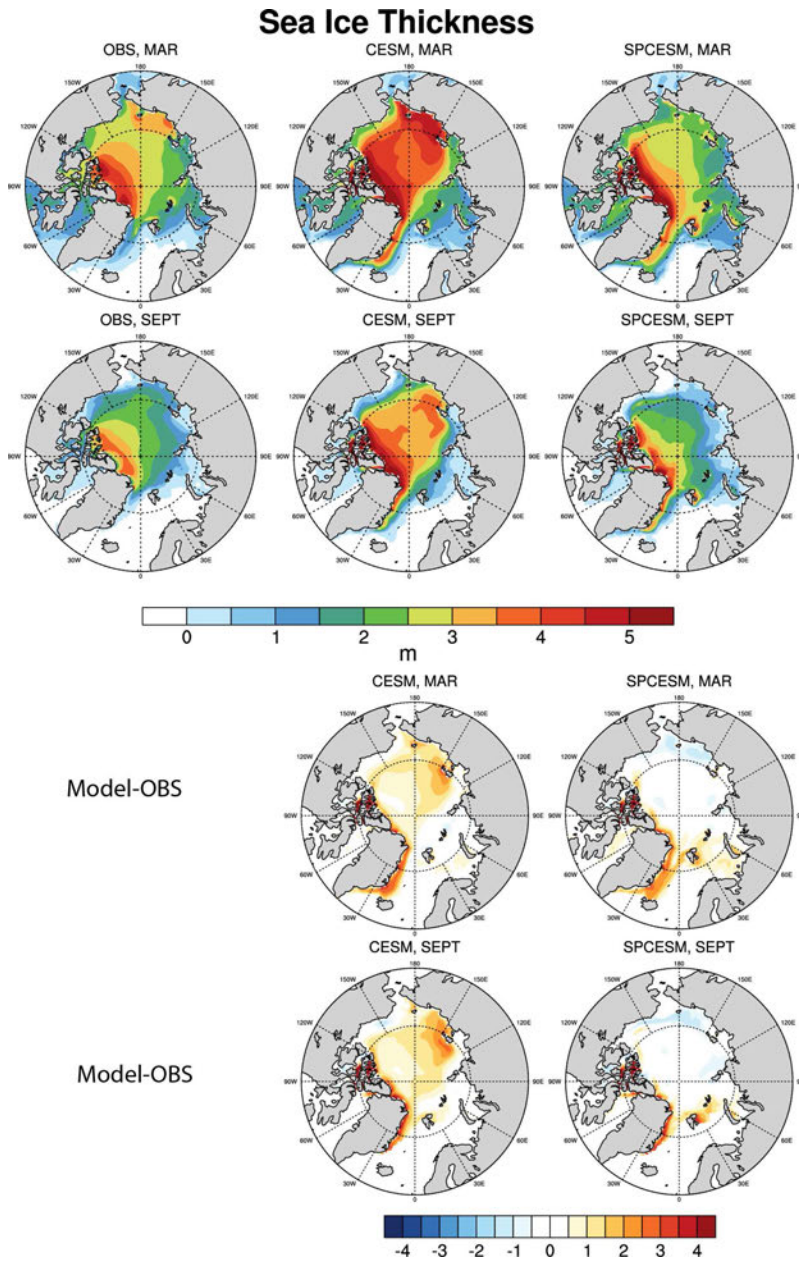


Figure 3.5. Polar stereographic maps of sea-ice thickness (meters) for observations, CESM, and SP-CESM for March (top row) and September (bottom row). The model biases are shown in the bottom two panels.

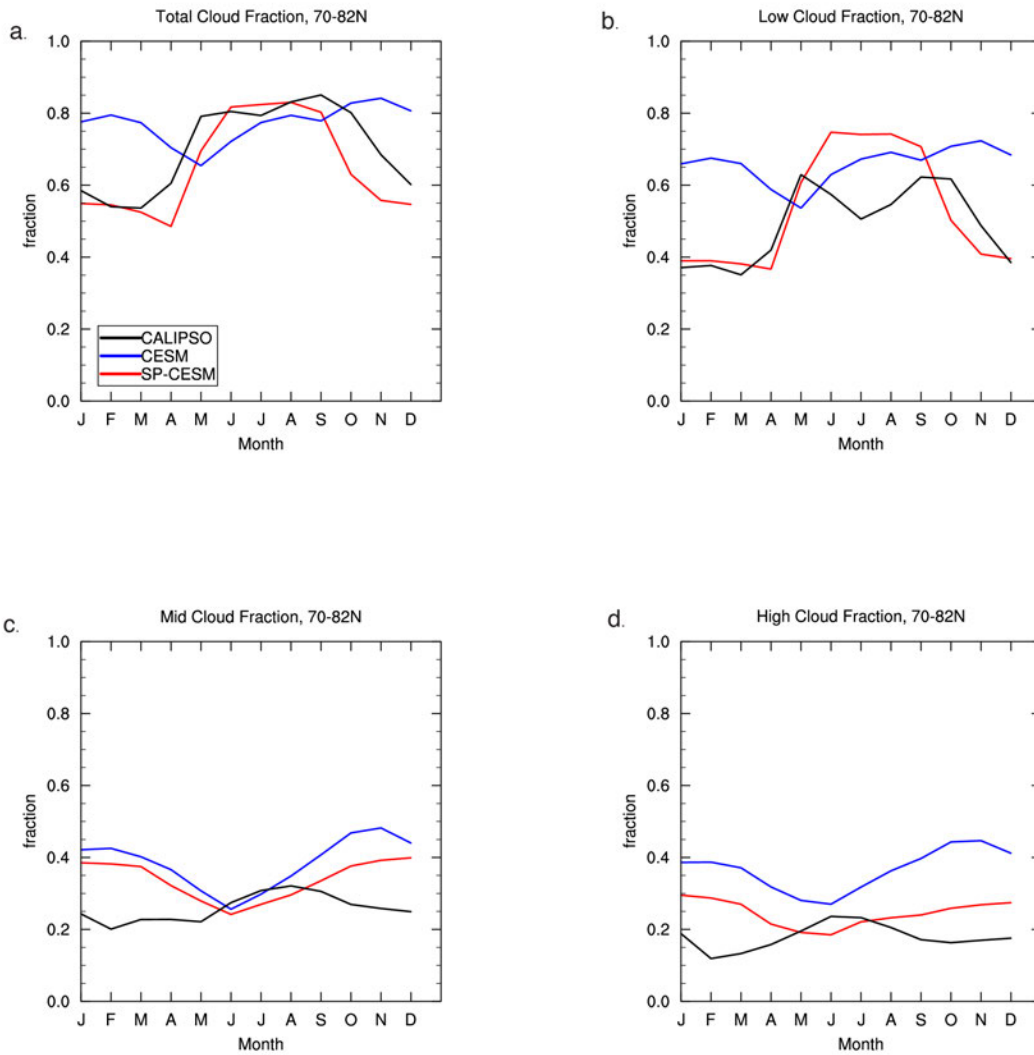


Figure 3.6. Seasonal cycle of monthly average a) total, b) low, c) middle, and d) high cloud fraction from 60-82°N for 7-yr average (2007–2013) of CALIPSO-GOCCP observations (black) and model simulations with CESM (blue) and SP-CESM (red).

Total Cloud Fraction, SP-CESM and CALIPSO

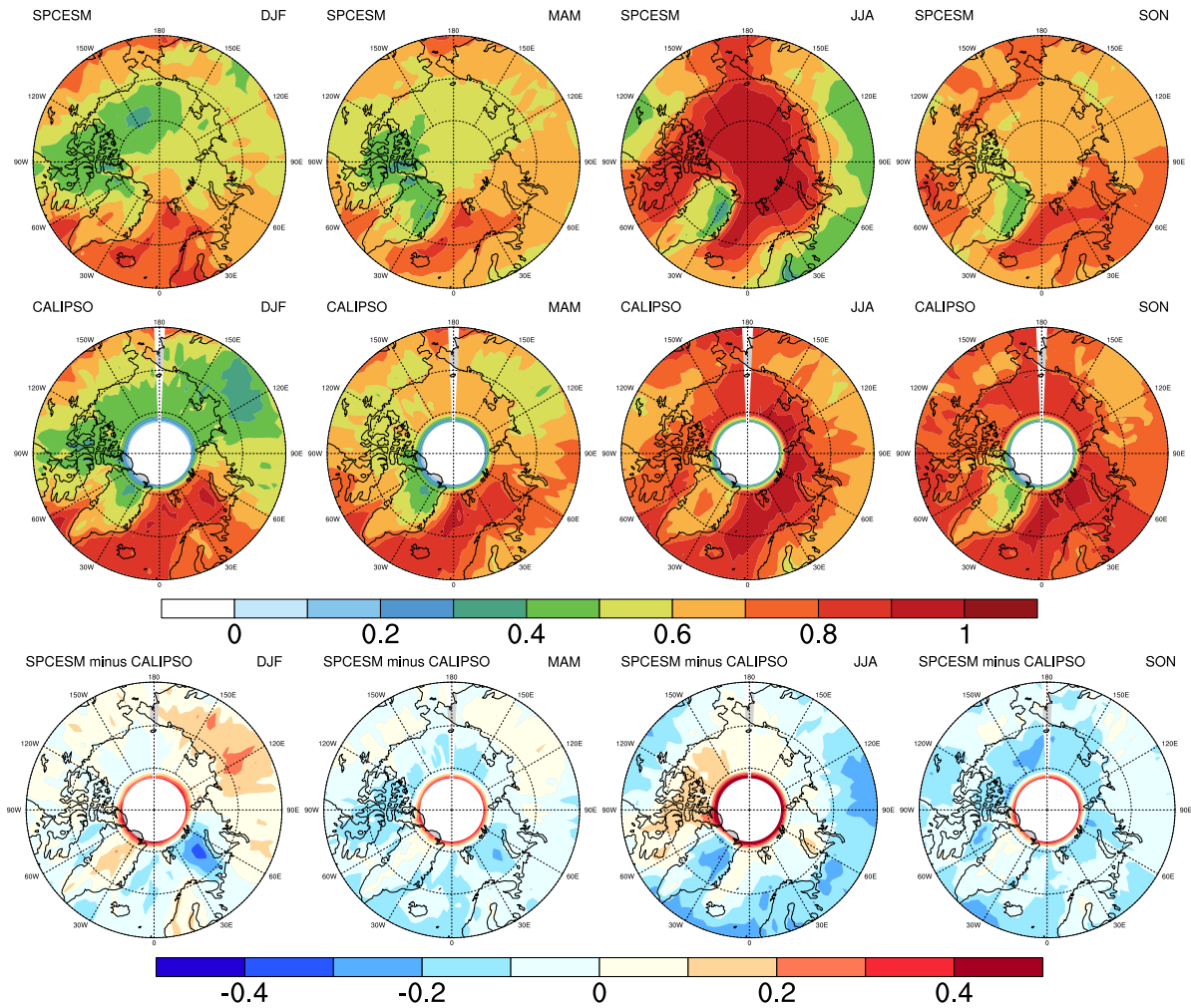


Figure 3.7a. Polar stereographic maps of seasonal averages of total cloud fraction with SP-CESM (top) and CALIPSO-GOCCP (middle) and the SP-CESM bias (bottom). A positive bias means the model predicts excess cloud compared to observations.

Total Cloud Fraction, CESM and CALIPSO

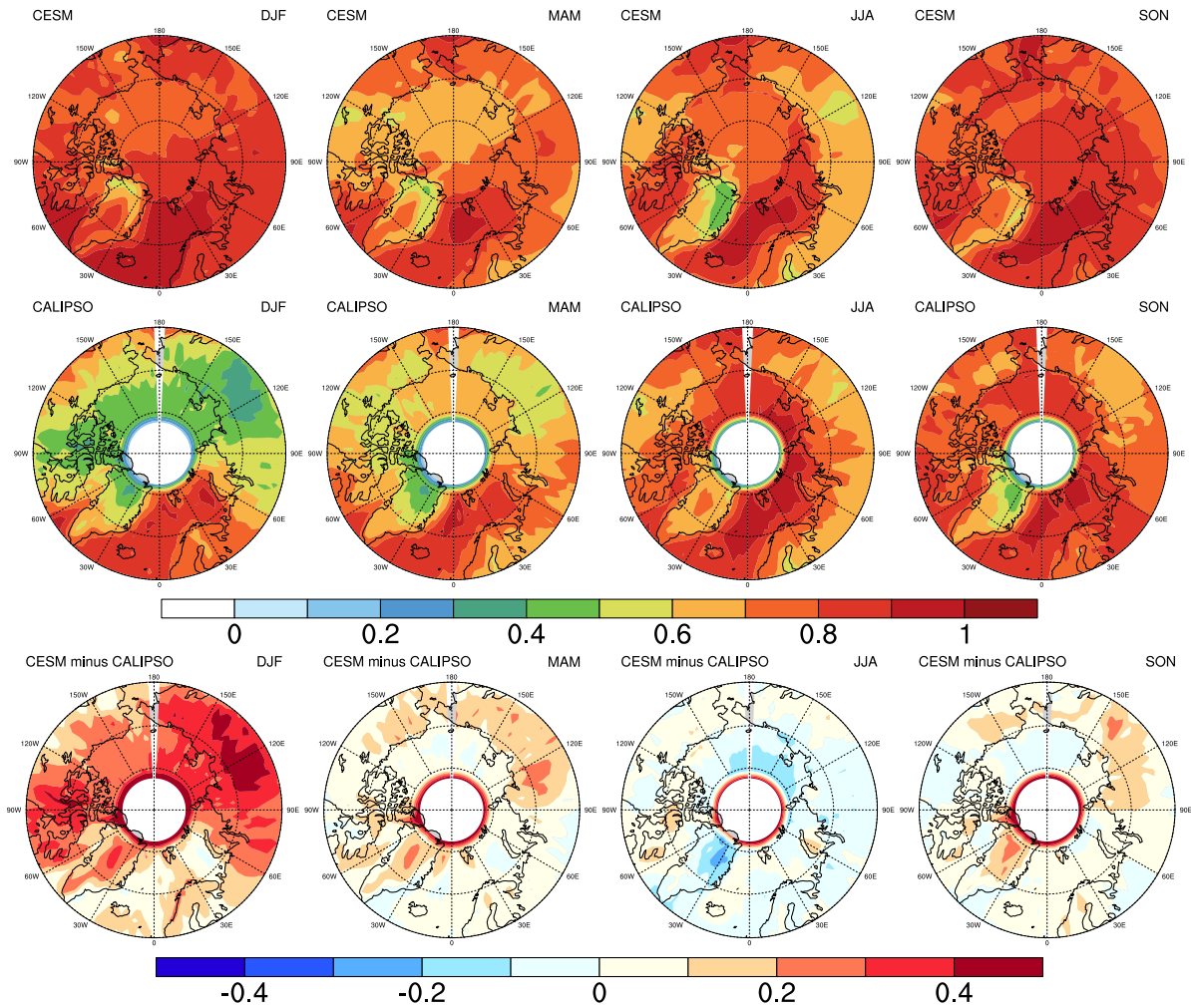


Figure 3.7b. Polar stereographic maps of seasonal averages of total cloud fraction with CESM (top) and CALIPSO-GOCCP (middle) and the CESM bias (bottom). A positive bias means the model predicts excess cloud compared to observations.

Low Cloud Fraction, SP-CESM and CALIPSO

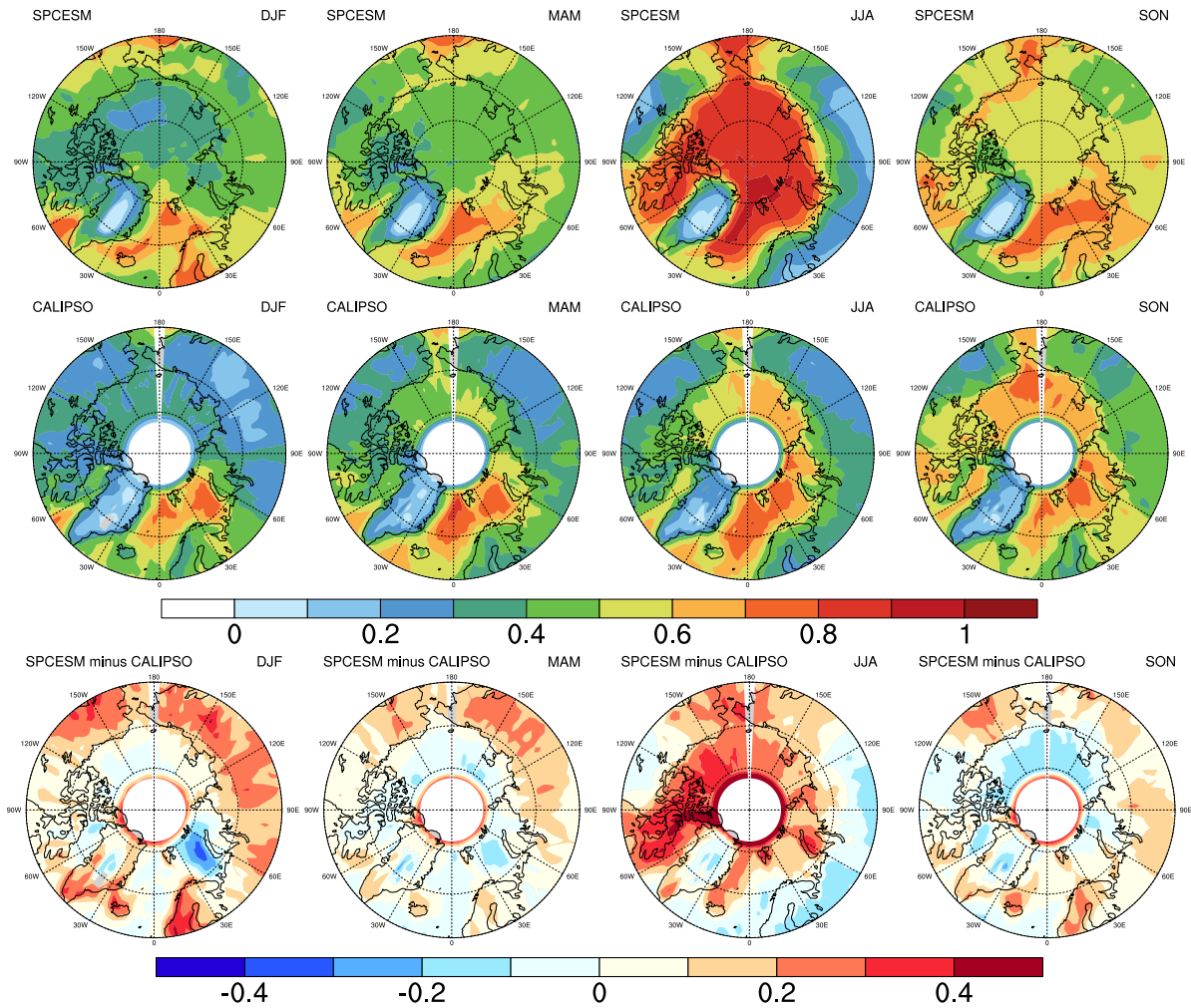


Figure 3.8a. Polar stereographic maps of seasonal averages of low cloud fraction with SP-CESM (top) and CALIPSO-GOCCP (middle) and the SP-CESM bias (bottom). A positive bias means the model predicts excess cloud compared to observations.

Low Cloud Fraction, CESM and CALIPSO

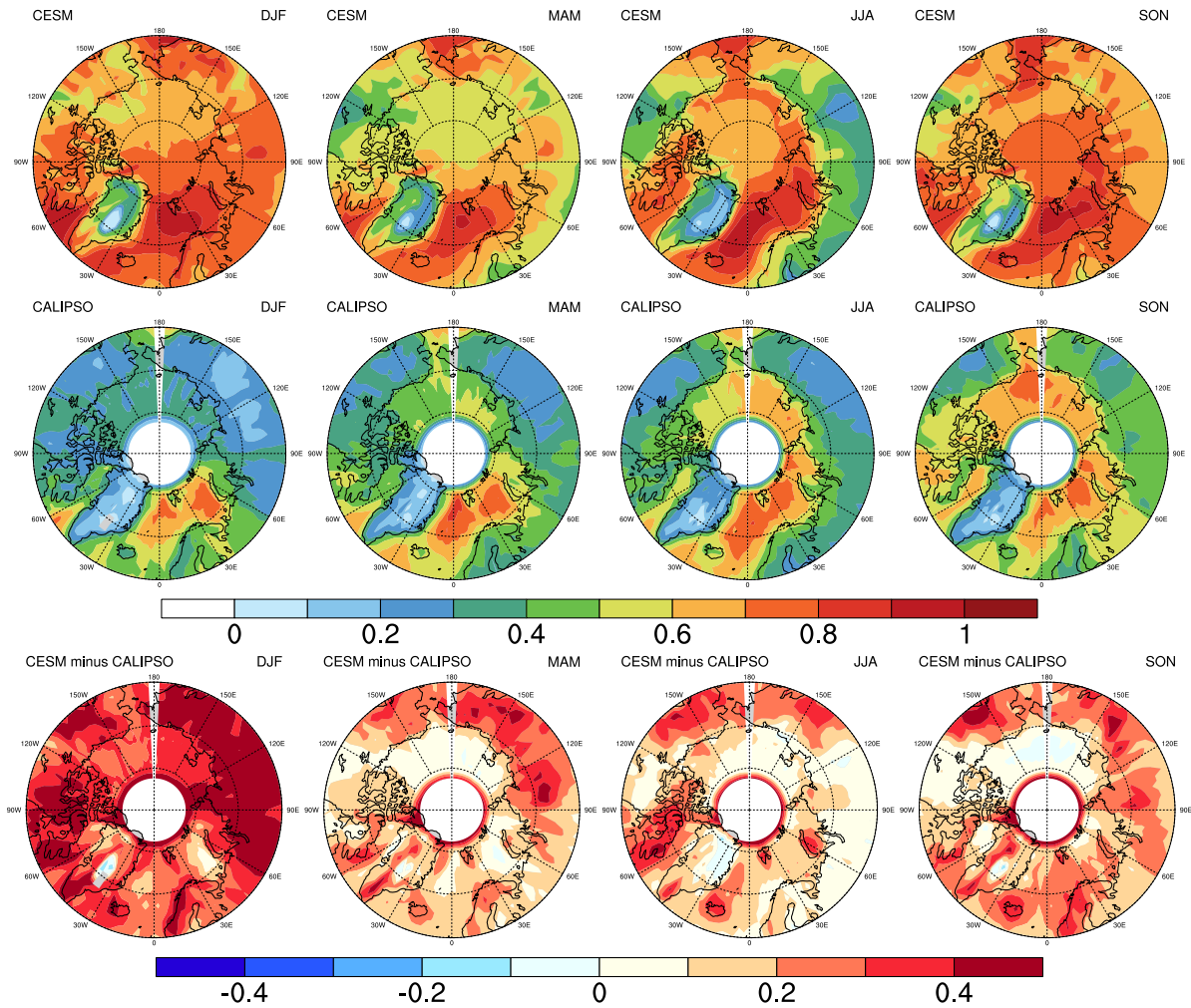


Figure 3.8b. Polar stereographic maps of seasonal averages of low cloud fraction with CESM (top) and CALIPSO-GOCCP (middle) and the CESM bias (bottom). A positive bias means the model predicts excess cloud compared to observations.

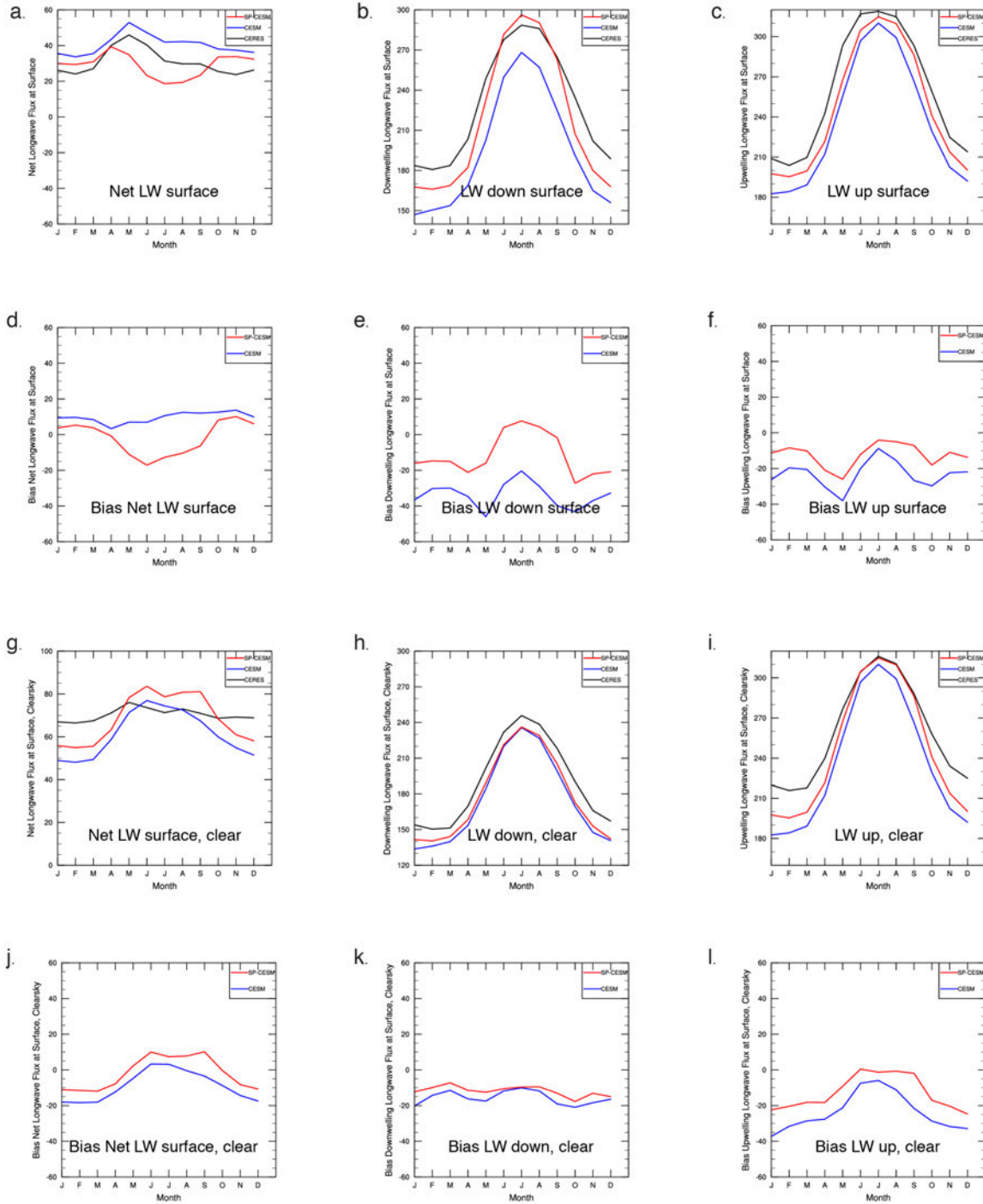


Figure 3.9. Arctic (70°-90°N) surface longwave all sky and clear sky radiative fluxes for the models and CERES-EBAF observations. Biases (model minus obs) are shown in panels d-f and j-l. A positive bias means the model predicts excess LW fluxes into the Arctic compared to observations.

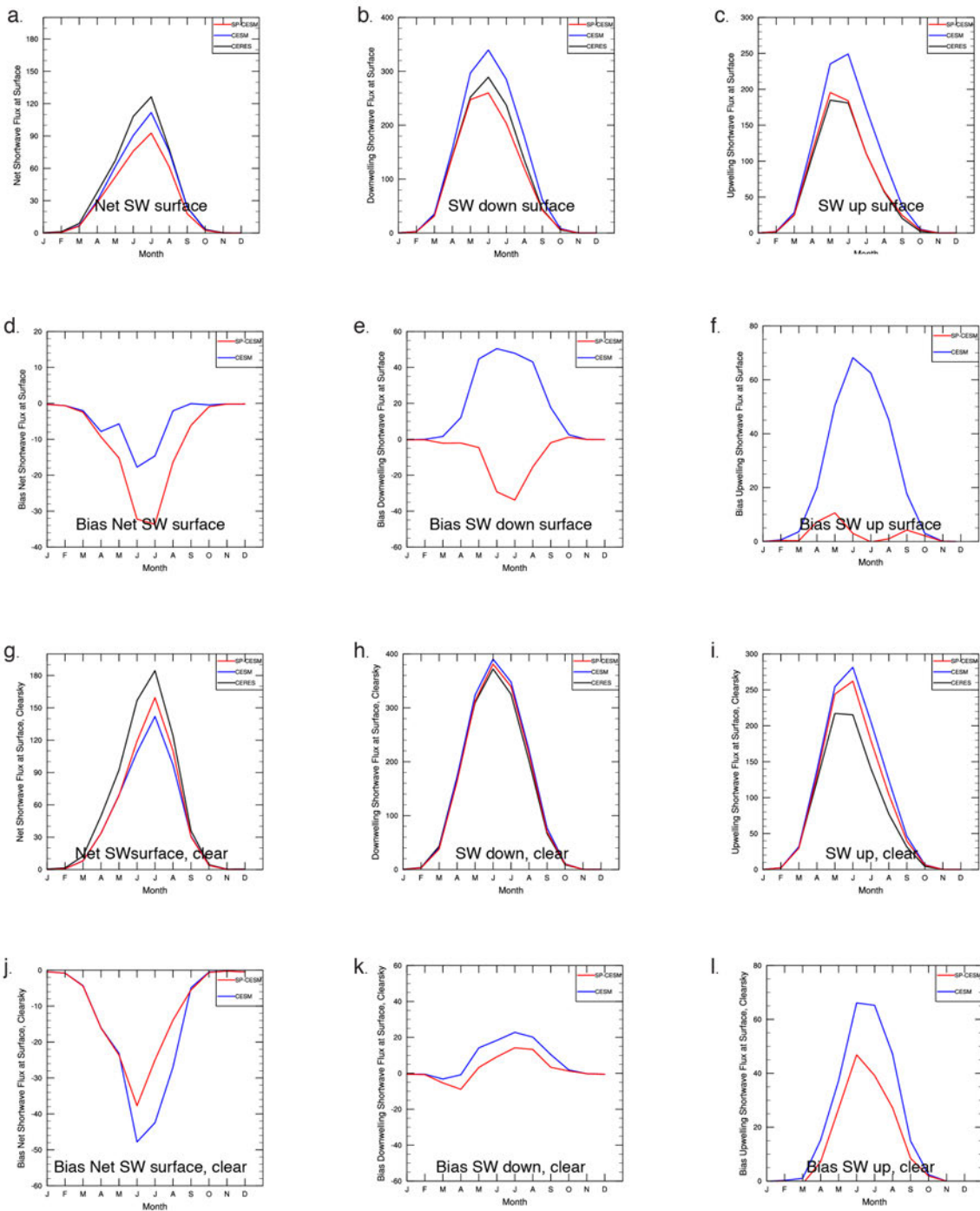


Figure 3.10. Arctic (70° - 90° N) surface shortwave all sky and clear sky radiative fluxes for the models and CERES-EBAF observations. Biases (model minus obs) are shown in panels d-f and j-l. A positive bias means the model predicts excess SW fluxes into the Arctic compared to observations.

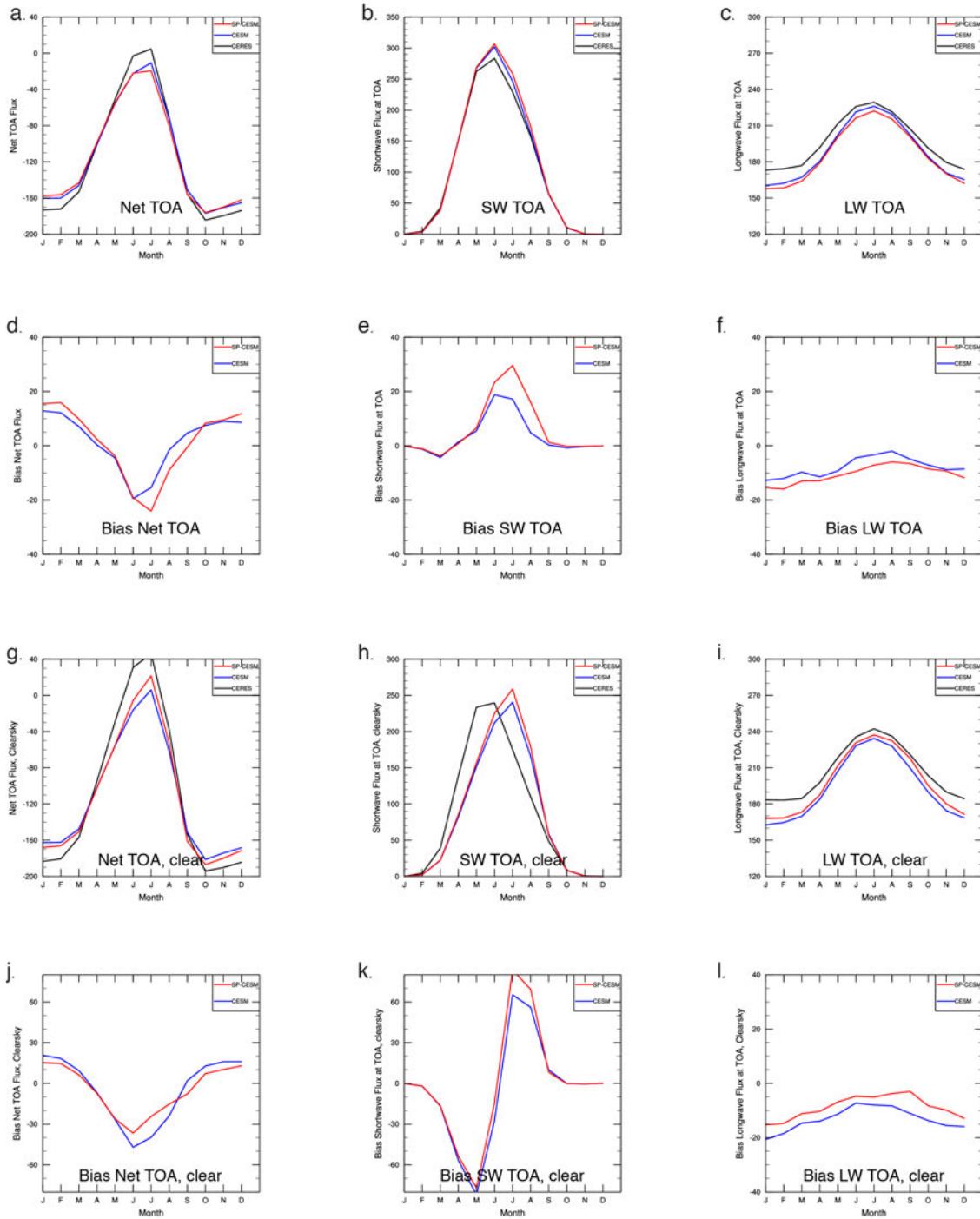


Figure 3.11. Arctic (70-90N) TOA shortwave and longwave all sky and clear sky radiative fluxes for the models and CERES-EBAF observations. Biases (model minus obs) are shown in panels d-f and j-l. A positive bias means the model predicts excess fluxes into the Arctic compared to observations.

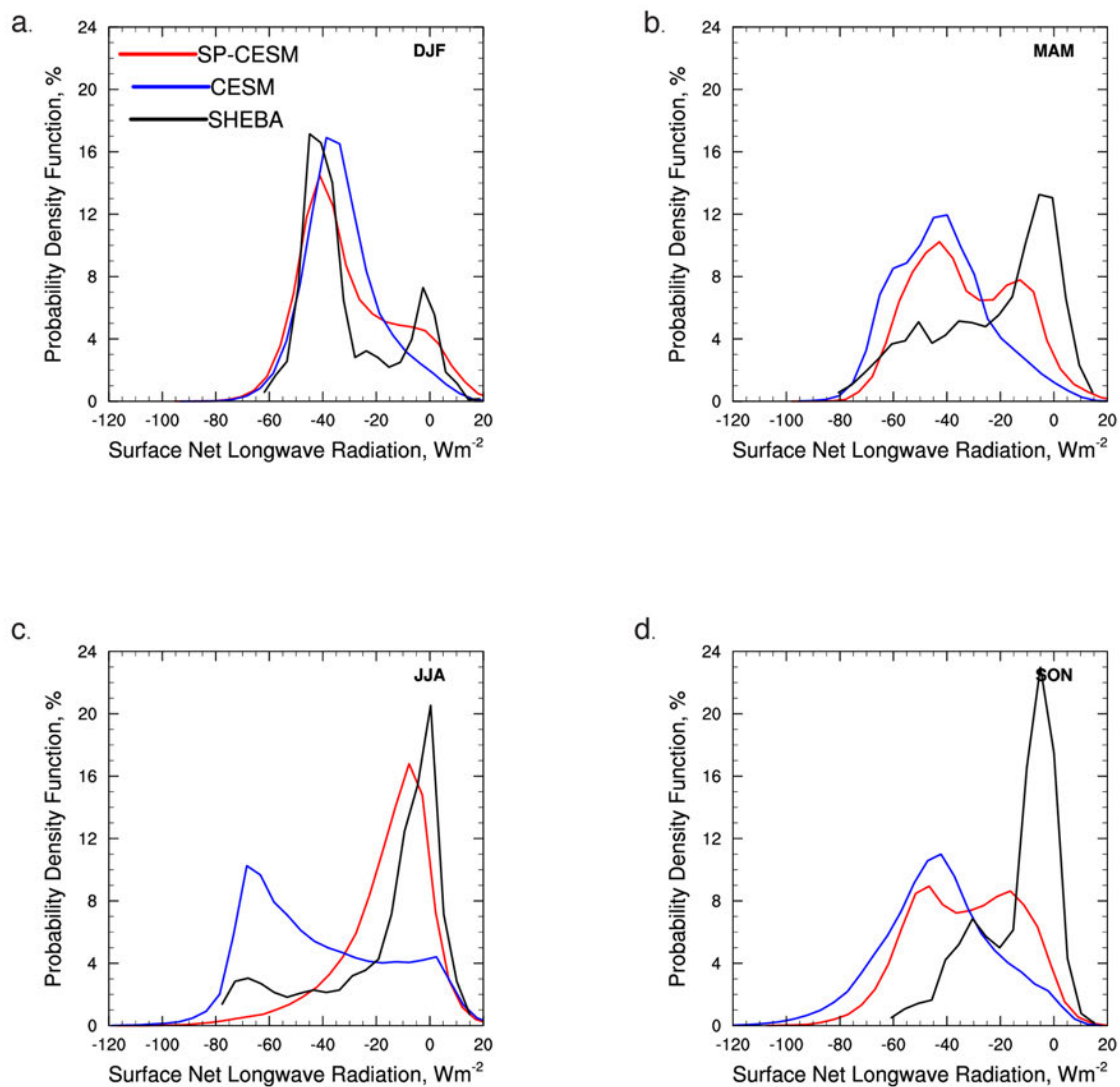


Figure 3.12. Histograms of the seasonal distributions of surface net longwave radiation for SHEBA observations (black) and the climate models with CESM (blue) and SP-CESM (red). Bin spacing is 5 Wm^{-2} .

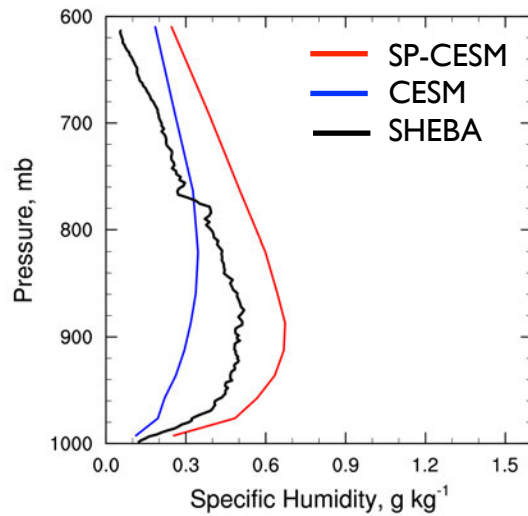
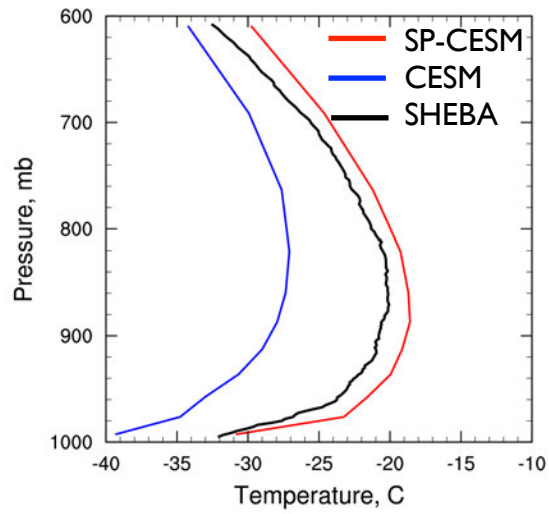


Figure 3.13. Simulated daily averaged vertical profiles of temperature (top) and specific humidity (bottom) for SHEBA (black), CESM (blue), and SP-CESM (red) for the radiatively clear state.

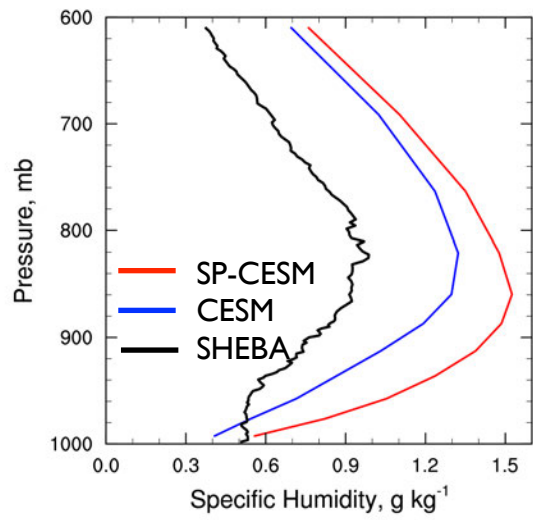
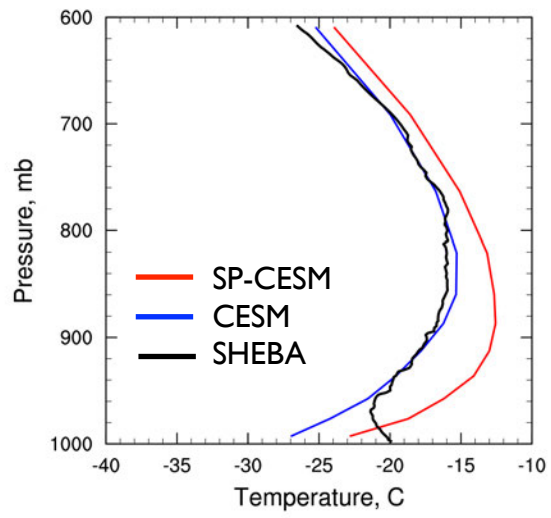
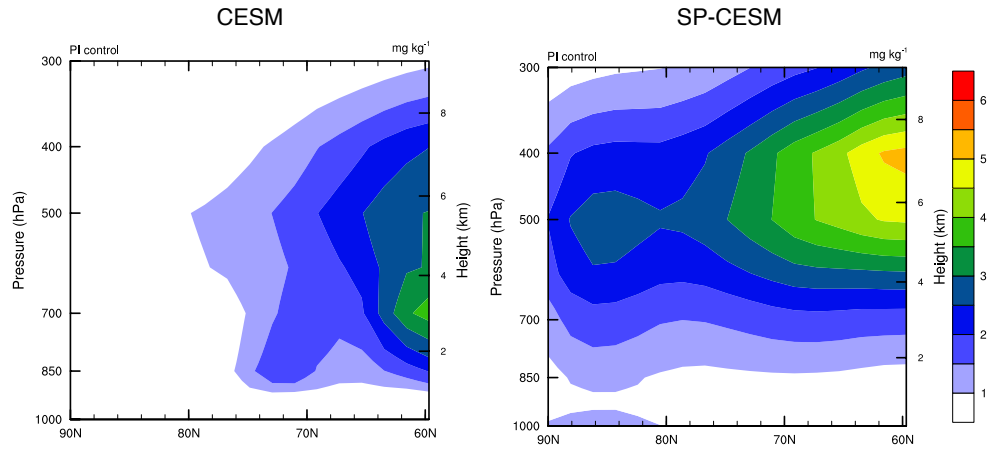


Figure 3.14. As in Figure 3.13 but for the opaquely cloudy state.

DJF Cloud ice
mg kg⁻¹



DJF Cloud liquid
mg kg⁻¹

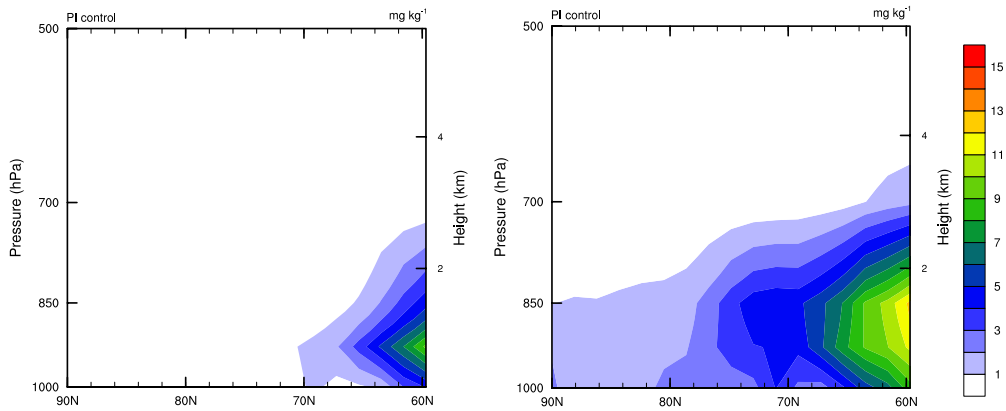


Figure 3.15. Vertical distribution of DJF cloud ice (mg kg⁻¹) and DJF cloud liquid (mg kg⁻¹) for the climate models.

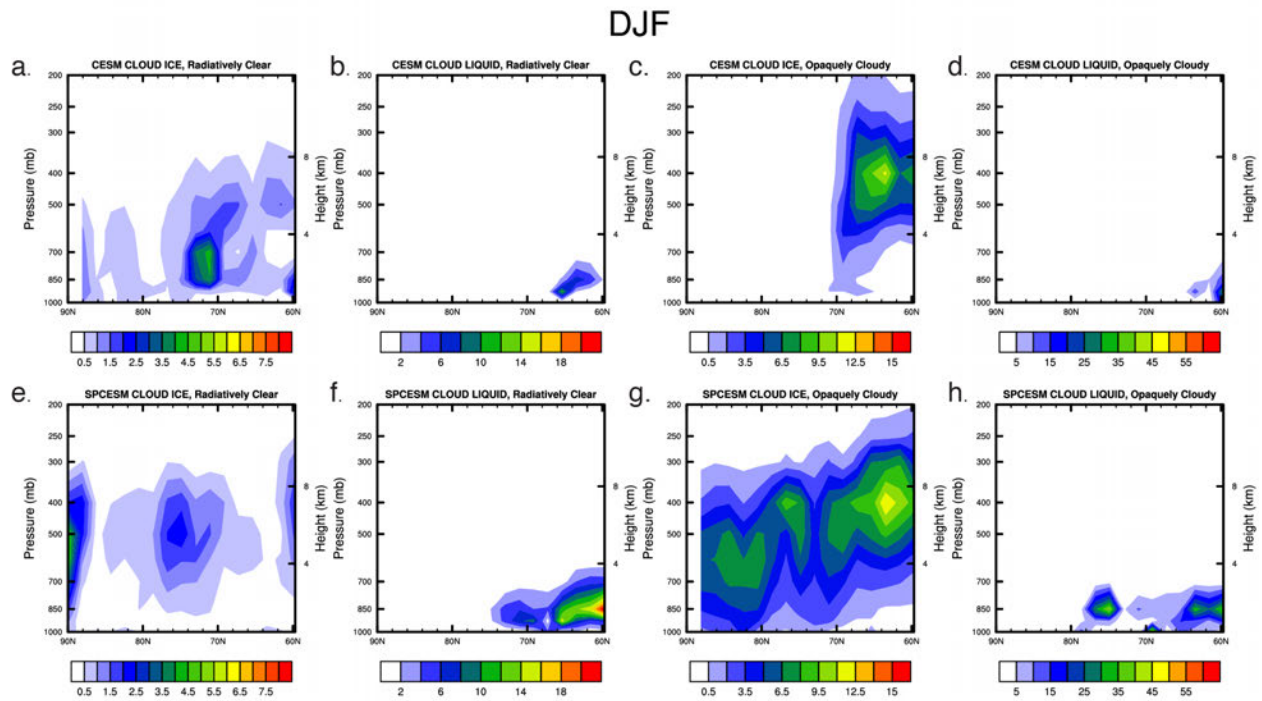


Figure 3.16. Vertical distribution of cloud ice (mg kg^{-1}) and cloud liquid (mg kg^{-1}) during DJF for the radiatively clear and opaquely states for the climate models.

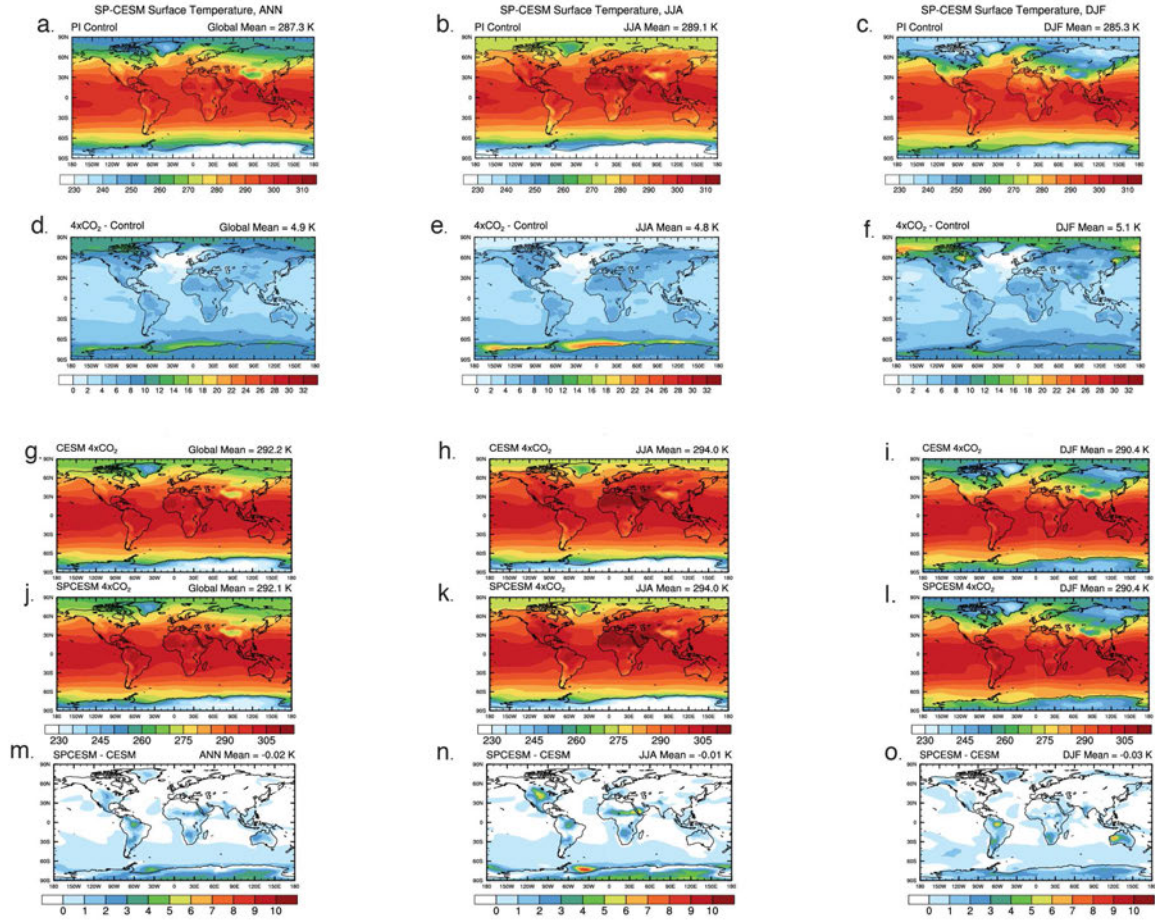


Figure 3.17. (a-e) Global maps of SP-CESM annual and seasonal simulated surface temperature for PI control and climate change ($4xCO_2$ minus PI Control). (g-o) Global maps of annual and seasonal simulated surface temperature at $4xCO_2$ for CESM, SP-CESM, and the difference (SP-CESM minus CESM).

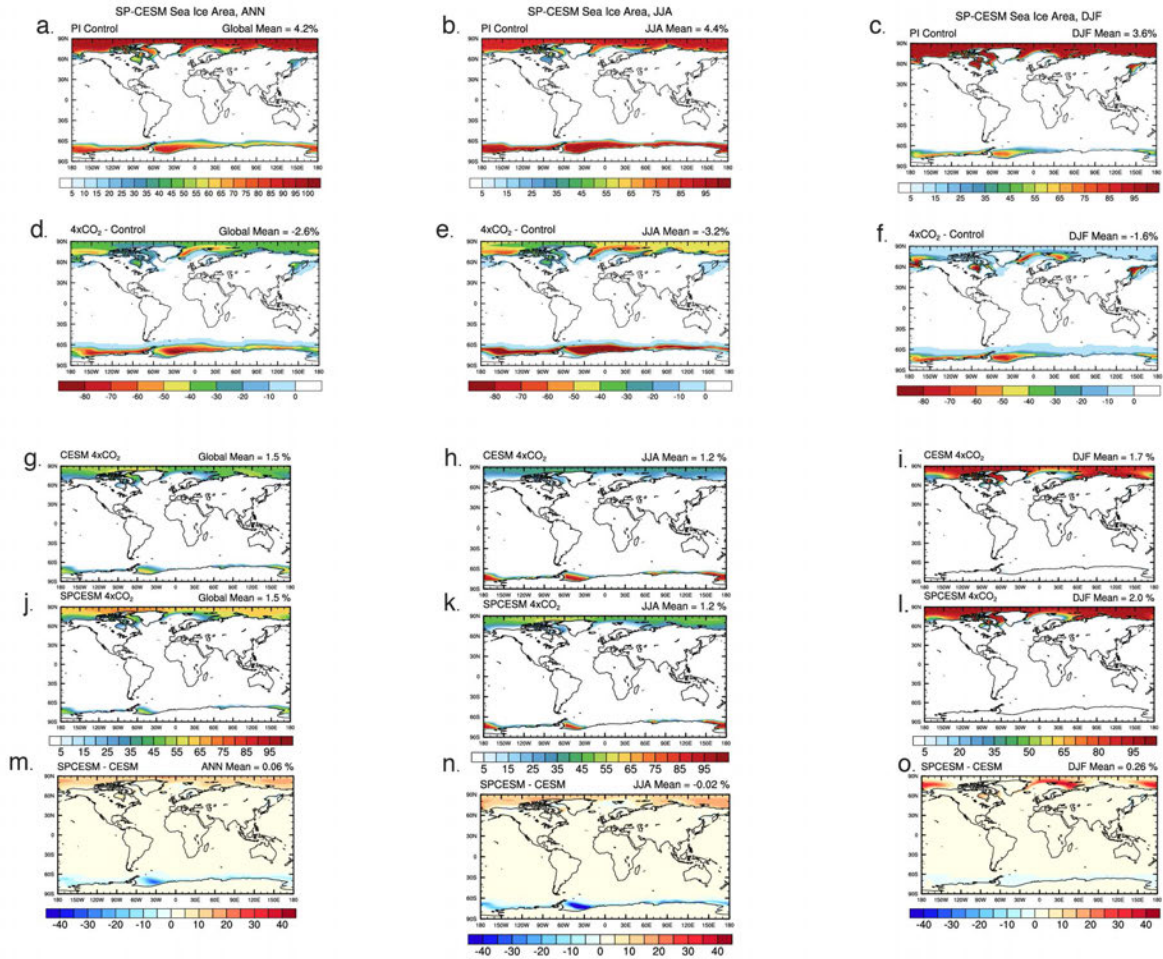


Figure 3.18. As in Figure 3.17, but for sea ice area.

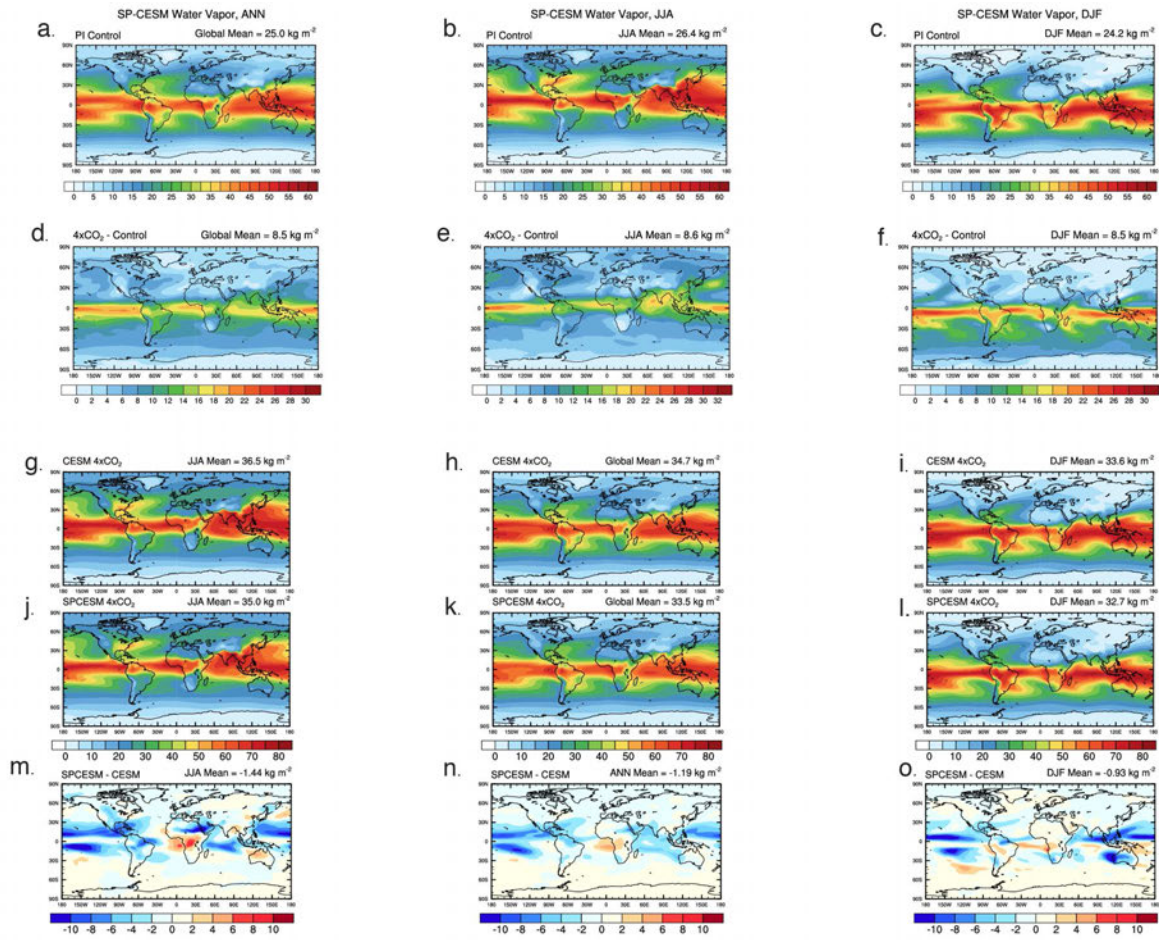


Figure 3.19. As in Figure 3.17, but for vertically integrated water vapor.

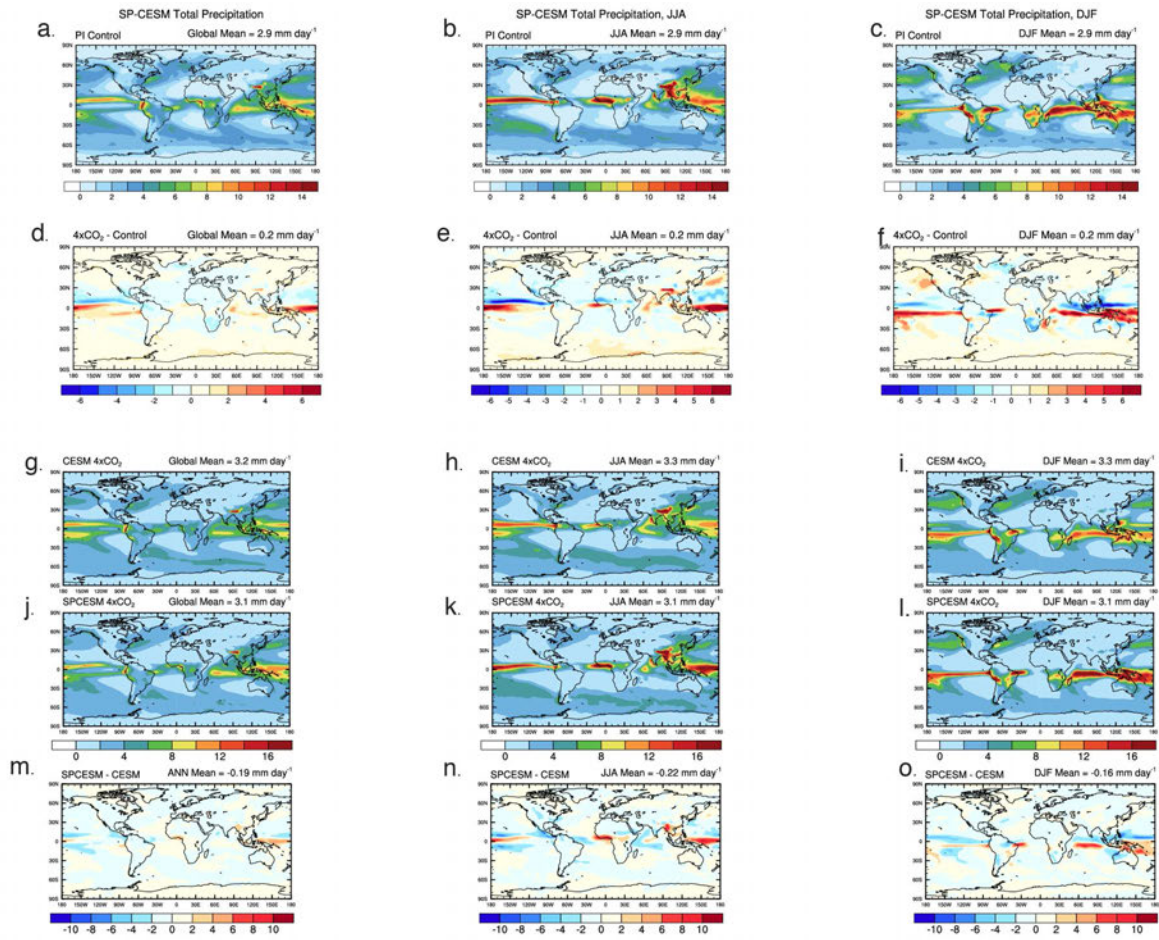


Figure 3.20. As in Figure 3.17, but for total precipitation.

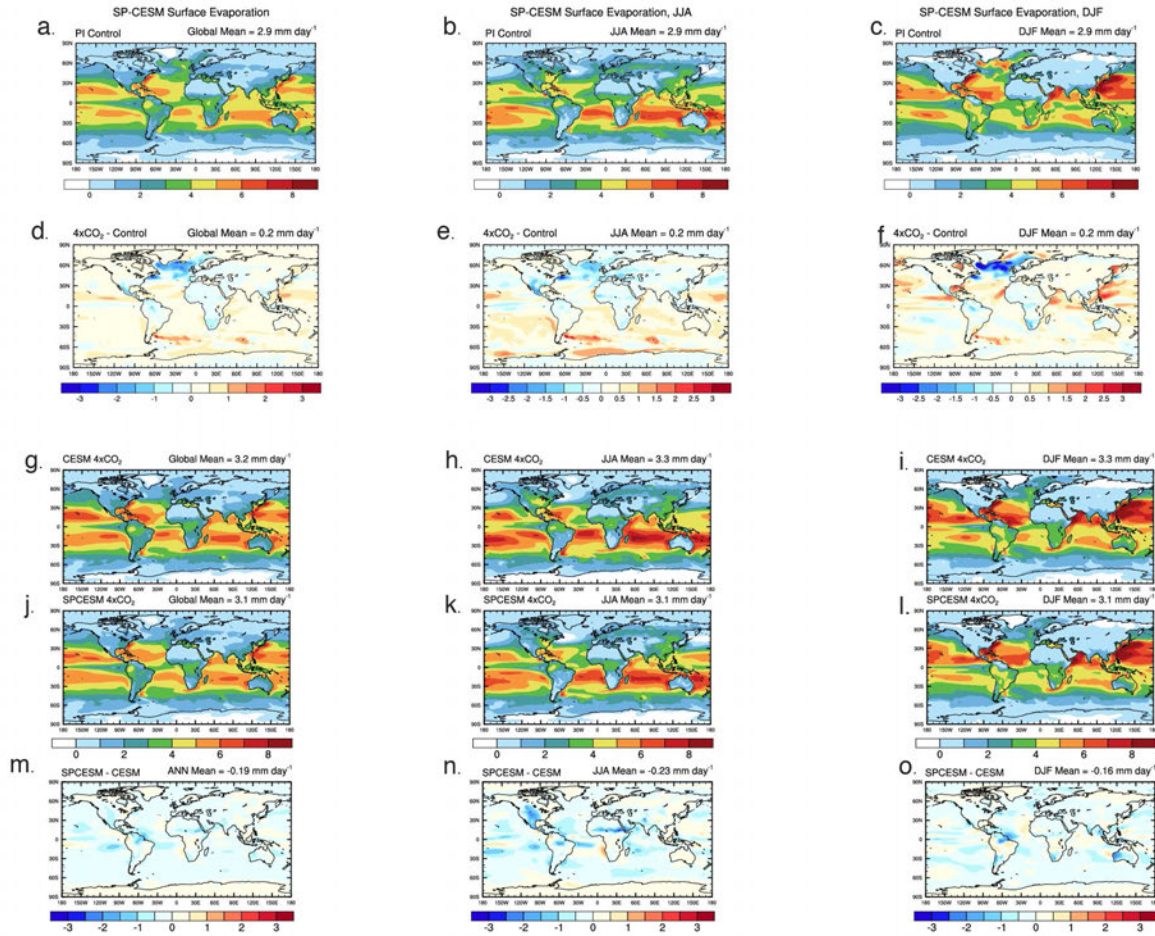


Figure 3.21. As in Figure 3.17, but for surface evaporation.

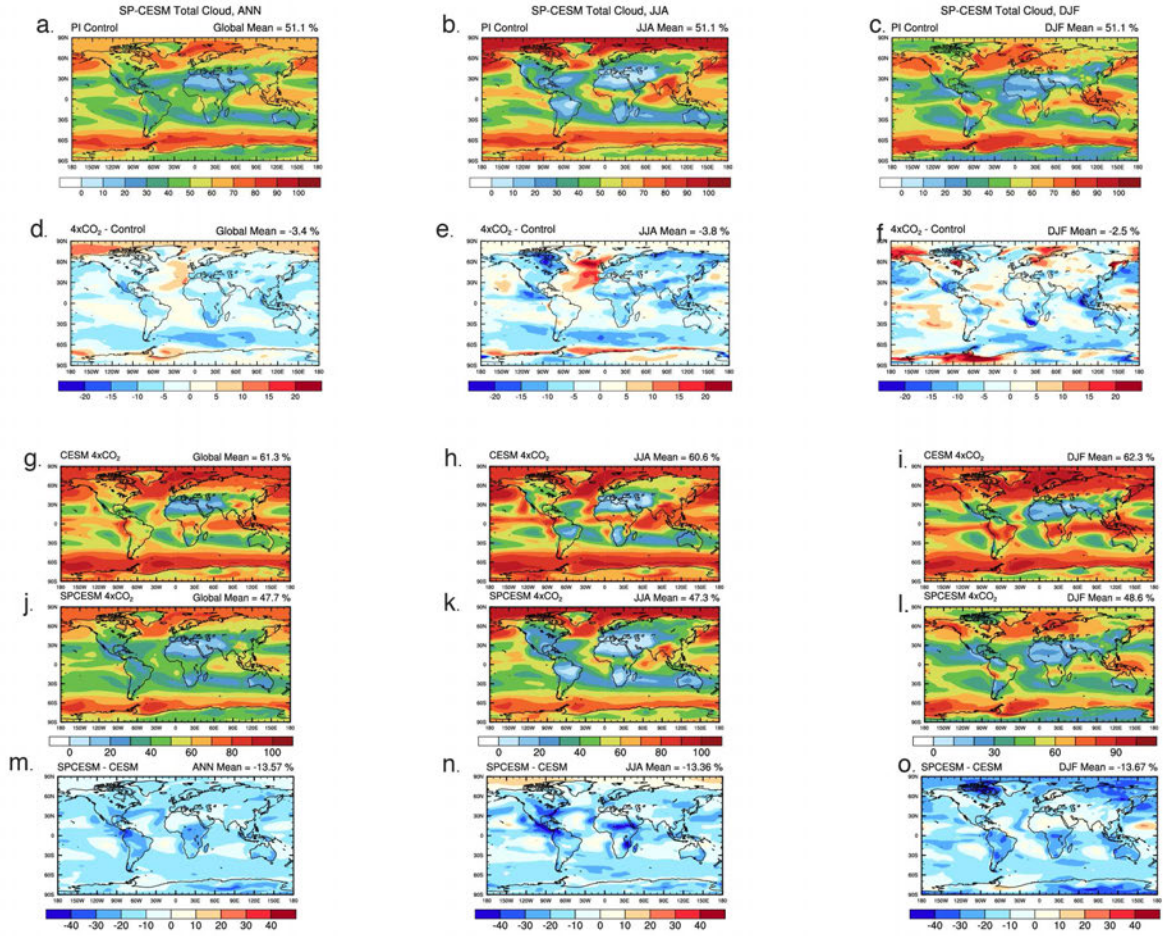


Figure 3.22. As in Figure 3.17, but for total cloud amount.

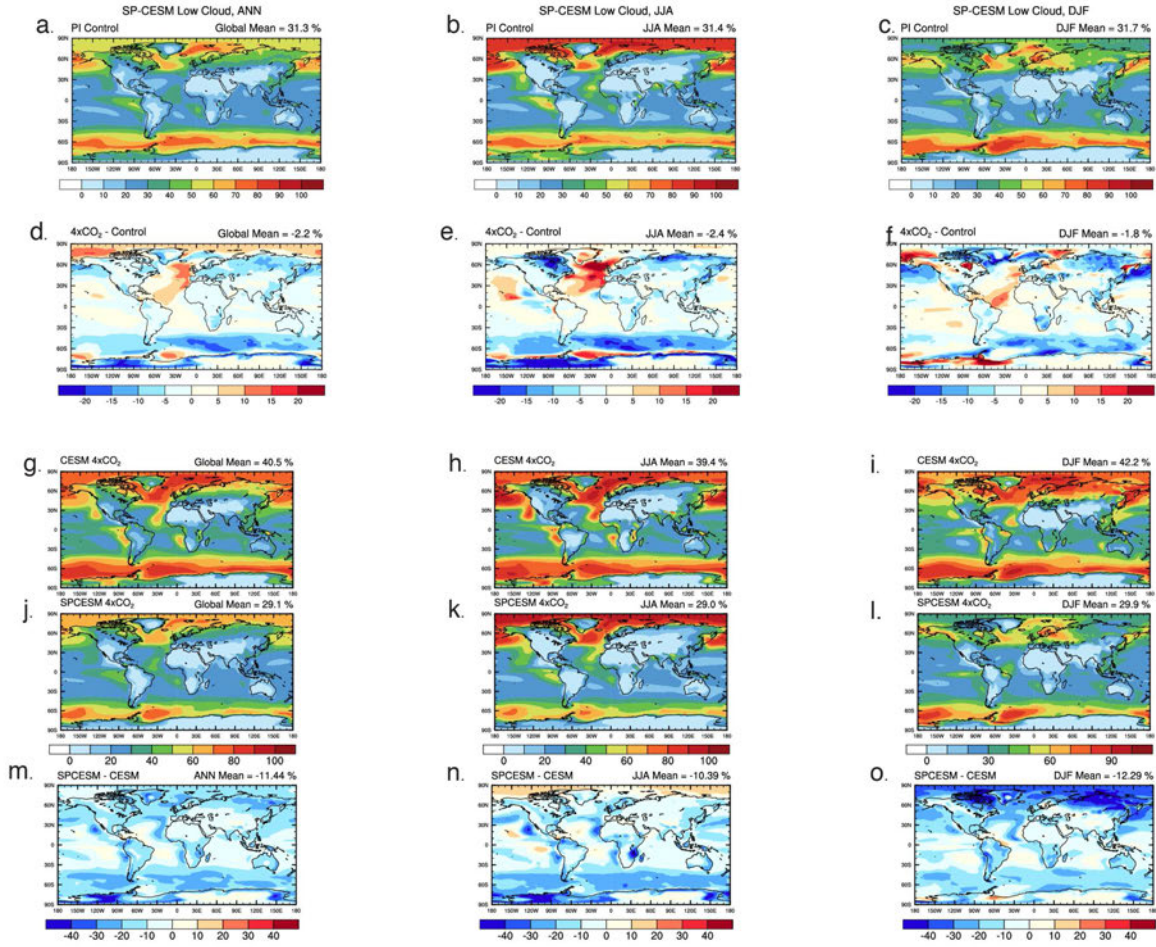


Figure 3.23. As in Figure 3.17, but for low cloud amount.

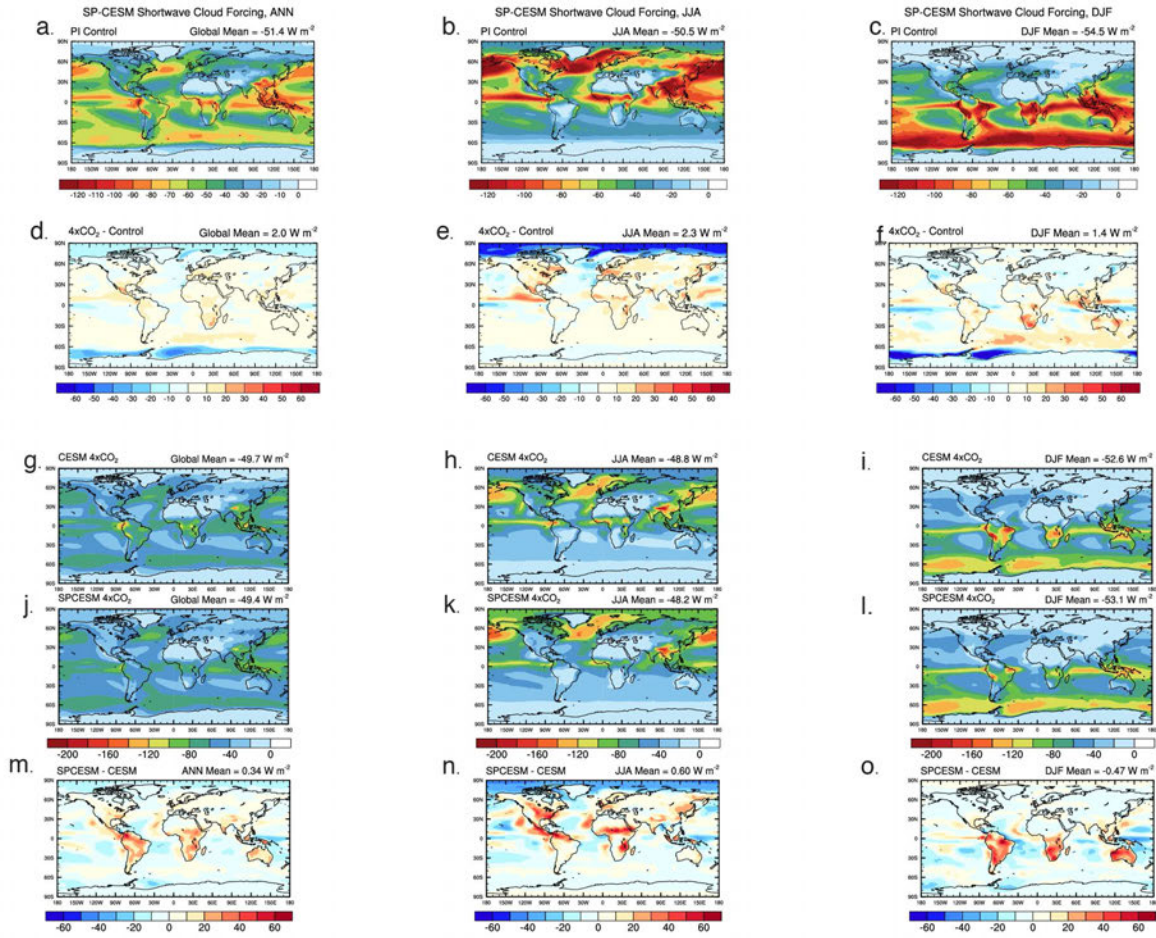


Figure 3.24. As in Figure 3.17, but for shortwave cloud forcing.

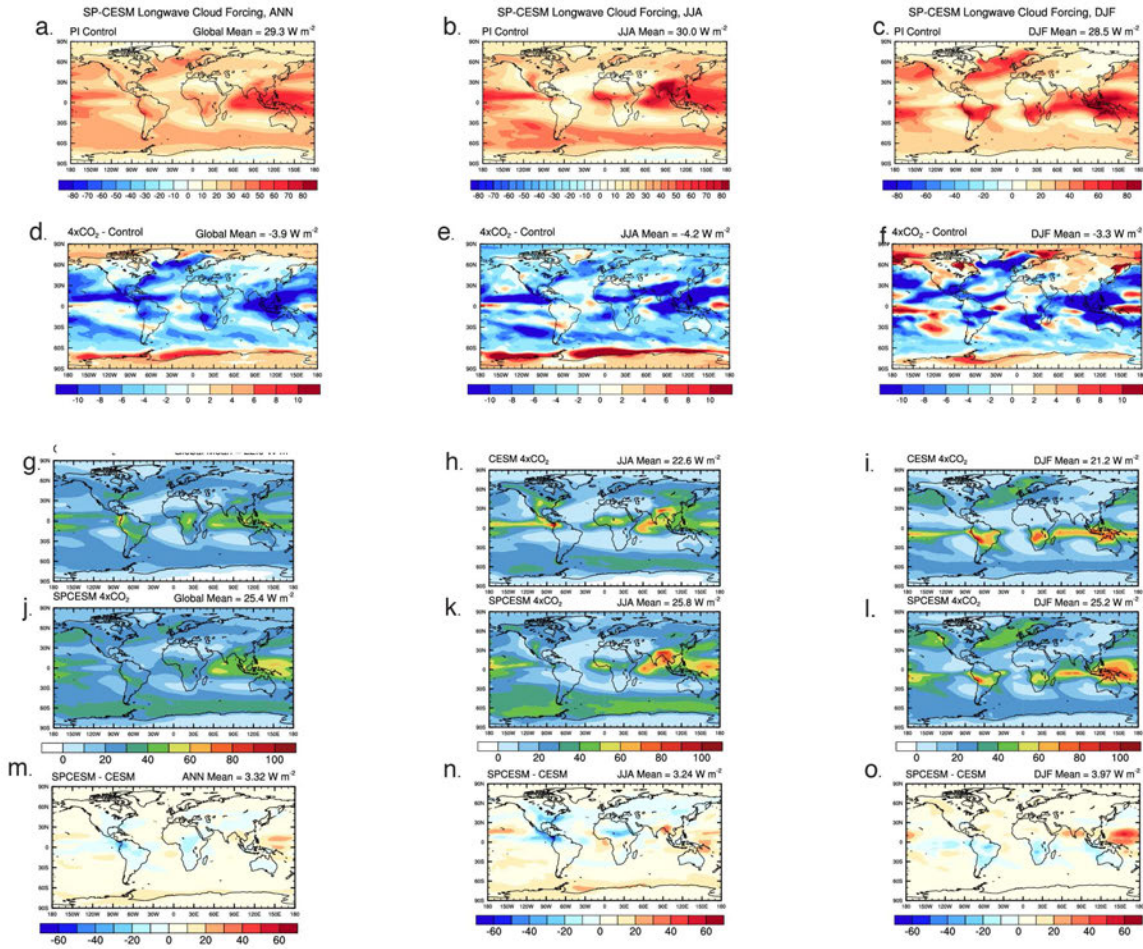


Figure 3.25. As in Figure 3.17, but for longwave cloud forcing.

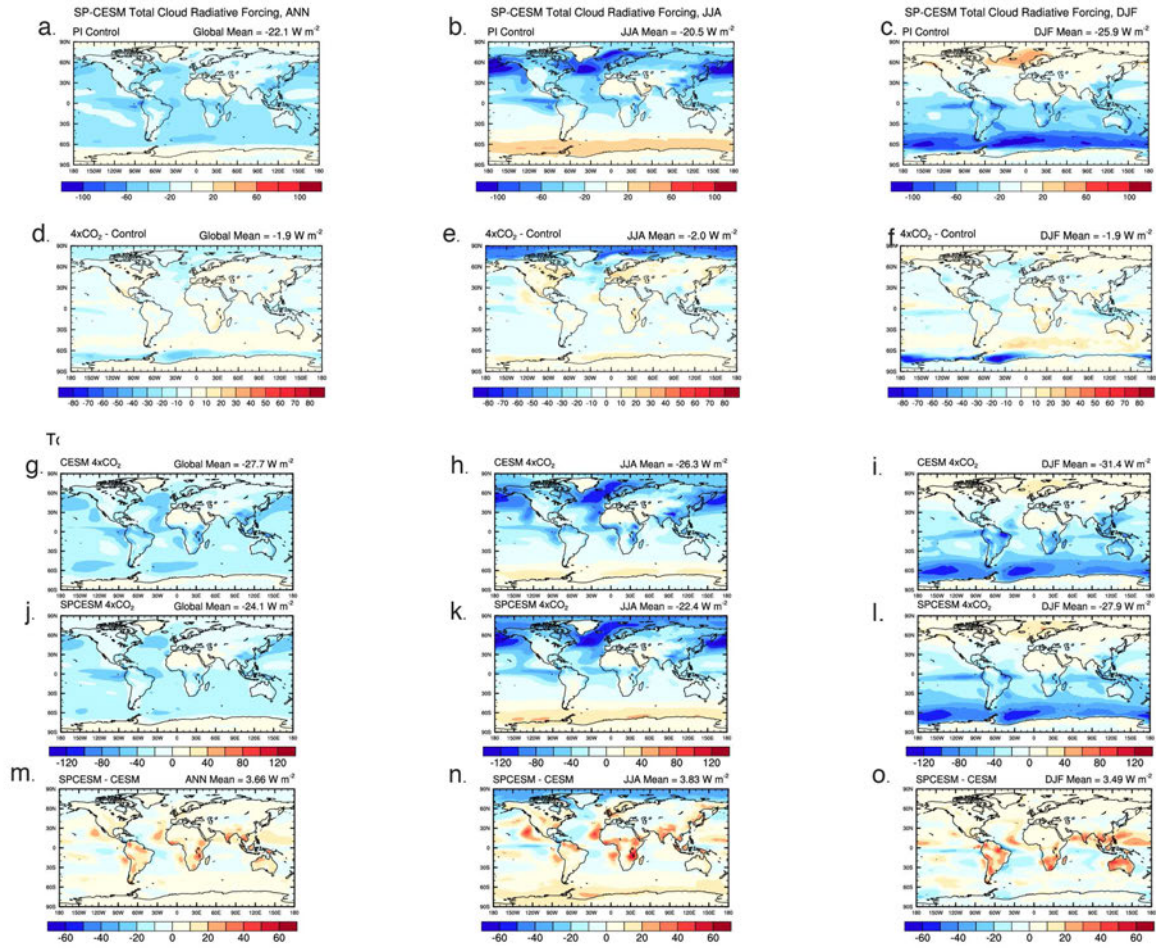


Figure 3.26. As in Figure 3.17, but for total cloud radiative forcing (SWCF plus LWCF).

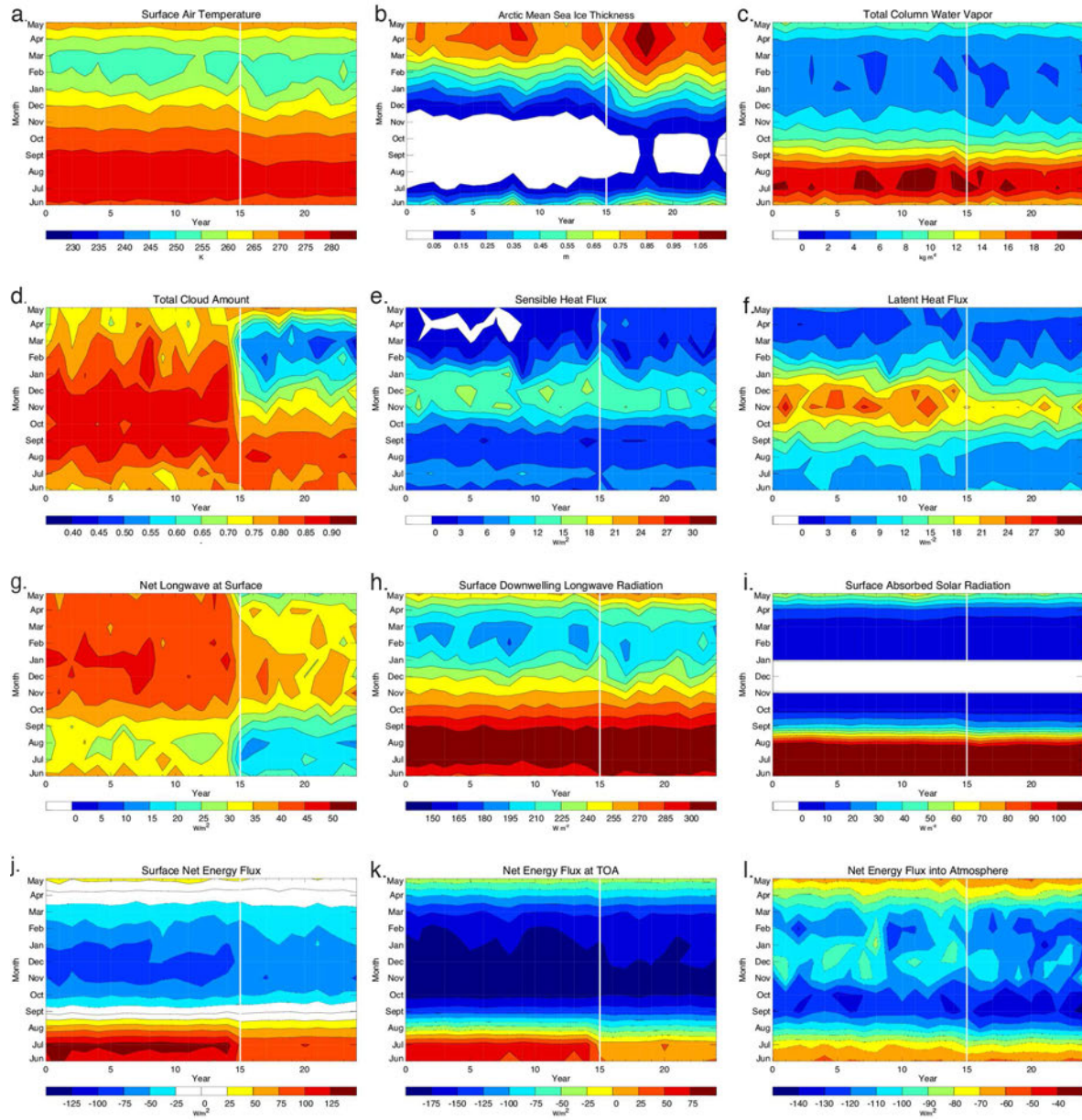


Figure 3.27. Arctic mean seasonal trend plots for the last 15 yrs of CESM 4xCO₂ and 10 years of SP-CESM 4xCO₂. The white line delineates the start of SP-CESM.

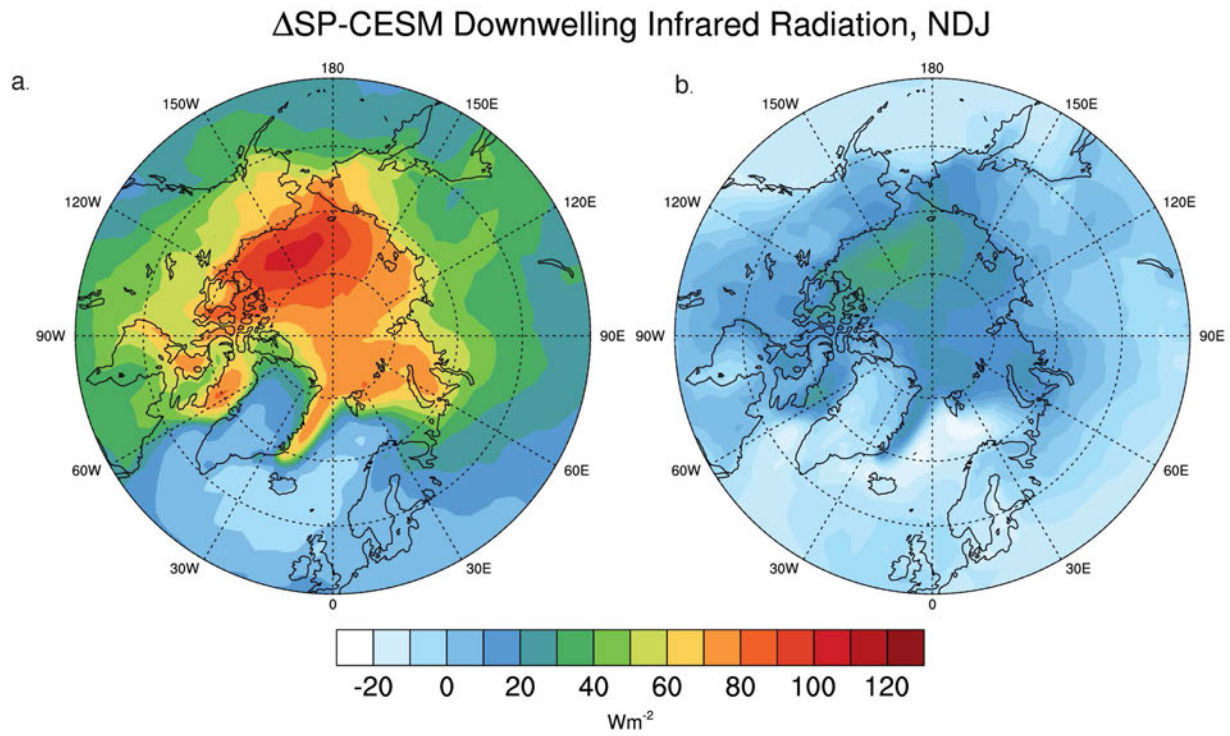


Figure 3.28. Polar stereographic map of change (4xCO₂ minus PI Control) in SP-CESM wintertime (November -December- January) a) downwelling longwave radiation and b) the contribution to a) from clouds.

SP-CESM Δ DLR, NDJ

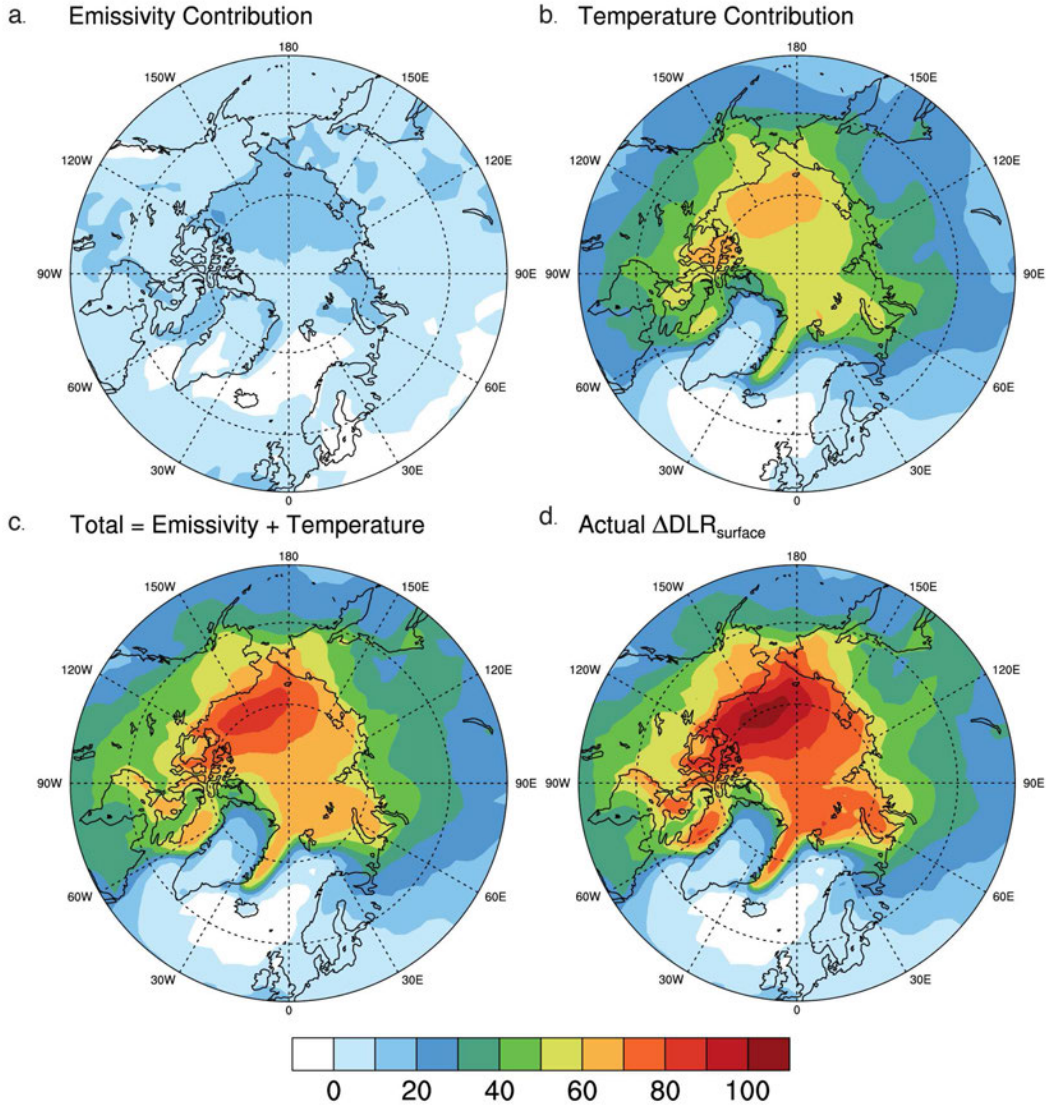


Figure 3.29. Polar stereographic maps of the wintertime contributions to $\Delta F_{\downarrow, sfc}$ from the changes in the a) the emissivity, and b) the temperature. The calculations are based on the linearization shown in Eq. (2.2). Panel c is the sum of a) and b). Panel d is the actual change in downwelling longwave radiation. The differences between panels c and d show the errors due to the linearization..

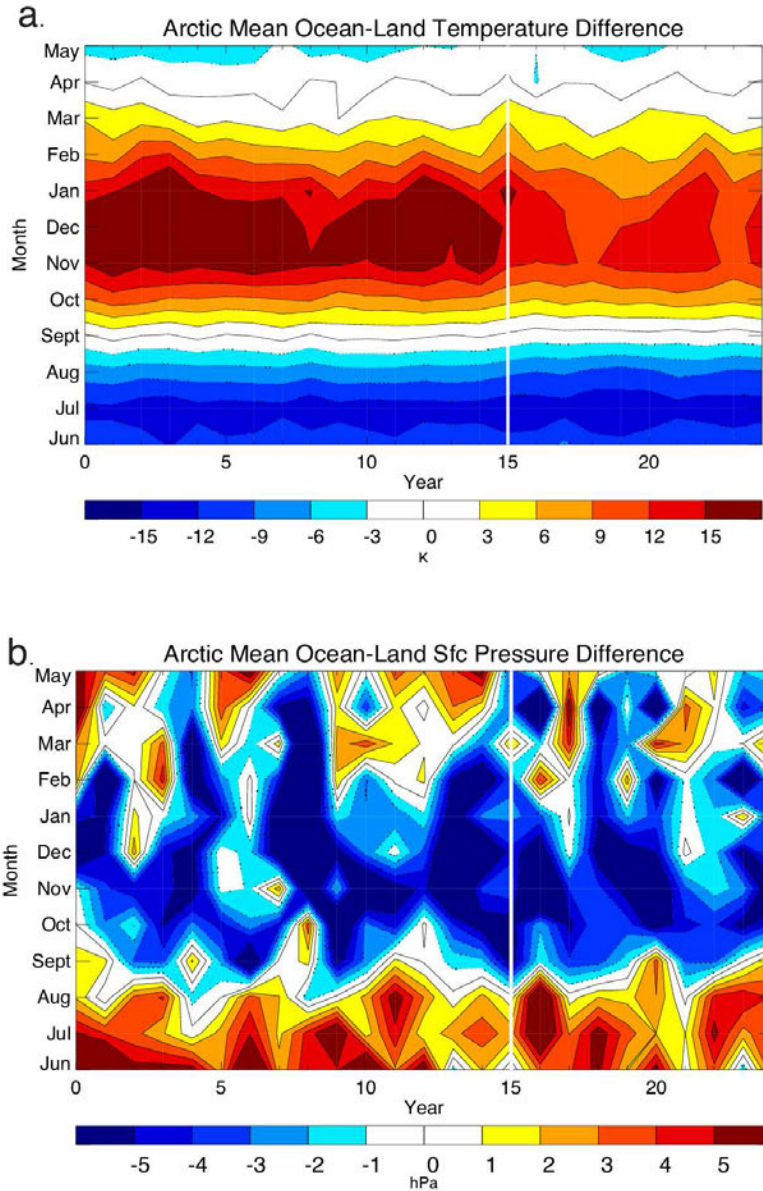
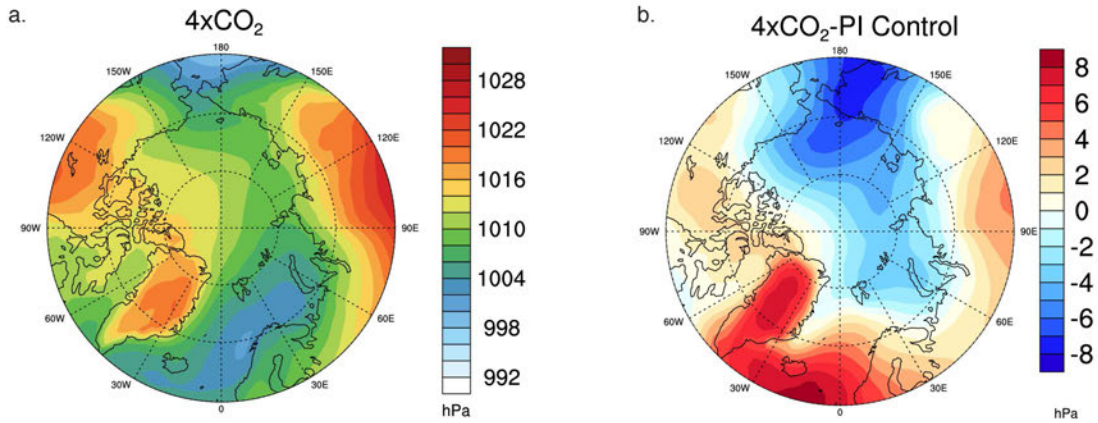


Figure 3.30. As in Figure 3.27, Panel a): The difference in surface air temperature between the Arctic Ocean (including areas covered by sea ice) and the surrounding land, from 60°N to the pole. Warmer colors indicate the ocean is warmer than the land and cooler colors indicate the land is warmer than the ocean. Panel b): As in panel a), but for the difference in surface pressure between the Arctic Ocean (including areas covered by sea ice) and the surrounding land, from 60°N to the pole.

Mean Sea Level Pressure, NDJ



970 hPa Winds and Surface Temperature, NDJ

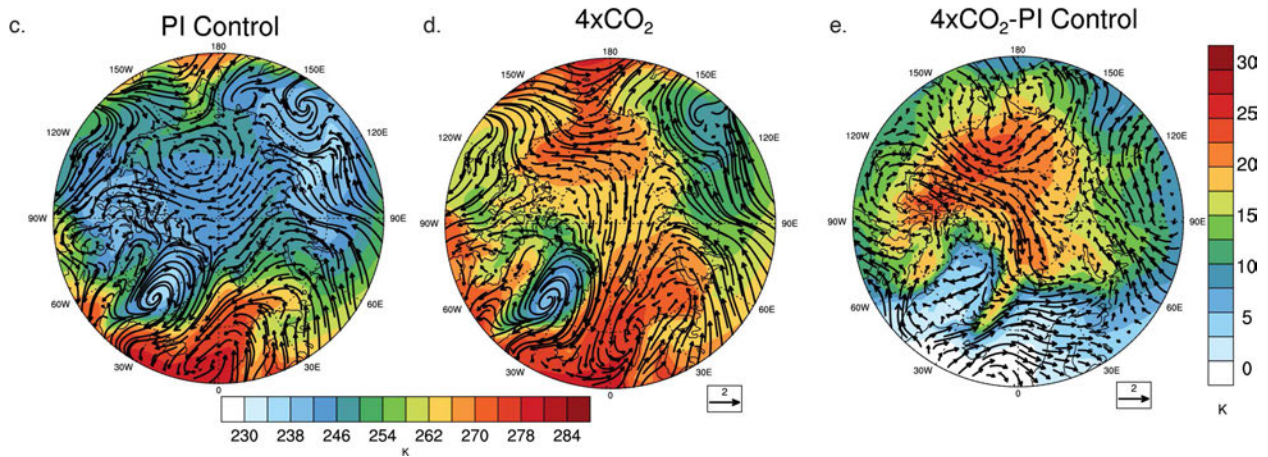


Figure 3.31. Panel a): Map showing the $4xCO_2$ SP-CESM-simulated wintertime sea level pressure and b) difference ($4xCO_2$ minus PI control). Panels c), d) and e) respectively show maps of the SP-CESM simulated wintertime 970 hPa winds (vectors) with overlaid on the surface temperature (filled contours) for PI Control, $4xCO_2$, and the difference.

Total Diabatic Heating, NDJ

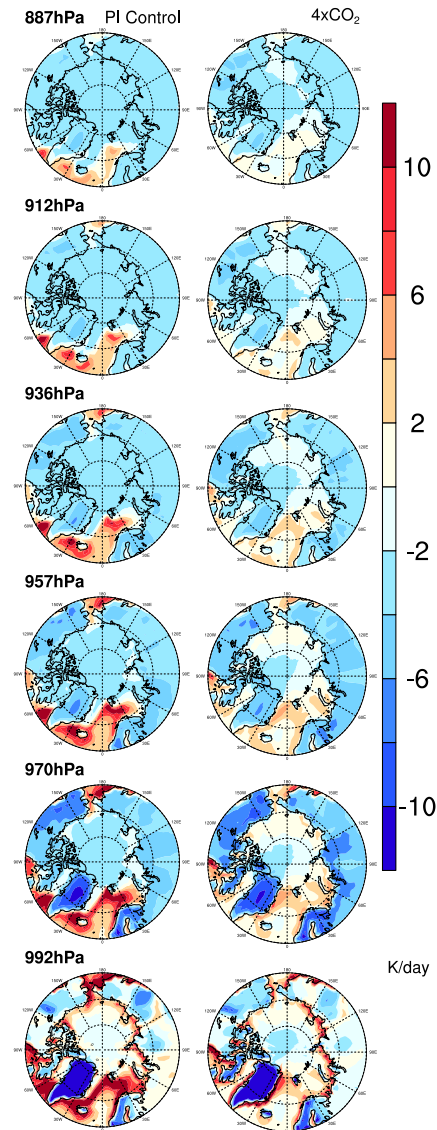


Figure 3.32. Maps of the SP-CESM simulated wintertime diabatic heating at several levels in the lower troposphere for both the PI control (left column) and 4xCO₂ (right column).

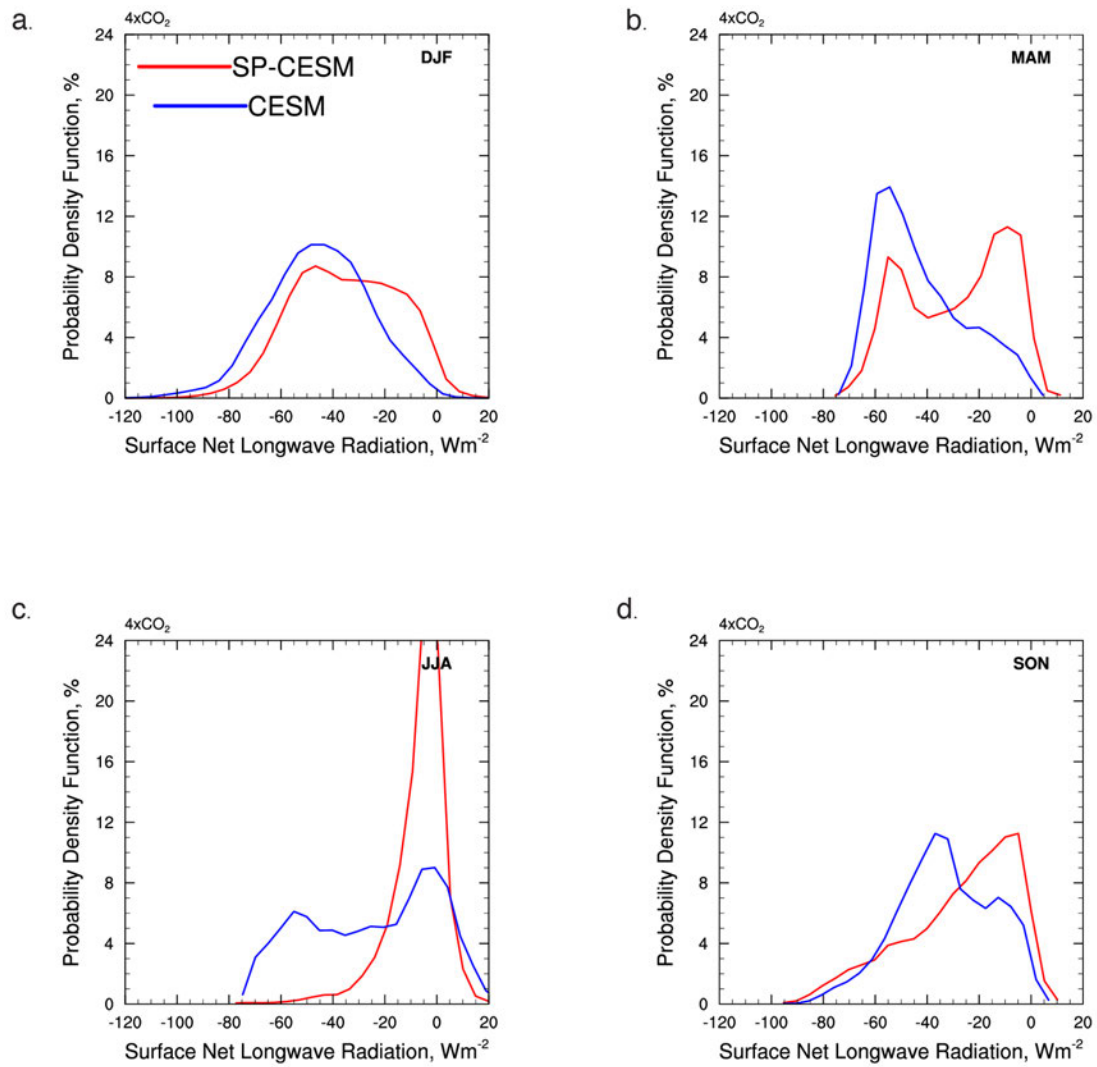


Figure 3.33. As in Figure 3.12, but for the 4xCO₂ climate.

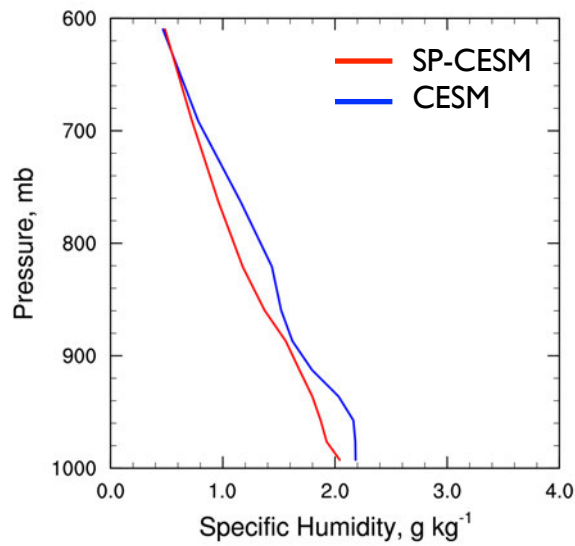
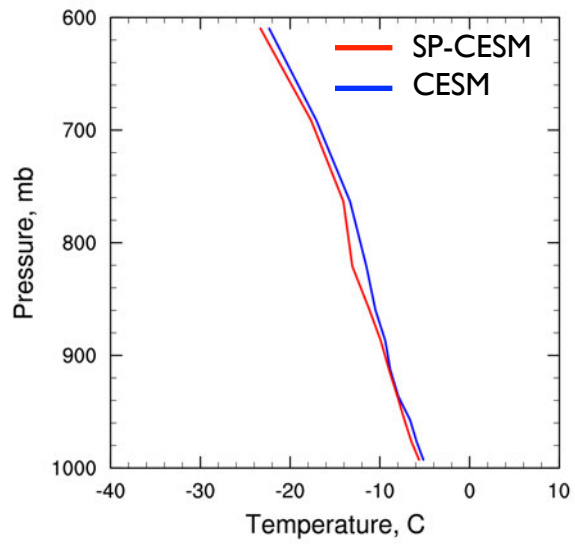


Figure 3.34. Simulated daily averaged vertical profiles of temperature (top) and specific humidity (bottom) for CESM (blue), and SP-CESM (red) for the radiatively clear state at 4xCO₂.

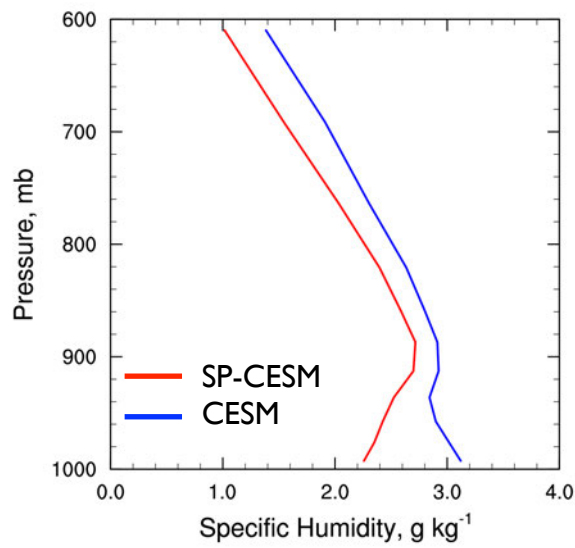
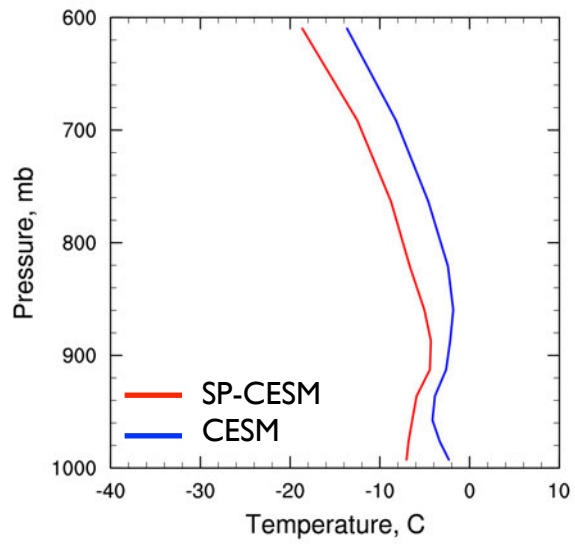


Figure 3.35. As in Figure 3.34 but for the opaquely cloudy state at 4xCO₂.

DJF 4xCO₂

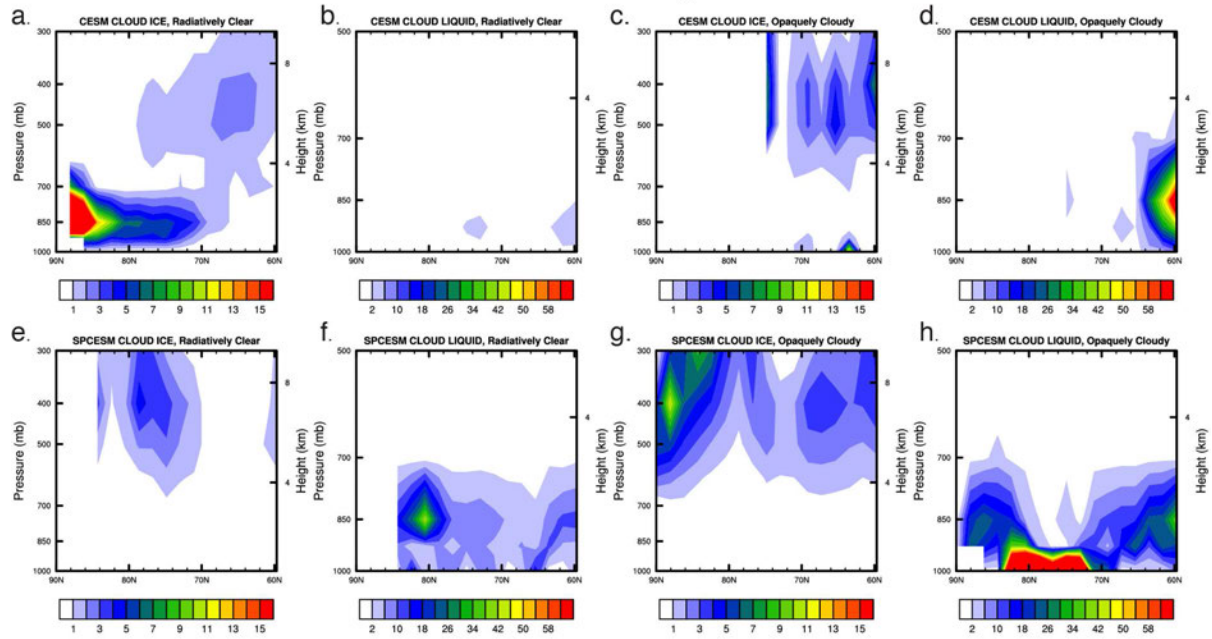


Figure 3.35. As in Figure 3.16, but for the 4xCO₂ climate.

CHAPTER 4: SUMMARY AND FUTURE WORK

4.1 SUMMARY

There is a need in the scientific community for improved simulations and, more importantly, improved understanding of the Arctic climate. As the climate continues to warm due to increasing greenhouse gas concentrations, we can expect the polar regions to undergo even more environmental change, from the complete loss of summer sea ice, to the melting of Greenland ice sheet. How will the role of clouds change as the Arctic climate continues to evolve?

This study has addressed the feedbacks that favor Arctic amplification during the dark-season; and how clouds interact with and influence the present-day and future surface energy budgets of the Arctic. We have also shown that the use of super-parameterization, embedding a 2D cloud resolving model in each atmospheric grid-box, improves the representation of the simulated Arctic climate.

As discussed in Chapter 2, we performed a transient climate change simulation with the Community Earth System Model, to investigate the impacts of dark-season surface radiative processes in CO₂-induced Arctic climate change. In this analysis, we identified two feedbacks that occur during the winter season. The first and stronger component involves the reduced insulating power of the sea ice, called the *ice-insulation feedback*, which is complementary to the well-known ice-albedo feedback. The ice-insulation feedback, whereby decreases in sea ice cover and thickness promote an increase in the downwelling longwave radiation, which then

leads to further decreases in sea ice cover and thickness. The positive ice-insulation feedback operates all year long, whereas the ice-albedo feedback only operates during the summer, and will end once summer sea-ice completely disappears. The fact that the ice-insulation feedback operates throughout the year, accounts for its power and importance of this feedback, especially during fall and winter.

The second and weaker feedback involves the changes in the dark-season winds, which are described in terms of a shallow winter monsoon that appears in the warmer climate but not in the present climate. In this newly-identified *Arctic Winter Monsoon*, there is low-level flow from the cold land to the warm ocean. Subsequently, dry air moves out over the ocean. We showed that the dry winds of a winter monsoon promote increased evaporation from the ocean. This increased evaporation is the main mechanism by which a winter monsoon promotes a moistening of the air over the ocean. In our simulation, we find that enhanced evaporation is partly due to more open water with warmer surface temperatures, and partly due to increased low-level wind speed.

The model-dependence of these findings was examined through an analysis of six climate models from the CMIP5 archive. As the simulated climate in the models adjust to the $4\times\text{CO}_2$ forcing, similarly to CESM, a strong temperature contrast developed between the Arctic Ocean and surrounding land during winter. As a result of the temperature contrast, sea level pressure decreased more over the Arctic Ocean. In addition to the shift towards lower wintertime Arctic surface pressure, the near-surface winds shifted, converging from the land to the ocean. As in CESM, increased evaporation during winter was the main mechanism by which the winter

monsoon promotes a moistening of the air over the ocean, and this feature was evident in a number of the CMIP5 models evaluated. With the limited number of models analyzed, we can say that the development of a winter monsoon is present in a handful of the CMIP5 models. An extensive multi-model analysis of the CMIP5 archive would be useful to fully understand and quantify the model-dependence of these results.

In Chapter 3, we showed how the incorporation of super-parameterization results in a more realistic representation of the Arctic climate. First, we explored the representation of the Arctic atmosphere in SP-CESM by evaluating surface temperature, sea level pressure, sea ice area, and sea ice thickness because of their significant implications on the regional and global climate. To highlight a few of these findings, we found that the distribution of sea ice thickness in SP-CESM was strikingly similar to the observations during March and September. Also, the location and strength of the Beaufort Sea High, one of the main drivers of sea ice advection throughout the Arctic, was captured reasonably well with SP-CESM as compared to observations. From the evaluation with several observational and reanalysis datasets, we found that SP-CESM tends to provide a more consistent and overall realistic representation of present-day Arctic climate compared to the conventional CESM.

The seasonal cycle of cloud amount and distribution in SP-CESM and CESM were examined and evaluated in Chapter 3. Both models generally overestimate (underestimate) cloud coverage over the ocean (land) compared to observations. The biases with SP-CESM are smaller than those of CESM. Broadly speaking, we found the clouds were simulated in the right place although the amount may be slightly overestimated or underestimated compared to observations.

We then, quantified net radiation biases at the TOA and surface to determine how the contribution of clouds influence these biases. There are a number of reasons for biases at the TOA and surfaces, but we ultimately found that insufficient cloud amount contribute to SW biases, while excessive middle and high clouds year-round contribute to LW biases.

A prominent feature of the Arctic climate, discovered during the SHEBA field campaign of 1997-1998, is the presence of two preferred and persistent winter states. We explored the distribution of these winter regimes in both models, compared to observations. We found that SP-CESM was able to better reproduce both of the preferred winter states, and this was mostly due to better representation of the microphysical properties of the clouds. An interesting finding in these simulations is that although the microphysical schemes of the two models are exactly the same, the simulated results are quite different. Is it really just a question of scales? If this is the case, what changes need to be made in CESM in order to have more realistic cloud processes without the inclusion of super-parameterization? SP-CESM calculates the microphysics on the CRM grid rather than the large-scale, and is consequently about 100 times more computationally expensive than the conventional CESM.

The causes are unclear as to why SP-CESM is able to better simulate these key features of the Arctic climate, but we think it may be due to improved simulations of tropical convection. Further investigations are needed but are beyond the scope of this study.

4.2 FUTURE WORK

This study has addressed the importance of downwelling longwave radiation in Arctic amplification, and its associated feedbacks. It would be interesting to delve deeper into the atmospheric processes that make up the ice-insulation feedback. One approach would be to decompose the ice-insulation feedback and quantify the importance of the individual processes at hand. One way to tackle this would be to quantify the contributions of various atmospheric components (e.g. water vapor, clouds, CO₂) to the downwelling longwave radiation response in the climate model by conducting a decomposition analysis (e.g. the Coupled Feedback Response Analysis Method, CFRAM). The Coupled Feedback Response Analysis Method (CFRAM; Lu and Cai 2009; Cai and Lu 2009), was originally formulated to diagnose the temperature response to global warming but since then, has been applied to diagnose Arctic warming. CFRAM is based on the energy balance equation of the coupled atmosphere–surface system, similar to the partial radiative perturbation (Wetherald and Manabe 1988) and the radiative kernel method (Soden and Held 2006), but has been shown to be particularly useful when there is a decoupling between the TOA and surface radiative response. CFRAM also considers both radiative and non-radiative feedback processes explicitly. Given the differences between the CESM and SP-CESM simulations, an analysis based on decomposing the ice-insulation feedback into cloud and water vapor components may be an interesting research avenue to pursue.

To look more closely at sea ice processes, it would be interesting, although computationally expensive, to include the sea-ice model in super-parameterization (SP-SEAICE). I can envision running the atmosphere and sea ice models with super-parameterization

to address the subgrid-scale processes at the sea ice surface that are typically parameterized. Many of the thermodynamic processes that control melting, freezing, and dissolving of the sea ice cover are either parameterized or not included. As an example, the sea ice model used in this study (CICE), includes a simple melt-pond parameterization that simulates the pond volume and area as functions of the surface meltwater flux. If we incorporated super-parameterization at the sea ice scale in the model, at least some of the melt-ponds could be explicitly resolved. Melt ponds are more prominent and have a stronger influence on the radiation budget during the summer and fall. As the climate continues to change, and the sea ice growth season is pushed back further into the fall, the radiative effects of melt ponds could become important in the early winter and potentially influence the ice-insulation feedback.

Modeling of snow on sea ice is also an area of interest, and it has received less research attention in the sea ice community compared to sea ice area and thickness. Snow cover acts to insulate sea ice, inhibiting its growth, and to delay ice melt onset, thereby decreasing surface melt. As a result, changing snow conditions can strongly modify the response of sea ice. As the climate continues to warm and the sea ice gets thinner, the insulating effect of the snow on the sea ice will become increasingly more important. By implementing, SP-SEAICE, we could explore this more and gain a better understanding of the relative importance of key snow characteristics for climate feedbacks including the ice-insulation feedback.

In Chapter 3, we discussed the influence of clouds and their microphysical properties on the Arctic climate. The Morrison and Gettelman (2008) two-moment microphysics scheme gives a better representation of cloud processes compared to earlier parameterizations. It would be

interesting to address the role of ice nucleation in the simulated Arctic clouds. Previous work has shown that ice nucleation processes have a strong impact on simulated Arctic clouds (Liu et al., 2007a,b; Xie et al., 2008; Gettelman et al., 2010; Morrison et al., 2012; Xie et al., 2013), and ice nuclei (IN) play an important role in the glaciation of mixed-phase clouds. Although the modeling community accepts and understands the importance of ice formation in clouds, the treatment of IN concentrations in current climate models is still crude or non-existent due to our poor understanding of the complex ice-formation processes and a general lack of observations of cold clouds. Existing ice nucleation schemes have been developed based on very limited field studies (most conducted at middle and low latitudes) and optimized specifically for where these measurements were observed. Currently, CESM and SP-CESM use the ice nucleation scheme of Gettelman et al., (2010) which is based on the scheme developed by Liu et al., (2007a) and also includes the widely used empirical formulation developed by Meyers et al., (1992, hereafter M1992). In M1992, the IN predicted through deposition and condensation freezing are parameterized as functions of ice supersaturation, based on measurements at northern midlatitudes. Prenni et al., (2007) found that the M1992 parameterization is not representative of average IN behavior of Arctic clouds encountered during M-PACE (The Mixed-Phase Arctic Cloud Experiment) field experiment flights. To best fit M-PACE observations of IN, a modified M1992 parameterization was proposed by Prenni et al., (2007), which results in a much smaller ice number density. Based on in situ data measured by continuous-flow diffusion-chamber (CFDC) measurements from nine field campaigns conducted in many regions of the globe, DeMott et al., (2010) showed a large variability in IN observations in time, space, and temperature. At any temperature the IN number concentrations have been observed to span more

than three orders of magnitude. It would be interesting to explore the inclusion of Prenni et al., (2007) and/or DeMott et al., (2010) in the fully coupled SP-CESM, to examine the role of ice nuclei in the simulated clouds and the impact on the Arctic winter regimes.

In closing, the work in this dissertation has led to more questions that I would like to answer. I hope to continue my work on understanding the sensitivity of Arctic sea ice to the changing climate, and the role of clouds.

REFERENCES

- Abbot, D. S., and E. Tziperman, 2008a: A high-latitude convective cloud feedback and equable climates. *Quart. J. Roy. Meteor. Soc.*, **134**, 165–185, doi: 10.1002/qj.211.
- Abbot, D. S., and E. Tziperman, 2008b: Sea ice, high-latitude convection, and equable climates. *Geophys. Res. Lett.*, **35**, L03702, doi:10.1029/2007GL032286.
- Abbot, D. S., M. Huber, G. Bousquet, and C. Walker, 2009: High-CO₂ cloud radiative forcing feedback over both land and ocean in a global climate model. *Geophys. Res. Lett.*, **36**, L05702. doi:10.1029/2008GL036703.
- ACIA, 2005: Arctic Climate Impacts Assessment. Cambridge University Press, 1042p.
- Arnold, N., M. Branson, M. A. Burt, D. S. Abbot, Z. Kuang, D. A. Randall, and E. Tziperman, 2014: Significant consequences of explicit representation of atmospheric convection at high CO₂ concentration. *Proc. Nat. Acad. Sci.*, **111**, 10943–10948. doi: 10.1073/pnas.1407175111.
- Barton, N. P., S. A. Klein, J. S. Boyle, and Y. Y. Zhang, 2012: Arctic synoptic regimes: Comparing domain-wide Arctic cloud observations with CAM4 and CAM5 during similar dynamics. *J. Geophys. Res.*, **117**, D15205, doi:10.1029/2012JD017589.
- Benedict, J. J., and D. A. Randall, 2009: Structure of the Madden–Julian Oscillation in the superparameterized CAM. *J. Atmos. Sci.*, **66**, 3277–3296, doi:10.1175/2009JAS3030.1.
- Benedict, J. J., and D. A. Randall, 2011: Impacts of idealized air-sea coupling on Madden-Julian Oscillation structure in the super-parameterized CAM. *J. Atmos. Sci.*, **68**, 1990–2008, doi: <http://dx.doi.org/10.1175/JAS-D-11-04.1>.
- Bengtsson, L., K. I. Hodges, S. Koumoutsaris, M. Zahn, and N. Keenlyside, 2011: The changing atmospheric water cycle in polar regions in a warmer climate. *Tellus*, **63A**, 907–920, doi: 10.1111/j.1600-0870.2011.00534.x.
- Bergeron, T., 1935: Procès Verbaux de l'Association de Meteorologie, edited by P. Duport, pp. 156–178, *Int. Union of Geod. and Geophys.*, Karlsruhe, Germany.
- Betts, A. K., 1998: Climate–convection feedbacks: Some further issues. *Climatic Change*, **39**, 35–38, doi: 10.1023/A:1005323805826.
- Bindoff, N. L., P. A. Stott, K. M. AchutaRao, M. R. Allen, N. Gillett, D. Gutzler, K. Hansingo, G. Hegerl, Y. Hu, S. Jain, I. I. Mokhov, J. Overland, J. Perlwitz, R. Sebbari, and X. Zhang, 2013:

Detection and attribution of climate change: from global to regional. In: *Climate Change 2013: The Physical Science Basis. Contribution of Working Group I to the Fifth Assessment Report of the Intergovernmental Panel on Climate Change* [Stocker, T.F., D. Qin, G.-K. Plattner, M. Tignor, S.K. Allen, J. Boschung, A. Nauels, Y. Xia, V. Bex and P.M. Midgley (eds.)]. Cambridge University Press, Cambridge, United Kingdom and New York, NY, USA.

Bintanja, R., and F. M. Selten, 2014: Future increases in Arctic precipitation linked to local evaporation and sea ice retreat. *Nature*, **509**, 479-482 doi:10.1038/nature13259.

Bitz, C. M., and W. H. Lipscomb, 1999: An energy-conserving thermodynamic model of sea ice. *J. Geophys. Res.*, **104**, 7, 669-15, 677, doi: 10.1029/1999JC900100.

Boucher, O., D. Randall, P. Artaxo, C. Bretherton, G. Feingold, P. Forster, V.-M. Kerminen, Y. Kondo, H. Liao, U. Lohmann, P. Rasch, S. K. Satheesh, S. Sherwood, B. Stevens, and X.Y. Zhang, 2013: Clouds and Aerosols. In: *Climate Change 2013: The Physical Science Basis. Contribution of Working Group I to the Fifth Assessment Report of the Intergovernmental Panel on Climate Change* [Stocker, T.F., D. Qin, G.-K. Plattner, M. Tignor, S.K. Allen, J. Boschung, A. Nauels, Y. Xia, V. Bex and P.M. Midgley (eds.)]. Cambridge University Press, Cambridge, United Kingdom and New York, NY, USA.

Burt, M. A., D. A. Randall, and M. D. Branson, 2016: Dark warming, *J. Climate*, **29**, 705–719. doi: <http://dx.doi.org/10.1175/JCLI-D-15-0147.1>

Cai, M., and J. Lu, 2009: A new framework for isolating individual feedback processes in coupled general circulation climate models. Part II: Method demonstrations and comparisons. *Climate Dyn.*, **32**, 887–900, doi:10.1007/s00382-008-0424-4.

Cesana, G., and H. Chepfer, 2012: How well do climate models simulate cloud vertical structure? A comparison between CALIPSO-GOCCP satellite observations and CMIP5 models. *Geophys. Res. Lett.*, **39**, L20803, doi:10.1029/2012GL053153.

Chepfer, H., S. Bony, D. M. Winker, M. Chiriaco, J.-L. Dufresne, and G. Sèze, 2008: Use of CALIPSO lidar observations to evaluate the cloudiness simulated by a climate model. *Geophys. Res. Lett.*, **35**, L15704, doi:10.1029/2008GL034207.

Comiso, J., 2008: Bootstrap sea ice concentrations from NIMBUS-7 SMMR and DMSP SSM/I, 1979–2007. National Snow and Ice Data Center, Boulder, CO, digital media.

Curry, J. A., and E. E. Ebert, 1992: Annual cycle of radiative fluxes over the Arctic ocean: Sensitivity to cloud optical properties. *J. Climate*, **5**, 1267-1280, doi: [http://dx.doi.org/10.1175/1520-0442\(1992\)005<1267:ACORFO>2.0.CO;2](http://dx.doi.org/10.1175/1520-0442(1992)005<1267:ACORFO>2.0.CO;2).

Curry, J. A., W. B. Rossow, D. A. Randall, and J. L. Schramm, 1996: Overview of Arctic cloud and radiation characteristics. *J. Climate*, **9**, 1731-1764, doi: [http://dx.doi.org/10.1175/1520-0442\(1996\)009<1731:OOACAR>2.0.CO;2](http://dx.doi.org/10.1175/1520-0442(1996)009<1731:OOACAR>2.0.CO;2).

Dee, D. P., S.M. Uppala, A. J. Simmons, P. Berrisford, P. Poli, S. Kobayashi, U. Andrae, M. A. Balmaseda, G. Balsamo, P. Bauer, P. Bechtold, A. C. M. Beljaars, L. van de Berg, J. Bidlot, N. Bormann, C. Delsol, R. Dragani, M. Fuentes, A. J. Geer, L. Haimberger, S. B. Healy, H. Hersbach, E. V. Hólm, L. Isaksen, P. Kållberg, M. Köhler, M. Matricardi, A. P. McNally, B. M. Monge-Sanz, J.-J. Morcrette, B.-K. Park, C. Peubey, P. de Rosnay, C. Tavolato, J.-N. Thépaut, and F. Vitart, 2011: The ERA-Interim reanalysis: configuration and performance of the data assimilation system. *Q.J.R. Meteorol. Soc.*, **137**: 553–597. doi: 10.1002/qj.828.

DeMott, C. A., and D. A. Randall, 2007: Convective precipitation variability as a tool for general circulation model analysis. *J. Climate*, **20**, 91-112.

DeMott, C. A., C. Stan, D. A. Randall, J. L. Kinter III, and M. Khairoutdinov, 2011: The Asian monsoon in the super- parameterized CCSM and its relationship to tropical wave activity. *J. Climate*, **24**, 5134–5156, doi:10.1175/2011JCLI4202.1.

DeMott, C. A., C. Stan, and D. A. Randall, 2013: Northward propagation mechanisms of the boreal summer intraseasonal oscillation in the ERA-Interim and SP-CCSM. *J. Climate*, **26**, 1973–1992, doi:10.1175/JCLI-D-12-00191.1.

DeMott, P. J., A. J. Prenni, X. Liu, S. M. Kreidenweis, M. D. Petters, C. H. Twohy, M. S. Richardson, T. Eidhammer, and D. C. Rogers, 2010: Predicting global atmospheric ice nuclei distributions and their impacts on climate, *Proc. Natl. Acad. Sci.*, **107**, 11217–11222, doi: 10.1073/pnas.0910818107.

Deser, C., R. Tomas, M. Alexander, and D. Lawrence, 2010: The seasonal atmospheric response to projected Arctic sea ice loss in the late twenty-first century. *J. Climate*, **23**, 333–351, doi: 10.1175/2009JCLI3053.1.

DeWeaver, E., and C. M. Bitz, 2006: Atmospheric circulation and Arctic sea ice in CCSM3 at medium and high resolution, *J. Climate*. **19**, 11, 2415–2436, doi: <http://dx.doi.org/10.1175/JCLI3753.1>.

Di Biagio, C. ,A. di Sarra, P. Eriksen, S. E. Ascanius, G. Mascara, and B. Holben, 2012: Effect of surface albedo, water vapour, and atmospheric aerosols on the cloud-free shortwave radiative budget in the Arctic, *Climate Dyn*, **39**, 3-4, 953, doi: 10.1007/s00382-011-1280-1.

Doyle, J. G., G. Lesins, C. P. Thackray, C. Perro, G. J. Nott, T. J. Duck, R. Damoah, and J. R. Drummond, 2011: Water vapor intrusions into the high Arctic during winter, *Geophys. Res. Lett.*, **38**, L12806, doi:10.1029/2011GL047493.

- Druckenmiller, M. L., H. Eicken, J. C. George, and L. Brower, 2013: Trails to the whale: reflections of change and choice on an Iñupiat icescape at Barrow, Alaska. *Polar Geography*, **36** (1-2), 5–29, doi: 10.1080/1088937X.2012.724459. 2.
- Eicken, H., 2013: Ocean science: Arctic sea ice needs better forecasts. *Nature*, **497** (7450), 431–433. 2.
- Eisenman, I., N. Untersteiner, and J. S. Wettlaufer, 2007: On the reliability of simulated Arctic sea ice in global climate models, *Geophys. Res. Lett.*, **34**, L10501, doi:10.1029/2007GL029914.
- English, J. M., J. E. Kay, A. Gettelman, X. Liu, Y. Wang, Y. Zhang, and H. Chepfer, 2014: Contributions of clouds, surface albedos, and mixed-phase ice nucleation schemes to Arctic radiation biases in CAM5. *J. Climate*, **27**, 5174–5197, doi:10.1175/JCLI-D-13-00608.1.
- Findeisen, W., 1938: Kolloid-Meteorologische, 2nd ed., *Am. Meteorol. Soc.*, Boston, Mass.
- Flato, G., J. Marotzke, B. Abiodun, P. Braconnot, S.C. Chou, W. Collins, P. Cox, F. Driouech, S. Emori, V. Eyring, C. Forest, P. Gleckler, E. Guilyardi, C. Jakob, V. Kattsov, C. Reason and M. Rummukainen, 2013: Evaluation of Climate Models. In: *Climate Change 2013: The Physical Science Basis. Contribution of Working Group I to the Fifth Assessment Report of the Intergovernmental Panel on Climate Change* [Stocker, T.F., D. Qin, G.-K. Plattner, M. Tignor, S.K. Allen, J. Boschung, A. Nauels, Y. Xia, V. Bex and P.M. Midgley (eds.)]. Cambridge University Press, Cambridge, United Kingdom and New York, NY, USA.
- Francis, J. A., and E. Hunter, 2007: Changes in the fabric of the Arctic’s greenhouse blanket. *Environ. Res. Lett.*, **2**, 045011, doi:10.1088/1748-9326/2/4/045011.
- Francis, J.A, J. R. Key, and X. Wang, 2005: Clues to variability in Arctic minimum sea ice extent. *Geophys. Res. Lett.*, **32**, L21501.
- Francis, J. A., W. Chan, D. J. Leathers, J. R. Miller, and D. E. Veron, 2009: Winter Northern Hemisphere weather patterns remember summer Arctic sea-ice extent. *Geophys. Res. Lett.*, **36** (7), L07 503, 1944– 8007, doi:10.1029/2009GL037274.1.
- Gettelman, A., H. Morrison, and S. J. Ghan, 2008: A new two-moment bulk stratiform cloud microphysics scheme in the NCAR community atmosphere model (CAM3). Part II: Single-column and global results. *J. Climate*, **21**, 3660–3679, doi:10.1175/2008JCLI2116.1.
- Gettelman, A., X. Liu, S. J. Ghan, H. Morrison, S. Park, and A. J. Conley, 2010: Global simulations of ice nucleation and ice supersaturation with an improved cloud scheme in the Community Atmospheric Model. *J. Geophys. Res.*, **115**, D18216, doi:10.1029/2009JD013797.

Ghatak, D., and J. Miller, 2013: Implications for Arctic amplification of changes in the strength of the water vapor feedback. *J. Geophys. Res.*, **118**, 7569–7578, doi: 10.1002/jgrd.50578.

Gorodetskaya, I. V. and L. B. Tremblay, 2008: Arctic cloud properties and radiative forcing from observations and their role in sea ice decline predicted by the NCAR CCSM3 model during the 21st century. Arctic Sea Ice Decline: Observations, Projections, Mechanisms, and Implications, *Geophys. Monogr.*, **180**, Amer. Geophys. Union, 213–268.

Graversen, R. G., Langen, P. G., and T. Mauritsen, 2014: Arctic amplification in CCSM4: contributions from the lapse rate and surface albedo feedbacks. *J. Climate*, **27**, 4433–4450, doi: <http://dx.doi.org/10.1175/JCLI-D-13-00551.1>

Graversen, R. G., and M. Wang, 2009: Arctic amplification in a coupled climate model with locked albedo. *Climate Dyn.*, **33**, 629–643, doi: 10.1007/s00382-009-0535-6.

Hall, A., 2004: Role of surface albedo feedback in climate. *J. Climate*, **17**, 1550–1568, doi: [http://dx.doi.org/10.1175/1520-0442\(2004\)017<1550:TROSAF>2.0.CO;2](http://dx.doi.org/10.1175/1520-0442(2004)017<1550:TROSAF>2.0.CO;2).

Hansen, J., A. Lacis, D. Rind, G. Russell, P. Stone, I. Fung, R. Ruedy, and J. Lerner, 1984: Climate sensitivity: Analysis of feedback mechanisms. In Climate Processes and Climate Sensitivity, AGU Geophysical Monograph **29**, Maurice Ewing Vol. 5. J.E. Hansen, and T. Takahashi, Eds. American Geophysical Union, 130-163.

Held, I. M., and B. J. Soden, 2006: Robust responses of the hydrological cycle to global warming. *J. Climate*, **19**, 5686– 5699, doi: <http://dx.doi.org/10.1175/JCLI3990.1>.

Higgins, M. E., and J. J. Cassano, 2009: Impacts of reduced sea ice on winter Arctic atmospheric circulation, precipitation, and temperature. *J. Geophys. Res.*, **114**, D16107, doi: 10.1029/2009JD011884.

Holland, M. M., and C. M. Bitz, 2003: Arctic amplification of climate change in coupled models. *Climate Dyn.* **21**, 221–232, doi: 10.1007/s00382-003-0332-6.

Holland, M. M., D. A. Bailey, B. J. Briegleb, B. Light, and E. Hunke, 2012: Improved sea ice shortwave radiation physics in CCSM4: The impact of melt ponds and aerosols on Arctic sea ice. *J. Climate*, **25**, 1413–1430, doi: <http://dx.doi.org/10.1175/JCLI-D-11-00078.1>.

Hollinger, J., J. Peirce, and G. Poe, 1990: SSM/I instrument evaluation. *IEEE Trans. Geosci. Remote Sens.*, **28**, 781–790, doi:10.1109/36.58964.

Hunke, E. C., and J. K. Dukowicz, 1997: Elastic–Viscous–Plastic Model for sea ice dynamics. *J. Phys. Oceanogr.*, **27**, 1849–1867. doi: 10.1175/1520- 0485(1997)027<1849:AEVPM F>2.0.CO; 2

Hunke, E. C. ,and W. H. Lipscomb, 2008: CICE: The Los Alamos sea ice model, documentation and software, version 4.0. *Los Alamos National Laboratory Tech. Rep. LACC-06-012*, 76 pp.

Hurrell, J. W., M. M. Holland, P. R. Gent, S. Ghan, Jennifer E. Kay, P. J. Kushner, J.-F. Lamarque, W. G. Large, D. Lawrence, K. Lindsay, W. H. Lipscomb, M. C. Long, N. Mahowald, D. R. Marsh, R. B. Neale, P. Rasch, S. Vavrus, M. Vertenstein, D. Bader, W. D. Collins, J. J. Hack, J. Kiehl, and S. Marshall, 2013: The Community Earth System Model: A framework for collaborative research. *Bull. Amer. Meteor. Soc.*, **94**, 1339-1360. doi: <http://dx.doi.org/10.1175/BAMS-D-12-00121.1>.

Iacono, M. J., J. S. Delamere, E. J. Mlawer, M. W. Shephard, S. A. Clough, and W. D. Collins, 2008: Radiative forcing by long-lived greenhouse gases: Calculations with the AER radiative transfer models. *J. Geophys. Res.*, **113**, D13103, doi:10.1029/2008JD009944.

Inoue, J., J. Liu, J. O.Pinto, and J. A. Curry, 2006: Intercomparison of Arctic regional climate models: Modeling clouds and radiation for SHEBA in May 1998. *J. Climate*, **19**, 4167-4178, doi: <http://dx.doi.org/10.1175/JCLI3854.1>.

Intrieri, J. M., M. D. Shupe, T. Uttal, and B. J. McCarty, 2002: An annual cycle of Arctic cloud characteristics observed by radar and lidar at SHEBA, *J. Geophys. Res.*, **107**(C10), doi: 10.1029/2000JC000423.

Jahn, A., K. Sterling, M. M. Holland, J. E. Kay, J. A. Maslanik, C. M. Bitz, D. A. Bailey, J. Stroeve, E. C. Hunke, W. H. Lipscomb, and D. A. Pollak, 2012: Late twentieth-century simulation of Arctic sea ice and ocean properties in CCSM4. *J. Climate*, **25**, 1431–1452, doi: <http://dx.doi.org/10.1175/JCLI-D-11-00201.1>.

Jakobson, E., and T. Vihm, 2010: Atmospheric moisture budget in the Arctic based on the ERA-40 reanalysis. *Intl. J. Clim*, **30**, 2175–2194, doi:10.1002/joc.2039.

Kay, J. E., T. L'Ecuyer, A. Gettelman, G. Stephens, and C. O'Dell, 2008: The contribution of cloud and radiation anomalies to the 2007 Arctic sea ice extent minimum, *Geophys. Res. Lett.*, **35**, L08503, doi:10.1029/2008GL033451.

Kay, J. E., and A. Gettelman, 2009: Cloud influence on and response to seasonal Arctic sea ice loss. *J. Geophys. Res.*, **114**, D18204, doi:10.1029/2009JD011773.

Kay, J. E., B. R. Hillman, S. A. Klein, Y. Zhang, B. Medeiros, R. Pincus, A. Gettelman, B. Eaton, J. Boyle, R. Marchand, and T. P. Ackerman, 2012: Exposing global cloud biases in the Community Atmosphere Model (CAM) using satellite observations and their corresponding instrument simulators. *J. Climate*, **25**, 5190–5207. doi: <http://dx.doi.org/10.1175/JCLI-D-11-00469.1>.

- Khairoutdinov, M. F., and D. A. Randall, 2001: A cloud resolving model as a cloud parameterization in the NCAR Community Climate System Model: Preliminary results. *Geophys. Res. Lett.*, **28**, 3617–3620, doi:10.1029/2001GL013552.
- Khairoutdinov, M. F., and D. A. Randall, 2003: Cloud resolving modeling of the ARM summer 1997 IOP: Model formulation, results, uncertainties, and sensitivities. *J. Atmos. Sci.*, **60**, 607–625, doi:10.1175/1520-0469(2003)060<0607:CRMOTA.2.0.CO;2.
- Khairoutdinov, M. F., D. A. Randall and C. DeMott, 2005: Simulations of the atmospheric general circulation using a cloud-resolving model as a super-parameterization of physical processes. *J. Atmos. Sci.*, **62**, 2136–2154, doi:10.1175/JAS3453.1.
- Klein, S. A., R. B. McCoy, H. Morrison, A. S. Ackerman, A. Avramov, G. d. Boer, M. Chen, J. N. S. Cole, A. D. Del Genio, M. Falk, M. J. Foster, A. Fridlind, J.-C. Golaz, T. Hashino, J. Y. Harrington, C. Hoose, M. F. Khairoutdinov, V. E. Larson, X. Liu, Y. Luo, G. M. McFarquhar, S. Menon, R. A. J. Neggers, S. Park, M. R. Poellot, J. M. Schmidt, I. Sednev, B. J. Shipway, M. D. Shupe, D. A. Spangenberg, Y. C. Sud, D. D. Turner, D. E. Veron, K. v. Salzen, G. K. Walker, Z. Wang, A. B. Wolf, S. Xie, K.-M. Xu, F. Yang, and G. Zhang, 2009: Intercomparison of model simulations of mixed-phase clouds observed during the ARM Mixed-Phase Arctic Cloud Experiment. I: single-layer cloud. *Q.J.R. Meteorol. Soc.*, **135**: 979–1002. doi: 10.1002/qj.416.
- Kooperman, G. J., M. S. Pritchard, M. A. Burt, M. D. Branson, and D.A. Randall, 2016: Robust effects of cloud superparameterization on simulated daily rainfall intensity statistics across multiple versions of the Community Earth System Model. *J. Adv. Model. Earth Syst.* Accepted Author Manuscript. doi:10.1002/2015MS000574.
- Kwok, R., H. J. Zwally, and D. Yi, 2004: ICESat observations of Arctic sea ice: A first look. *Geophys. Res. Lett.*, **31**, L16401, doi:10.1029/2004GL020309.
- Kwok, R., and G. F. Cunningham, 2008: ICESat over Arctic sea ice: Estimation of snow depth and ice thickness. *J. Geophys. Res.*, **113**, C08010, doi:10.1029/2008JC004753.
- Kurita, N., 2011: Origin of Arctic water vapor during the ice-growth season. *Geophys. Res. Lett.* **38**, L02709. doi:10.1029/2010GL046064.
- Laxon, S., N. Peacock, and D. Smith, 2003: High interannual variability of sea ice thickness in the Arctic region. *Nature*, **425**, 947–949, doi:10.1038/nature02050.
- Lee, S., T. Gong, N. Johnson, S. B. Feldstein, and D. Pollard, 2011: On the possible link between tropical convection and the Northern Hemisphere Arctic surface air temperature change between 1958 and 2001. *J. Climate*, **25**, 4350–4367.
- Leibowicz, B. D., D. S. Abbot, K. Emanuel, and E. Tziperman, 2012: Correlation between present-day model simulation of Arctic cloud radiative forcing and sea ice consistent with

positive winter convective cloud feedback. *J. Adv. Model. Earth Syst.*, **4**, M07002, doi: 10.1029/2012MS000153.

Lindsay, R., M. Wensnahan, A. Schweiger, and J. Zhang, 2014: Evaluation of Seven Different Atmospheric Reanalysis Products in the Arctic. *J. Climate*, **27**, 2588–2606. doi: <http://dx.doi.org/10.1175/JCLI-D-13-00014.1>.

Liu, X., S. Xie, J. Boyle, S. A. Klein, X. Shi, Z. Wang, W. Lin, S. J. Ghan, M. Earle, P. S. K. Liu, A. Zelenyuk, 2011: Testing cloud microphysics parameterizations in NCAR CAM5 with ISDAC and M-PACE observations. *J. Geophys. Res.*, **116**, D00T11, doi:10.1029/2011JD015889.

Liu, X., J. E. Penner, S. J. Ghan, and M. Wang, 2007a: Inclusion of ice microphysics in the NCAR Community Atmosphere Model version 3 (CAM3), *J. Climate*, **20**, 4526–4547.

Liu, X., S. Xie, and S. J. Ghan, 2007b: Evaluation of a new mixed-phase cloud microphysics parameterization with CAM3 single-column model and M-PACE observations. *Geophys. Res. Lett.*, **34**, L23712, doi:10.1029/2007GL031446.

Liu, Y., J. R. Key, Z. Liu, and X. Wang and S. J. Vavrus, 2012: A cloudier Arctic expected with diminishing sea ice, *Geophys. Res. Lett.*, **39**, L05705, doi:10.1029/2012GL051251.

Lu, J., and M. Cai, 2010: Quantifying contributions to polar warming amplification in an idealized coupled general circulation model. *Climate Dyn.*, **34**, 669–687, doi:10.1007/s00382-009-0673-x.

Lu, J., and M. Cai, 2009: A new framework for isolating individual feedback processes in coupled general circulation climate models. Part I: Formulation. *Climate Dyn.*, **32**, 873–885, doi: 10.1007/s00382-008-0425-3.

Manabe, S., and R. J. Stouffer, 1980: Sensitivity of a global climate model to an increase of CO₂ concentration in the atmosphere. *J. Geophys. Res.*, **85** (C10), 5529–5554.

Manabe, S., and R. T. Wetherald, 1980: On the distribution of climate change resulting from an increase in CO₂ content of the atmosphere. *J. Atmos. Sci.*, **37**, 99–118, doi: 10.1175/1520-0469(1980)037<0099:OTDOCC>2.0.CO;2.

Manabe, S. and R. T. Wetherald, 1975: The effects of doubling the CO₂ concentrations on the climate of a general circulation model. *J. Atmos. Sci.*, **32**, 3–15, doi:10.1175/1520-0469(1975)032<0003:TEODTC>2.0.CO;2.

Maslowski, W., J. C. Kinney, M. Higgins, and A. Roberts, 2012: The future of Arctic sea ice. *Annu. Rev. Earth Planet. Sci.*, **40** (1), 625–654, doi:10.1146/annurev-earth-042711-105345. 1.

- McCrary, R. R., D. A. Randall, and C. Stan, 2014a: Simulations of the West African monsoon with a superparameterized climate model. Part I: The seasonal cycle. *J. Climate*, **27**, 8303–8322, doi:10.1175/JCLI-D-13-00676.1.
- McCrary, R. R., D. A. Randall, and C. Stan, 2014b: Simulations of the West African Monsoon with a Superparameterized Climate Model. Part II: African Easterly Waves. *J. Climate*, **27**, 8323–8341. doi: <http://dx.doi.org/10.1175/JCLI-D-13-00677.1>
- McGuire, A. D., F. S. Chapin III, J. E. Walsh, and C. Wirth, 2006: Integrated regional changes in Arctic climate feedbacks: Implications for the global climate system, *Annu. Rev. Environ. Resour.*, **32**, 61-91.
- Meyers, M. P., P. J. DeMott, and W. R. Cotton, 1992: New primary ice nucleation parameterizations in an explicit cloud model. *J. Appl. Meteor.*, **31**, 708–721, doi: [http://dx.doi.org/10.1175/1520-0450\(1992\)031<0708:NPINPI>2.0.CO;2](http://dx.doi.org/10.1175/1520-0450(1992)031<0708:NPINPI>2.0.CO;2).
- Miller, J. R., and G.L. Russell, 2002: Projected impact of climate change on the energy budget of the Arctic Ocean by a global climate model. *J Climate*, **15**, 3028-3042.
- Miller, R.L., G.A. Schmidt, and D.T. Shindell, 2006: Forced annular variations in the 20th century IPCC AR4 simulations. *J. Geophys. Res.*, **111**, D18101, doi:10.1029/2005JD006323.
- Morrison, H., and A. A. Gettelman, 2008: A new two-moment bulk stratiform cloud microphysics scheme in the NCAR community atmosphere model (CAM3). Part I: Description and numerical tests. *J. Climate*, **21**, 3642–3659, doi: 10.1175/2008JCLI2105.1.
- Morrison, H. G. de Boer, G. Feingold, J. Harrington, M. D. Shupe, and K. Sulia, 2012: Resilience of persistent Arctic mixed-phase clouds. *Nat. Geosci.*, **5**, 11–17, doi:10.1038/ngeo1332.
- NASA, 2010, *Energy Balance of Earth* [online]. [image]. 2010. [Accessed 10 January 2016]. Available from: <http://www.eoearth.org/view/article/152458/>
- Otto-Bliesner, B.L., E. Brady, G. Clauzet, R. Tomas, S. Levis, and Z. Kothavala, 2006: Last glacial maximum and Holocene climate in CCSM3, *J. Climate*, **19**, 2526-2544, doi: <http://dx.doi.org/10.1175/JCLI3748.1>.
- Park, D.-S., S. Lee, and S. B. Feldstein 2015: Attribution of the recent winter sea-ice decline over the Atlantic sector of the Arctic Ocean. *J. Climate*, **28**, 4027-4033.
- Park, H.-S., S. Lee, S.-W. Son, S. B. Feldstein, and Y. Kosaka, 2015: The impact of poleward moisture and sensible heat flux on Arctic winter sea-ice variability. *J. Climate*, **28**, 5030-5040, doi: <http://dx.doi.org/10.1175/JCLI-D-15-0074.1>.

- Pithan, F., and T. Mauritsen, 2014: Arctic amplification dominated by temperature feedbacks in contemporary climate models. *Nature Geoscience*, **7**, 181–184, doi:10.1038/ngeo2071.
- Pithan, F., B. Medeiros, and T. Mauritsen, 2014: Mixed-phase clouds cause climate model biases in Arctic wintertime temperature inversions. *Climate Dyn.*, **43**, 289–303, doi:10.1007/s00382-013-1964-9.
- Prenni, A. J., P. J. DeMott, S. M. Kreidenweis, J. Y. Harrington, A. Avramov, J. Verlinde, M. Tjernström, C. N. Long, and P. Q. Olsson, 2007: Can ice-nucleating aerosols affect Arctic seasonal climate?. *Bull. Amer. Meteor. Soc.*, **88**, 541–550, doi: <http://dx.doi.org/10.1175/BAMS-88-4-541>.
- Pritchard, M. S., M. W. Moncrieff, and R. C. J. Somerville, 2011: Orographic propagating precipitation systems over the United States in a global climate model with embedded explicit convection, *J. Atmos. Sci.*, **68**(8), 1821–1840, doi: <http://dx.doi.org/10.1175/2011JAS3699.1>
- Randall, D., M. Khairoutdinov, A. Arakawa, and W. Grabowski, 2003: Breaking the cloud parameterization deadlock, *Bull. Amer. Meteor. Soc.*, **84**(11), 1547–1564, doi: <http://dx.doi.org/10.1175/BAMS-84-11-1547>.
- Rauthe, M., A. Hense, and H. Paeth, 2004: A model intercomparison study of climate change-signals in extratropical circulation. *Int. J. Climatol.*, **24**, 643–662, doi: 10.1002/joc.1025.
- Rinke, A., C. Melsheimer, K. Dethlof, and G. Heygster, 2009: Arctic total water vapor: comparison of regional climate simulations with observations, and simulated decadal trends. *J. Hydrometeor.* **10**, 113–129, doi: <http://dx.doi.org/10.1175/2008JHM970.1>.
- Robock, A., 1980: The seasonal cycle of snow cover, sea ice, and surface albedo. *Mon. Wea. Rev.*, **108**, 267–285, doi: [http://dx.doi.org/10.1175/1520-0493\(1980\)108<0267:TS CO SC>2.0.CO;2](http://dx.doi.org/10.1175/1520-0493(1980)108<0267:TS CO SC>2.0.CO;2).
- Roberts, A., J. Cassano, R. Döscher, L. Hinzman, M. Holland, H. Mitsudera, A. Sumi, and J. E. Walsh, 2010: A Science Plan for Regional Arctic System Modeling, A report to the National Science Foundation from the International Arctic Science Community. International Arctic Research Center Technical Papers 10-0001. International Arctic Research Center, University of Alaska Fairbanks.
- Schweiger, A. J., R. W. Lindsay, S. Vavrus, and J. A. Francis, 2008: Relationships between Arctic sea ice and clouds during autumn. *J. Climate*, **21**, 4799–4810, doi:<http://dx.doi.org/10.1175/2008JCLI2156.1>.
- Screen, J. A., and I. Simmonds, 2010a: The central role of diminishing sea ice in recent Arctic temperature amplification. *Nature*, **464**, 1334–1337, doi:10.1038/nature09051.

Screen, J. A., and I. Simmonds, 2010b: Increasing fall-winter energy loss from the Arctic Ocean and its role in Arctic temperature amplification. *Geophys. Res. Lett.*, **37**, L16707, doi: 10.1029/2010GL044136.

Serreze, M. C., A. P. Barrett, A. G. Slater, M. Steele, J. Zhang, K. E. Trenberth, 2007: The large-scale energy budget of the Arctic. *J. Geophys. Res.*, **112**, D11122, doi:10.1029/2006JD008230

Serreze, M. C., and R. G. Barry, 2011: Processes and impacts of Arctic amplification: A research synthesis. *Global and Planetary Change*, **77**, 85–96, doi:10.1016/j.gloplacha.2011.03.004.

Serreze, M. C., A. P. Barrett, and J. Stroeve, 2012: Recent changes in tropospheric water vapor over the Arctic as assessed from radiosondes and atmospheric reanalyses. *J. Geophys. Res.*, **117**, D10104, doi:10.1029/2011JD017421.

Serreze, M. C., and R. G. Barry, 2014, "The Arctic Climate System", 2nd Edition, Cambridge University Press, 404pp.

Shupe, M. D., and J. M. Intrieri, 2004: Cloud radiative forcing of the Arctic surface: The influence of cloud properties, surface albedo, and solar zenith angle, *J. Climate*, **17**, 616–628, doi: 10.1175/1520-0442(2004)017<0616:CRFOTA>2.0.CO;2.

Skific, N., J. A. Francis, and J. J. Cassano, 2009a: Attribution of projected changes in atmospheric moisture transport in the Arctic: A self-organizing map perspective. *J. Climate*, **22**, 4135–4153, doi: <http://dx.doi.org/10.1175/2009JCLI2645.1>.

Skific, N., Francis, J. A., and J. J. Cassano, 2009b: Attribution of seasonal and regional changes in Arctic moisture convergence. *J. Climate*, **22**, 5115–5134, doi: <http://dx.doi.org/10.1175/2009JCLI2829.1>.

Skific, N., and J. A. Francis, 2013: Drivers of projected change in Arctic moist static energy transport. *J. Geophys. Res.*, **118**, 2748–2761, doi: 10.1002/jgrd.50292.

Smith, R. D., P. Jones, B. Briegleb, F. Bryan, G. Danabasoglu, J. Dennis, J. Dukowicz, C. Eden, B. Fox-Kemper, P. Gent, M. Hecht, S. Jayne, M. Jochum, W. Large, K. Lindsay, M. Maltrud, N. Norton, S. Peacock, M. Vertenstein, and S. Yeager, 2010: The parallel ocean program (POP) reference manual: Ocean component of the community climate system model (CCSM) and community earth system model (CESM). *Los Alamos National Laboratory Tech. Rep. LAUR-10-01853*, 141 pp.

Soden, B. J., and I. M. Held, 2006: An assessment of climate feedbacks in coupled ocean–atmosphere models. *J. Climate*, **19**, 3354–3360, doi: <http://dx.doi.org/10.1175/JCLI3799.1>.

Solomon, S., D. Qin, M. Manning, M. Marquis, K. Averyt, M. M. B. Tignor, H. L. Miller Jr., and Z. Chen, Eds., 2007: *Climate Change 2007: The Physical Science Basis*. Cambridge University Press, 996 pp.

Stramler, K. L., 2006: *The Influence of Synoptic Atmospheric Motions on the Arctic Energy Budget*. Ph.D. thesis. Columbia University.

Stramler, K., A. D. Del Genio, and W. B. Rossow, 2011: Synoptically driven Arctic winter states. *J. Climate*, **24**, 1747–1762, doi:10.1175/2010JCLI3817.1.

Stan, C., M. Khairoutdinov, C. A. DeMott, V. Krishnamurthy, D. M. Straus, D. A. Randall, J. L. Kinter III, and J. Shukla, 2010: An ocean-atmosphere climate simulation with an embedded cloud resolving model, *Geophys. Res. Lett.*, **37**, L01702.

Stroeve, J. C., and W. Meier, 2012: Arctic Sea Ice Decline. In *greenhouse gases - emission, measurement and management*, ed. G. Liu, 441-462. New York: InTech.

Sun, L., C. Deser, and R. A. Tomas, 2015: Mechanisms of stratospheric and tropospheric circulation response to projected Arctic sea ice loss. *J. Climate*, **28**, 7824–7845. doi: <http://dx.doi.org/10.1175/JCLI-D-15-0169.1>.

Taylor, K. E., R. J. Stouffer, and G. A. Meehl, 2012: An overview of CMIP5 and the experiment design. *Bull. Amer. Meteor. Soc.*, **93**, 485–498, doi: <http://dx.doi.org/10.1175/BAMS-D-11-00094.1>.

Thayer-Calder, K., and D. A. Randall, 2009: The role of convective moistening in the Madden–Julian oscillation. *J. Atmos. Sci.*, **66**, 3297–3312, doi: <http://dx.doi.org/10.1175/2009JAS3081.1>.

Thompson, D. W. J., and J. M. Wallace, 2000: Annular modes in the extratropical circulation. Part I: Month-to-month variability. *J. Climate*, **13**, 1000–1016, doi: [http://dx.doi.org/10.1175/1520-0442\(2000\)013<1000:AMITEC>2.0.CO;2](http://dx.doi.org/10.1175/1520-0442(2000)013<1000:AMITEC>2.0.CO;2).

Thompson, D. W. J., and J. M. Wallace, 1998: The Arctic Oscillation signature in the wintertime geopotential height and temperature fields. *Geophys. Res. Lett.*, **25**, 1297-1300, doi: 10.1029/98GL00950.

Trenberth, K. E., 1998: Atmospheric moisture residence times and cycling: Implications for rainfall rates with climate change. *Climatic Change*, **39**, 667–694, doi: 10.1023/A:1005319109110.

Trenberth K.E., J. Fasullo, and L. Smith, 2005: Trends and variability in column-integrated atmospheric water vapour. *Clim Dyn* ,**24**, 741–758, 10.1007/s00382-005-0017-4.

- Vavrus, S., 2004: The impact of cloud feedbacks on Arctic climate under greenhouse forcing. *J. Climate*, **17**, 603–615, doi: [http://dx.doi.org/10.1175/1520-0442\(2004\)017<0603:TIO CFO>2.0.CO;2](http://dx.doi.org/10.1175/1520-0442(2004)017<0603:TIO CFO>2.0.CO;2).
- Vavrus, S., U. Bhatt, and V. Alexeev, 2011a: Factors influencing simulated changes in future Arctic cloudiness. *J. Climate*, **24**, 4817–4830, doi: <http://dx.doi.org/10.1175/2011JCLI40 29.1>.
- Vavrus, S., M. M. Holland, and D. A. Bailey, 2011b: Changes in Arctic clouds during intervals of rapid sea ice loss. *Climate Dyn.*, **36**, 1475–1489, doi: [10.1007/s00382-010-0816-0](http://dx.doi.org/10.1007/s00382-010-0816-0).
- Walsh, J. E., and W. L. Chapman, 1998: Arctic cloud-radiation-temperature associations in observational data and atmospheric reanalyses. *J. Climate*, **11**, 3030–3045.
- Walsh, J. E., V. M. Kattsov, W. L. Chapman, V. Govorkova, and T. Pavlova, 2002: Comparison of Arctic climate simulations by coupled and uncoupled models. *J. Climate*, **15**, 1429–1446, doi: [http://dx.doi.org/10.1175/1520-0442\(2002\)015<1429:COAC SB>2.0.CO;2](http://dx.doi.org/10.1175/1520-0442(2002)015<1429:COAC SB>2.0.CO;2).
- Walsh, J. E., S. J. Vavrus, and W. L. Chapman, 2005: Summary of a workshop on modeling of the Arctic atmosphere. *Bull. Amer. Met. Soc.*, **86**, 845–852, doi: [10.1175/BAMS-86-6-845](http://dx.doi.org/10.1175/BAMS-86-6-845).
- Wegener, A., 1911: *Thermodynamik der Atmosphäre*, J. A. Barth, Leipzig, Germany.
- Wetherald, R. T., and S. Manabe, 1986: An investigation of cloud cover change in response to thermal forcing. *Climatic Change*, **8**, 5–24.
- Wetherald, R., and S. Manabe, 1988: Cloud feedback processes in a general circulation model. *J. Atmos. Sci.*, **45**, 1397–1415.
- Winton, M., 2006: Amplified Arctic climate change: What does surface albedo feedback have to do with it? *Geophys. Res. Lett.*, **33**, L03701, doi: [10.1029/2005GL025244](http://dx.doi.org/10.1029/2005GL025244).
- Xie, S., J. Boyle, S. A. Klein, X. Liu, and S. Ghan, 2008: Simulations of Arctic mixed-phase clouds in forecasts with CAM3 and AM2 for M-PACE. *J. Geophys. Res.*, **113**, D04211, doi: [10.1029/2007JD009225](http://dx.doi.org/10.1029/2007JD009225).
- Xie, S., X. Liu, C. Zhao, and Y. Zhang, 2013: Sensitivity of CAM5- simulated Arctic clouds and radiation to ice nucleation parameterization. *J. Climate*, **26**, 5981–5999, doi: <http://dx.doi.org/10.1175/JCLI-D-12-00517.1>.
- Zhang, J., and D. A. Rothrock, 2003: Modeling global sea ice with a thickness and enthalpy distribution model in generalized curvilinear coordinates. *Mon. Wea. Rev.*, **131**, 845–861. doi: [http://dx.doi.org/10.1175/1520-0493\(2003\)131<0845:MGSIWA>2.0.CO;2](http://dx.doi.org/10.1175/1520-0493(2003)131<0845:MGSIWA>2.0.CO;2)

Zhang, T., K. Stamnes, and S. A. Bowling, 1996: Impact of clouds on surface radiative fluxes and snowmelt in the Arctic and Subarctic. *J. Climate*, **9**, 2110–2123, doi: [http://dx.doi.org/10.1175/1520-0442\(1996\)009<2110:IOCOSR>2.0.CO;2](http://dx.doi.org/10.1175/1520-0442(1996)009<2110:IOCOSR>2.0.CO;2).

Zhang, X., J. He, J. Zhang, I. Polyakov, R. Gerdes, J. Inoue, and P. Wu, 2012: Enhanced polarward moisture transport and amplified northern high-latitude wetting trend. *Nat. Climate Change*, **3**, 47–51, doi:10.1038/nclimate1631.

Zygmuntowska, M., T. Mauritsen, J. Quaas, and L. Kaleschke, 2012: Arctic clouds and surface radiation—A critical comparison of satellite retrievals and the ERA-Interim reanalysis, *Atmos. Chem. Phys.*, **12**, 6667–6677, doi:10.5194/acp-12-6667-2012.